QUASIPARTICLE INTERFERENCE AND THE IMPACT OF STRONG CORRELATIONS ON HIGH TEMPERATURE SUPERCONDUCTIVITY

A Dissertation

Presented to the Faculty of the Graduate School

of Cornell University

in Partial Fulfillment of the Requirements for the Degree of

Doctor of Philosophy

by

Andrew Robert Schmidt

August 2009

QUASIPARTICLE INTERFERENCE AND THE IMPACT OF STRONG CORRELATIONS ON HIGH TEMPERATURE SUPERCONDUCTIVITY

Andrew Robert Schmidt, Ph.D.

Cornell University 2009

Spectroscopic imaging - scanning tunneling microscope studies of quasiparticle interference in the high temperature superconductor $Bi_2Sr_2CaCu_2O_{8+\delta}$ as a function hole density and temperature are presented. Its is found that the momentum space source of low energy Bogoliubov excitations is restricted to a region that falls rapidly as the hole density falls to zero. This region agrees well with a strongly correlated generalization of Luttinger's theorem relating the momentum space area of low energy excitations to the electron density. Excitations to higher energies, whose momentum space source would be outside this restricted region without correlations, lack the properties of Bogoliubov quasiparticles and instead locally break translational and rotational symmetries. These real space excitations are demonstrated to be the pseudogap states. An intimate relationship between the Bogoliubov excitation gap and the pseudogap is found. As the temperature increases, the quasiparticle interference patterns persist above the superconducting transition temperature revealing them to be the spectroscopic signature of phase fluctuations. Although the Bogoliubov excitation gap evolves with temperature, both the restricted region in momentum space occupied by the quasiparticles and the real space pseudogap excitation structure does not. The generalized Luttinger's theorem provides a unified framework for understanding the properties of the cuprates at low hole densities in terms of strong correlations.

BIOGRAPHICAL SKETCH

Andy grew up in Santa Rosa, California enjoying the outdoor beauty of the Sonoma coast and making the Sierra Nevada his mountain playground with backpacking in the summer and skiing in the winter. He started college at Montana State University in Bozeman but after one year left for the University of California in Santa Cruz to find science with field work. A broken leg and a pair of surgeries propelled him away from the mountain bumming and into condensed matter physics. Even after seven years in Ithaca, Andy still finds scientific research rewarding. The path for life after the doctorate is unknown but will likely involve a trip or two back to Bishop.

Andy received a Bachelor of Science with highest honors and college honors from the University of California, Santa Cruz in 2002 and a Master of Science degree from Cornell University in 2006. Both degrees are in physics.

To my parents, for teaching me that ignorance is not an option.

ACKNOWLEDGEMENTS

Kyle McElroy, Christian Lupien, and Joan Hoffmann for teaching me the details of how to pursue scientific research. Yuhki Kohsaka, Curry Taylor, Peter Wahl, Mohammad Hamidian, and Focko Meier for pursuing scientific research with me.

It was a pleasure to work with Jhinhwhan Lee, Kazuhiro Fujita, and Chung Koo Kim on the temperature dependent QPI studies.

I appreciate Santiago Grigera and Andy Mackenzie for letting me pursue $Sr_2Ru_2O_7$ research for a bit.

Ben Hunt, Alfred Wang, James Slezak, Ethan Pratt and Jacob Alldredge for being in the same dingy with me as the Seamus Ship arrived from Berkeley.

Seamus Davis for teaching me to focus on research that matters, and for teaching me the importance of brevity in scientific communication.

And again Kyle McElroy, Jenny Hoffman and Ray Simmonds who did the original cuprate QPI work. I hope they see this is fruitful extension and not just a copy of their work.

Mohammad Hamidian for helping me run STM2 while I prepared this dissertation.

I am deeply grateful to the Army Research Office for awarding me a graduate fellowship to fund my education and research efforts.

TABLE OF CONTENTS

LIST OF FIGURES

LIST OF TABLES

CHAPTER 1

INTRODUCTION TO QUASIPARTICLE INTERFERENCE

"My generation is not handing over to yours a clear set of tasks, like the problems in a physics textbook, but when has it ever been clear what is the next thing to be done?" Steven Weinberg[1]

1.1 Tunneling Spectroscopy as a Probe of the Solid State

Tunneling current spectroscopy has been an extremely valuable tool in the experimental verification of the detailed microscopic theory for conventional superconductors. Ivar Giaever's studies[2, 3, 4] of the tunnel current between lead and aluminum separated by a thin insulating layer provided the first direct measurement of the superconducting density of states predicted by the theory of Bardeen, Cooper, and Schrieffer (BCS theory)[5]. For this theory, those three were awarded the 1972 Nobel Prize in Physics, while Giaever's work earned him a share of the 1973 prize. W. L. McMillan and J. M. Rowell[6] inferred both the electron-phonon coupling constant and the phonon density of states in superconducting lead by inverting tunneling spectroscopy measurements using the Eliashberg theory of strong coupling superconductivity[7]. They were able to show that the phonon spectrum derived from the superconducting tunneling spectroscopy agreed with the spectrum directly measured by inelastic neutron scattering[8]. This quantitative agreement between the direct and inferred measurements firmly established the microscopic BCS-Eliashberg description of superconductivity as the condensation of conduction electrons into Cooper pairs. The measurements and analysis of McMillan and Rowell resolved the quantita-

tive discrepancy Giaever[4] observed between experiment and BCS theory.

Tunnel current spectroscopy falls within the broader class of quantum mechanical tunneling phenomena, which describes processes as diverse as the decay rate of low energy α particles from radioactive nuclei. Quantum mechanical tunneling is a direct consequence of the operator commutation hypothesis $[x, p] = i\hbar$ for momentum p and position x, which leads to an exponentially decaying penetration of bound state quantum wave function into the classically forbidden barrier region where the potential energy exceeds the total energy of the state[10, 11]. The experiments of Giaever and McMillan and Rowell consists of electrons tunneling between a superconductor and a normal metal, both of macroscopic extent, that are separated by a microscopically thin insulating material acting as the potential barrier. The superconductor-insulator-normal metal tunnel junction geometry is roughly planar forming a parallel plate capacitor with a dielectric thickness of 100-1000 nanometers. A net tunnel current flows when a D.C. bias voltage V is applied to across the capacitor plates. In the language of many-body quantum theory, the tunneling process can be described by the Hamiltonian

$$\mathcal{H}_T = \sum_{\mu\nu} \left(T_{\mu\nu} c^\dagger_{1,\nu} c_{2,\mu} + T^*_{\nu\mu} c^\dagger_{2,\mu} c_{1,\nu} \right) \tag{1.1}$$

The creation and annihilation operators $c^\dagger_{1,\nu}$, $c^\dagger_{2,\mu}$ create a single particle state in the normal metal (1) or superconductor (2) of quantum numbers ν, μ for the isolated normal metal and superconductor, respectively. For simplicity ν, μ are also chosen to be eigenstates of the appropriate isolated Hamiltonian. The coupling matrix elements are just the overlap of the single particle wave functions ψ through the barrier potential, expressed in the language of first quantization

as

$$T_{\mu\nu} = \int d\mathbf{r}\, \psi^*_{1,\nu}(\mathbf{r})\, H(\mathbf{r})\, \psi_{2,\mu}(\mathbf{r})$$

This tunneling current formulation was introduced by John Bardeen[12] to describe Ivar Giaever's measurements. Assuming a large enough barrier region so that the coupling is weak, the tunnel current is found to first order in $\mathcal{H}_T$ to be[13]

$$I_T = \int_{-\infty}^{\infty} \frac{d\omega}{2\pi\hbar} \sum_{\mu\nu} \left|T_{\mu\nu}\right|^2 A_1(\nu, \omega + eV)\, A_2(\mu, \omega)\, (n_F(\omega + eV) - n_F(\omega)) \quad (1.2)$$

$n_F$is the Fermi function, and the A functions are the single particle spectral functions for the isolated normal metal and superconductor. Because of the relationship

$$n_\nu = \left\langle c^\dagger_\nu c_\nu \right\rangle = \int_{-\infty}^{\infty} \frac{d\omega}{2\pi\hbar} A(\nu, \omega)\, n_F(\omega) \quad (1.3)$$

$A(\nu, \omega)\, n_F(\omega)$ is similar to the probability density function of energy ω for occupation of state ν. By choosing a normal metal with a density of states constant within an electron volt of the chemical potential, the approximation $\sum_\nu \left|T_{\mu\nu}\right|^2 A(\nu, , \omega + eV) \approx const.$ is permissible. By measuring the differential conductance with this approximation we have

$$\frac{dI_T}{dV} \propto \int_{-\infty}^{\infty} \frac{d\omega}{2\pi} - \frac{\partial n_F(\omega + eV)}{\partial\omega} \sum_\mu A_2(\mu, \omega) \quad (1.4)$$

At low enough temperatures, the Fermi function derivative tends to a delta function and 1.4 becomes

$$\frac{dI_T}{dV} \propto \sum_\mu \frac{1}{2\pi} A_2(\mu, \omega = eV) = g(\omega = eV)$$

By Eq. 1.3 this is the total density of states at energy eV.

It is certainly possible to create more sophisticated expressions for the tunnel current than Eq. 1.2. But the power of Eq. 1.2 is that the materials dependencies

collapse into a simple matrix element plus spectral functions, allowing tunnel spectroscopy to become a probe of the intrinsic single particle spectral function of exotic solid state phases. This is what allowed Giaever and McMillan and Rowell to make their spectacular deductions about the nature of superconductors. For simple band structure materials, Eq. 1.2 can be expressed in terms of elementary first quantized concepts. The many-body formalism is introduced here because often the materials of interest are in highly-correlated phases, and Eq. 1.2 allows for the full machinery of many-body quantum field theory in the grand canonical ensemble to be employed in understating the measurements. Often in physics, the simplest conceptual picture is not developed until after the solution is known. For example, the BCS theory[5] was developed without the Bogoliubov diagonalization taught today[14] and is more awkward conceptually. An excellent introduction to many-body quantum theory is Ref. [13].

A few notes about Eq. 1.2. It requires at least two more assumptions about the physics beyond linear response to the tunneling coupling. One assumption is that materials are good conductors so that the electric fields of the D.C. bias fall to zero at the surface.[16, 15] This is not true for doped semiconductors like GaAs, where the poor screening due to the low carrier density lets the fields penetrate 10-1000nm into the bulk.[15, 17] This creates ambiguity as to what energies of the spectral function are actually being probed. The other assumption is that there is no off-diagonal long range order from Cooper pairing. Such terms leads to Josephson tunneling, which are considered in the context of Eq. 1.2 in Chapter 18 of [13]. Further, the spectral function in Eq. 1.2 is that of the relevant surface exposed at the tunnel junction. This spectral function is not necessarily that of the bulk. For the high temperature superconductor studied in this dissertation, oxygen doped $Bi_2Sr_2CaCu_2O_{8+\delta}$, the c-axis surface spectral

function has been experimentally identified as the bulk spectral function.[18]

In his treatment of tunneling, John Bardeen[12] found the matrix elements for a simple barrier to be

$$T_{\mu\nu} = -\frac{\hbar^2}{2m}\int_s dS\left(\psi_\nu^*\frac{\partial\psi_\mu}{\partial z} - \psi_\mu\frac{\partial\psi_\nu^*}{\partial z}\right) \tag{1.5}$$

The z-direction is normal to the tunnel junction interface, and the surface S is any surface that lies completely within the barrier region. If the two wave functions were identical, this would be $-i\hbar J$ for the current operator matrix element J. Using the WKB approximation, it can be shown that T decays exponentially with barrier thickness z.[19, 20]

1.2 The Scanning Tunneling Microscope

The scanning tunneling microscope, or STM, exploits the exponential decay of the tunneling matrix element to achieve atomic resolution imaging on the surfaces of conducting materials. The STM was invented by Gerd Binning and Heinrich Rohrer at IBM Zürich in 1981[29], and their pioneering work earned them a share of the 1986 Nobel Prize in Physics. A conducting sample is held at a D.C. bias voltage while a sharp metallic tip is brought close to its surface an appreciable tunnel current flows. The tip position is controlled by an electronic feedback system that monitors the tunnel current and sets the voltage of the piezoelectric scanner tube holding the tip, deflecting it appropriately. This is depicted by the cartoon of Fig. 1.1. In its simplest mode, the feedback maintains a constant current as the tip is scanned in the plane of the sample while recording the height of the tip. This produces a topographic image of the sample surface. Fig. 1.2a shows a topographic STM image of the surface of $Bi_2Sr_2CaCu_2O_{8+\delta}$. If

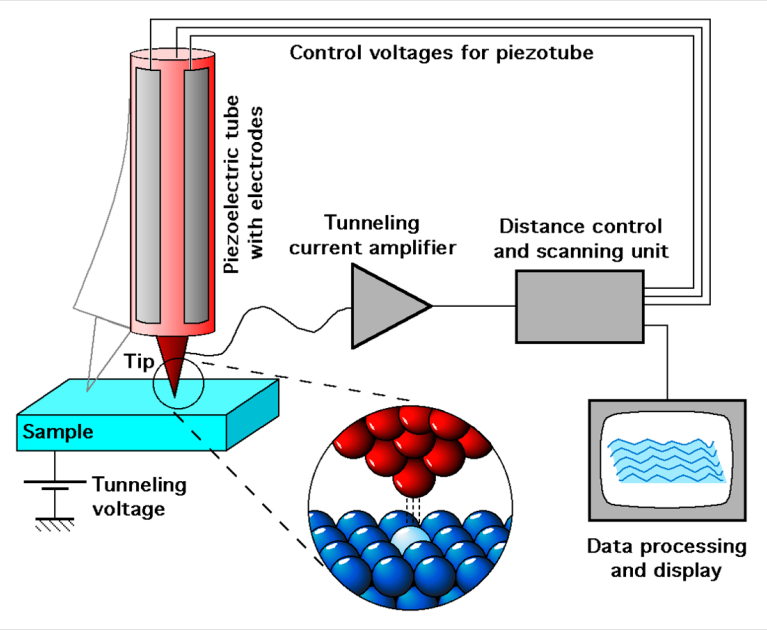

Figure 1.1: Cartoon of STM operation

a single atom protrudes out on the tip apex, then the exponential dependence of the tunneling matrix element on barrier distance ensures that most of the tunnel current will flow through that atom and suppress it in the rest of tip. This allows for in plane spatial resolution approaching the size of an atomic orbital.

The STM tunnel current can be described within the framework of Eq. 1.2 if we chose $1, \nu$ to describe the tip and $2, \mu$ to describe the sample. This was done by Tersoff and Hamann[21, 22], who evaluated the matrix element Eq. 1.5 for a spherical tip apex as

$$T_{\mu\nu} = \frac{\hbar^2}{2m} 4\pi \Omega_t^{-1/2} R e^{\kappa R} \psi_\mu \left(\mathbf{r}_0\right) \tag{1.6}$$

where $\kappa = \hbar^{-1} \left(2m\phi\right)^{1/2}$ is the minimum inverse decay length, ϕ is the effective work function, Ω_t is the tip volume, R is the radius of curvature of the apex, and $\mathbf{r}_0$ is the position vector for the center of curvature of the apex. This matrix element is only valid for tunneling electron energies far below the work function. The wave function in this matrix element can be used in the tunnel conductance

of Eq. 1.2 to change the basis of the sample spectral function into real space (See Appendix A) so that

$$I_t = \left| \frac{\hbar^2}{2m} 4\pi R e^{\kappa R} \right|^2 \int_{-\infty}^{\infty} \frac{d\omega}{\hbar} A_2\left(\mathbf{r}_0, \omega\right) g_1\left(\omega + eV\right) \left[n_F\left(\omega + eV\right) - n_F\left(\omega\right)\right]$$

with $g_1(\omega)$ the density of states per unit volume of the tip. By choosing a tip material with a density of states that is constant within $2eV$ of the chemical potential, the tip density of states can be evaluated at the chemical potential and pulled outside the integral. Common tip materials with this flat density of states include gold, copper and tungsten. Making this approximation and taking the derivative gives us the STM tunnel conductance

$$\frac{dI_t}{dV} = 4\pi^2 \left(\frac{\hbar^2}{m}\right)^2 R^2 e^{2\kappa R} g_1\left(\epsilon_F\right) \int_{-\infty}^{\infty} \frac{d\omega}{\hbar} - \frac{\partial n_F\left(\omega + eV\right)}{\partial \omega} A_2\left(\mathbf{r}_0, \omega\right) \qquad (1.7)$$

At low temperatures, the Fermi function tends to a δ function and this becomes

$$\frac{dI_t}{dV} = \frac{4\pi^2}{\hbar} \left(\frac{\hbar^2}{m}\right)^2 R^2 e^{2\kappa R} g_1\left(\epsilon_F\right) A_2\left(\mathbf{r}_0, \omega = eV\right)$$

In contrast to the tunnel conductance for a planar junction, Eq. 1.4, the STM tunnel conductance above has quantum number resolution. The sum over the quantum numbers for the sample was absorbed into the change of basis to real space. The real space spectral function is more commonly known as the local density of states, or LDOS[21].

As the authors note, the Tersoff-Hamann matrix element Eq. 1.6 is somewhat misleading because the wave function appearing in it suggests that a STM of arbitrarily large radius will give atomic resolution. But the wave function is evaluated at the three-dimensional coordinate $\mathbf{r}_0$ of the center of curvature, which gets farther away from the surface as the radius gets larger. As $\mathbf{r}_0$ moves

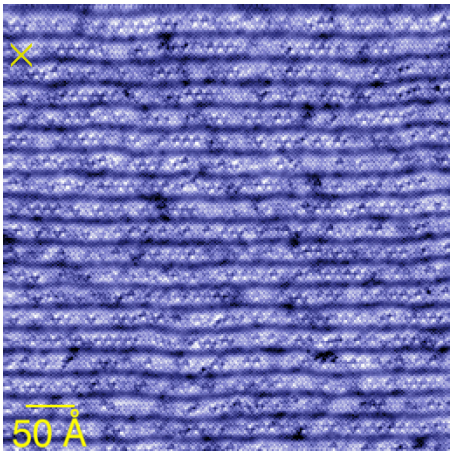

(a) Constant current $z(\mathbf{r})$ recorded during tip movement

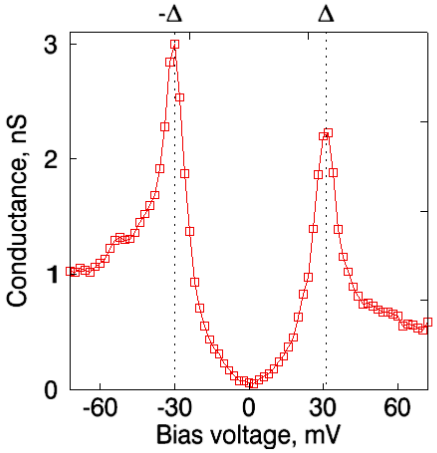

(b) $dI_t/dV(V)$ spectrum recorded at the pixel marked in 1.2a. There is a unique spectrum recorded at every pixel location $\mathbf{r}$ in 1.2a.

Figure 1.2: Example of spectroscopic imaging

away, the atomic corrugations in the surfaces of constant probability density become smeared out and the atoms will cease to be resolved. For a minimum tip-surface separation of z, $\left|\psi_\mu(\mathbf{r}_0)\right|^2 \propto e^{-2\kappa(R+z)}$ and we have I_t, $dI_t/dV \propto e^{-\kappa z}$. This suggests the following experimentally relevant form for the STM tunnel conductance and tunnel current

$$\frac{dI_t}{dV} = Me^{-\kappa z}\rho(\mathbf{r}, \omega = eV) \tag{1.8}$$

$$I_t = Me^{-\kappa z}\int_0^{eV} d\omega \rho(\mathbf{r}, \omega) \tag{1.9}$$

$\rho(\mathbf{r}, \omega)$ is the two-dimensional surface LDOS, and the coordinate $\mathbf{r}$ lies in the plane of the sample surface. M is the constant that absorbs everything else, labeled to suggest it is a matrix element.

Eq. 1.8 suggests the possibility that by measuring dI_t/dV as the tip is moved over the surface, spatially resolved images proportional to the LDOS $\rho(\mathbf{r}, \omega)$ can be produced. This mode of operation is called *spectroscopic imaging* and exploits the real-space quantum number resolution enabled by the STM. For the

measurements presented in this dissertation, spectroscopic imaging is implemented by moving the tip using the same constant current feedback used to produce topographic images. The tip rasters a line in one direction (to the right in Fig. 1.2a), moves a small displacement in the orthogonal direction (down in Fig. 1.2a), and rasters another line. As a line is being rastered, the tip height field $z(\mathbf{r})$ is digitally sampled producing the individual pixels in Fig. 1.2a. The particular pair of current, bias values used to control motion of the tip is called the movement setpoint. Holding Eq. 1.9 constant defines an implicit function for the height field $z(\mathbf{r})$ measured.

In addition, in spectroscopic imaging $dI_t/dV(V)$ as a function of tip-sample bias voltage V is measured at the same location as each height field $z(\mathbf{r})$ pixel. To accomplish this, the tip is first stabilized at the pixel location using constant current feedback, often at a larger setpoint current than is used for tip movement. This bias, current pair is called the spectroscopic setpoint. Then the feedback loop is turned off, and the tip-sample bias voltage is ramped through a range of values while $dI_t/dV(V)$ is recorded. The feedback loop is then turned back on and the tip is moved to the next pixel for another $dI_t/dV(V)$ measurement. A full spectroscopic-imaged data set is called a spectroscopic map and consists of the constant current topography $z(\mathbf{r})$ in Fig. 1.2a, and a spectroscopic curve $dI_t/dV(V)$ at each pixel. These curves are reminiscent of the planar tunneling conductance measurements described in Section 1.1, and a representative curve from the indicated pixel of Fig. 1.2a. is displayed in Fig. 1.2b.

The real-space quantum number resolution of these $dI_t/dV(\mathbf{r}, V)$ curves enable an almost unlimited number of data display possibilities. Fig. 1.3a displays the image $dI_t/dV(\mathbf{r})$ for one bias voltage. The weak patterns in this image are

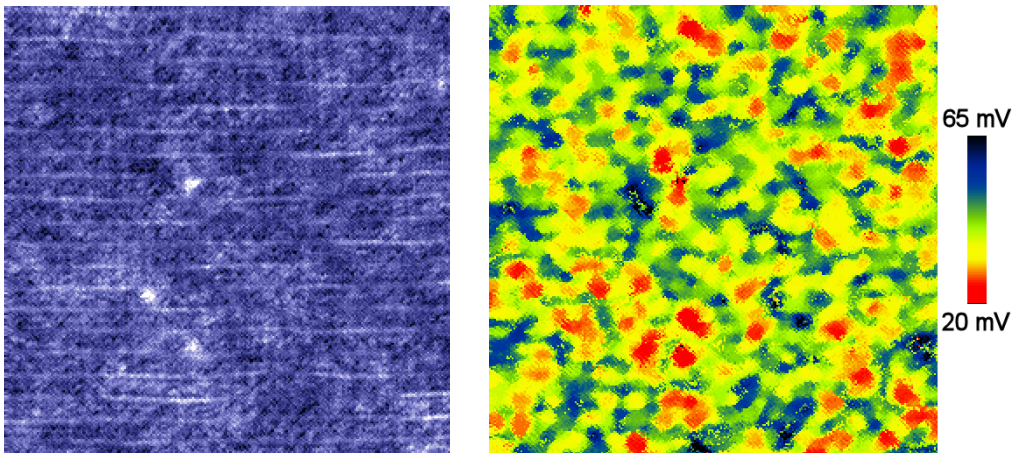

(a) $dI_t/dV\,(\mathbf{r})$ at -12mV at the same positions $\mathbf{r}$ as Fig. 1.2a

(b) Gap map $\Delta\,(\mathbf{r})$ at the same positions $\mathbf{r}$ as Fig. 1.2a

Figure 1.3: Data displays enabled by spectroscopic imaging

the subject of this dissertation. The data displayed in Fig. 1.2 are from a near optimally doped sample of superconducting $Bi_2Sr_2CaCu_2O_{8+\delta}$. The pair of strong peaks in Fig. 1.2b are the superconducting coherence peaks, and the location of their peaks on the energy (bias voltage) axis are a measure of the superconducting gap energy Δ. By finding the peak energies for each pixel, a map of the superconducting energy gap $\Delta\,(\mathbf{r})$, called a gap map, can be made as shown in Fig. 1.3b. Gap maps like this have revealed that strong inhomogeneity may play an important role in the cuprates[23, 24].

In practice, the $dI_t/dV\,(\mathbf{r})$ curves are measured using an AC lock-in amplifier, and in addition to the thermal broadening evident in Eq. 1.7, the bias modulation also limits the energy resolution available, see Appendix B, Eq. B.1.

There are other implementations of spectroscopic imaging employed in STM experiments. Indeed, there is an exceedingly large number of varying STM experiments other than spectroscopic imaging, see for an introduction Ref.[25]. For the full technical and experimental details for the environment demanded

by spectroscopic imaging STM see the dissertations of Refs [26, 27, 28]. The full details of the particular machine operated by the author, including construction, vibrational isolation, and cryogenic refrigeration is available in the dissertation of Dr. Curry Taylor[28].

1.3 Spectroscopic Imaging of Quasiparticle Interference

For Bloch wave functions of the form $\psi_{\mathbf{k}}(\mathbf{r}) = e^{i\mathbf{k}\cdot\mathbf{r}} u_{\mathbf{k}}(\mathbf{r})$, the LDOS of the homogeneous material $\rho(\mathbf{r},\omega) = \sum_{\mathbf{k}} |\psi_{\mathbf{k}}(\mathbf{r})|^2 \delta(\omega - \epsilon_{\mathbf{k}})$ only contains the spatial modulations of $u_{\mathbf{k}}(\mathbf{r})$, which are those of the underlying atomic lattice. This is because the crystal momentum $\mathbf{k}$ diagonalizes the Hamiltonian for the homogeneous system. Introduction of a small amount of impurities breaks the discrete translational invariance of the atomic lattice and induces elastic scattering between the Bloch states. The new eigenstates are linear combinations of the Bloch states on the same constant contour of energy of the band dispersion $\epsilon_{\mathbf{k}}$. This leads to interference patterns in the LDOS. Consider adding an impurity that mixes the two Bloch states $\mathbf{k}_1$ and $\mathbf{k}_2$ at energy ϵ_ν. The new eigenstate is $\psi_\nu(\mathbf{r}) = a_1\psi_{\mathbf{k}_1}(\mathbf{r}) + a_2\psi_{\mathbf{k}_2}(\mathbf{r})$, and the new LDOS is $\rho(\mathbf{r},\omega) = \sum_\nu |\psi_\nu(\mathbf{r})|^2 \delta(\omega - \epsilon_\nu)$. Since

$$\begin{aligned} |\psi_\nu(\mathbf{r})|^2 &= \left|a_1 u_{\mathbf{k}_1}(\mathbf{r})\right|^2 + \left|a_2 u_{\mathbf{k}_2}(\mathbf{r})\right|^2 + a_1 a_2^* u_{\mathbf{k}_1} u_{\mathbf{k_2}}^* e^{i(\mathbf{k}_1-\mathbf{k}_2)\cdot\mathbf{r}} \\ &\quad + a_1^* a_2 u_{\mathbf{k}_1}^* u_{\mathbf{k_2}} e^{-i(\mathbf{k}_1-\mathbf{k}_2)\cdot\mathbf{r}} \end{aligned}$$

the LDOS at energy $\omega = \epsilon_\nu$ of the dirty material will have spatial modulations at the interfering wavevector $\mathbf{q} = \mathbf{k}_1 - \mathbf{k}_2$ that is the difference between the quasiparticle wavevectors of the pure material. In general, elastic scattering in

the dirty system creates modulations in the LDOS at energy ω and wave vector

$$\mathbf{q}(\omega) = \mathbf{k}_1(\omega) - \mathbf{k}_2(\omega) \tag{1.10}$$

where $\mathbf{k}_1$ and $\mathbf{k}_2$lie on the same constant contour of energy for the homogeneous system.

In the 1950s Jacques Friedel considered in detail this problem of the response of a non-interacting homogeneous material to the addition of a single charged point impurity. He found that the impurity-induced density modulations in the electron gas have the asymptotic form

$$\delta n(r) = -\frac{1}{4\pi^2 r^3} \cos(2k_F + \delta_0(k_F)) \sin(\delta_0(k_F))$$

in limit of large distance r from the impurity[30]. k_F is the Fermi wave vector and δ_0 is the phase shift of the scattered states. These density modulations are known as Friedel oscillations.

Because of Eqs. 1.3 & 1.7, STM conductance maps can measure energy resolved Friedel oscillations as quasiparticle interference (QPI). And because of Eq. 1.10, these oscillations can be used to map out the dispersion relation $\epsilon_{\mathbf{k}}$ for the pure system. Mike Crommie, Chris Lutz, and Don Eigler at IBM's Almaden demonstrated this quantitatively for a surface band of Cu(111) at a temperature of 4K, finding a dispersion that matched photoemission results[31]. Further, they were able to show that the oscillations decayed in space with the proper power law exponent for the dimensionality of the band. At the same time, measurements by Hasegawa and Avouris at IBM T. J. Watson of Au(111) at room temperature demonstrated that the oscillations' spatial decay followed an exponential law consistent with thermal broadening[32]. An introductory review of this STM technique for metal surfaces is given in Ref. [33].

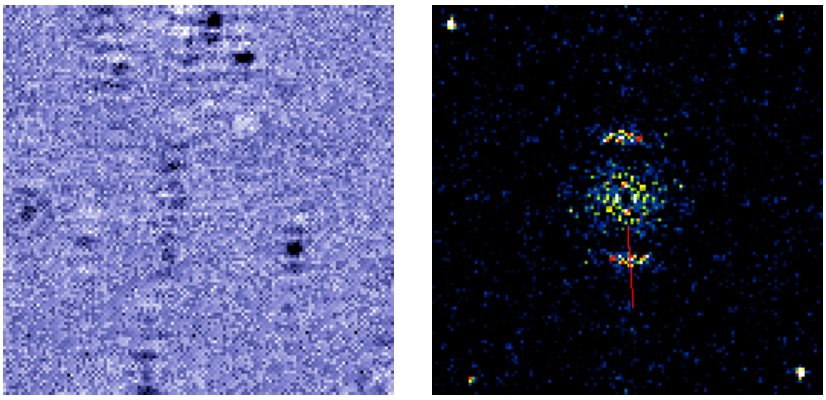

(a) Conductance Map $dI_t/dV\ (\mathbf{r})$ (b) FFT of Conductance Map

Figure 1.4: $S_3R_2O_7$ Fermi energy Spectroscopic Imaging of Quasiparticle Interference

Typically, this is implemented by Fourier transforming the experimental conductance maps and looking for areas of high intensity that disperse with bias voltage. This is demonstrated for spectroscopic image data of $Sr_3Ru_2O_7$ taken at a temperature of 200mK in measurements the author made with Santiago Grigera of the University of St. Andrews. Fig. 1.4a shows the zero bias conductance map. Fig. 1.4b shows its Fourier transform. Data along the line indicated is presented in Fig. 1.5a, showing that a Lorentzian function fits the Fourier transformed data well. Fig. 1.5b shows the resulting $\mathbf{q}\ (\omega)$ dispersion. Though the data is too incomplete to invert Eq. 1.10 for the band dispersion, by assuming an isotropic band, $q = 2k$, a reasonable order of magnitude estimate for the Fermi velocity can be obtained from the straight line fit of Fig. 1.5b. This yields $1\text{x}10^{6}\text{cm/s}$, an order of magnitude that is in agreement with the heavy electron masses obtained from de Haas - van Alphen effect measurements[34]. This $\mathbf{q}\ (\omega)$ vector is not observed at 4K[35], suggesting that STM is accessing the electronic states responsible for the unusual transport and thermodynamic properties of this material, which are proposed to be due to nematic ordering[36].

Quasiparticle interference can be understood within the context of tradi-

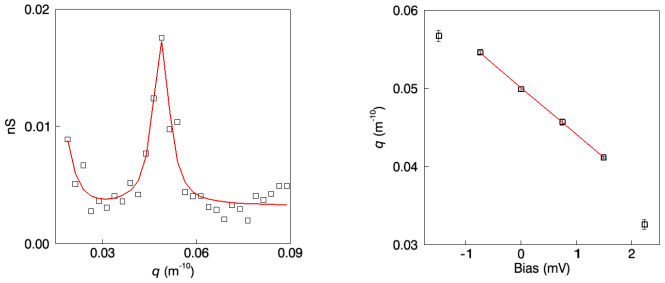

(a) Data along the line in Fig. 1.4b with fit to Lorentzian

(b) $\mathbf{q}(\omega)$ dispersion determined from peak fitting

Figure 1.5: $S_3R_2O_7$ $\mathbf{q}(\omega)$ determination

tional scattering theory. In the T-matrix approach, the Green's function and spectral function are given by

$$G\left(\mathbf{r},\mathbf{r}',\omega\right) = G_0\left(\mathbf{r},\mathbf{r}',\omega\right) + \int d\mathbf{r}_1 d\mathbf{r}_2 G_0\left(\mathbf{r}-\mathbf{r}_1\right) T\left(\mathbf{r}_1,\mathbf{r}_2\right) G_0\left(\mathbf{r}_2-\mathbf{r}'\right)$$

These are the retarded Green's functions, the subscript 0 denotes properties of the homogeneous system, and the T matrix is for the relevant translational symmetry breaking impurity potentials. From Eq. 1.7, for STM observables the relevant quantity is the diagonal spectral function $A\left(\mathbf{r},\omega\right) = -\frac{1}{\pi}G\left(\mathbf{r},\mathbf{r},\omega\right)$. This produces the Fourier transformed LDOS of this model,

$$\begin{aligned} \rho\left(\mathbf{q},\omega\right) &= \rho_0\left(\mathbf{q},\omega\right) - \frac{1}{2\pi i}\left(B\left(\mathbf{q},\omega\right) - B^*\left(-\mathbf{q},\omega\right)\right) \\ B\left(\mathbf{q},\omega\right) &= \int \frac{d\mathbf{k}}{\left(2\pi\right)^d} G_0\left(\mathbf{k}+\mathbf{q},\omega\right) T\left(\mathbf{k}+\mathbf{q},\mathbf{k},\omega\right) G_0\left(\mathbf{k},\omega\right) \end{aligned} \qquad (1.11)$$

d is the dimension of the system. For a single, purely local impurity potential the T matrix depends only on frequency so that Eq. 1.11 becomes $B\left(\mathbf{q},\omega\right) = T\left(\omega\right)\int \frac{d\mathbf{k}}{\left(2\pi\right)^d} G_0\left(\mathbf{k}+\mathbf{q},\omega\right) G_0\left(\mathbf{k},\omega\right)$. For $G_0^{-1}\left(\mathbf{k},\omega\right) = \epsilon_{\mathbf{k}} - \omega + i\delta$ we see that the impurity response $\mathbf{q}$-vectors Eq. 1.10 are given by the autocorrelation of the contours of constant energy for the band structure of the homogeneous system.

1.4 *d*-wave Superconductivity and the Octet Model

For a superconductor such as $Bi_2Sr_2CaCu_2O_{8+\delta}$, the same basic structure as Eq. 1.11 can be applied to describe the quasiparticle interference response in the LDOS. However, the appropriate retarded Green's function for the superconducting state is a 2x2 matrix $\mathcal{G}$ describing the propagation of Nambu spinors $\alpha_{\mathbf{k}}(\omega)$

$$\alpha_{\mathbf{k}}(\omega) = \begin{bmatrix} c_{\mathbf{k}\uparrow}(\omega) \\ c^{\dagger}_{-\mathbf{k}\downarrow}(\omega) \end{bmatrix} \mathcal{G}(\mathbf{k},\omega) = \begin{bmatrix} G_{\uparrow\uparrow}(\mathbf{k},\omega) & F^{*}_{\downarrow\uparrow}(\mathbf{k},\omega) \\ F_{\downarrow\uparrow}(\mathbf{k},\omega) & G^{*}_{\downarrow\downarrow}(-\mathbf{k},\omega) \end{bmatrix} \quad (1.12)$$

$G_{\sigma\sigma}(\mathbf{k},\omega)$ is the usual single particle Green's function associated with propagation of $\left\langle c^{\dagger}_{\mathbf{k}\sigma}(t)\, c_{\mathbf{k}\sigma}\right\rangle$, while $F_{\downarrow\uparrow}(\mathbf{k},\omega)$ is the anomalous Green's function associated with propagation of the Cooper pairs $\left\langle c^{\dagger}_{\mathbf{k}\uparrow}(t)\, c^{\dagger}_{-\mathbf{k}\downarrow}\right\rangle$ of the superconducting state. When included in the tunnel current response calculated from Eq 1.1, the anomalous Green's function yields the Josephson current. With this formalism, the FT-LDOS for the superconducting state is

$$\begin{aligned} \rho_{sc}(\mathbf{q},\omega) &= \rho_0(\mathbf{q},\omega) - \frac{1}{2\pi i}\left(\mathcal{B}_{11}(\mathbf{q},\omega) + \mathcal{B}_{22}(\mathbf{q},-\omega)\right. \\ &\quad \left. -\mathcal{B}^{*}_{11}(-\mathbf{q},\omega) - \mathcal{B}^{*}_{22}(-\mathbf{q},-\omega)\right) \end{aligned} \quad (1.13)$$

$\mathcal{B}_{ii}$ is the Nambu matrix form of the B function in Eq. 1.11. Ch 18. of Ref. [13] has an introduction to the Nambu formalism of superconducting Green's functions.

$Bi_2Sr_2CaCu_2O_{8+\delta}$ is in the cuprate family, a high temperature superconductor with a maximum transition temperature of 98K. Goerg Bednorz and Alex Müller won the 1987 Nobel Prize in Physics for discovering the high temperature superconducting state in the cuprates. In addition to the high transition temperature, another unconventional feature of these materials is the anisotropic superconducting order parameter. Phase sensitive techniques have exhaustively

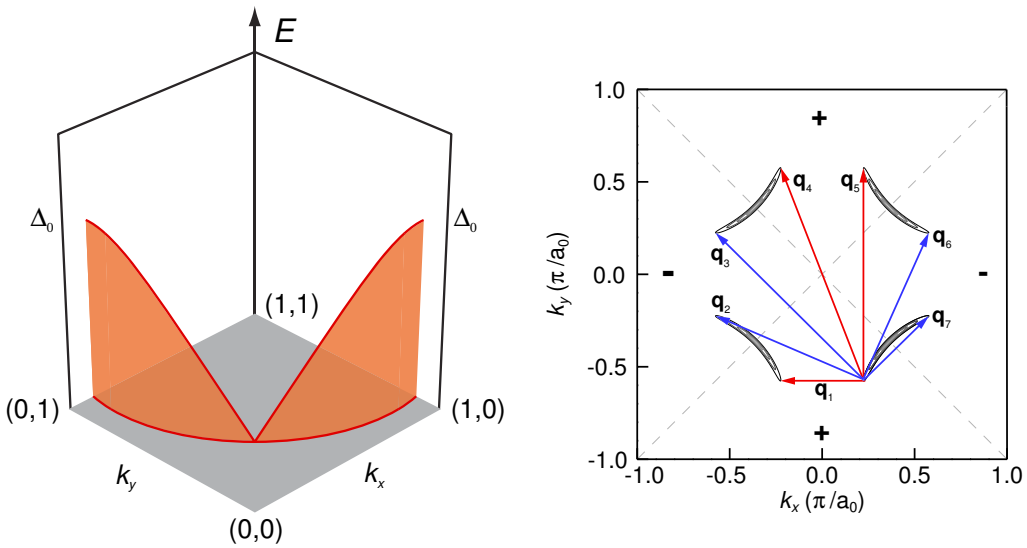

(a) $Bi_2Sr_2CaCu_2O_{8+\delta}$ Fermi surface gapped by the d-wave superconducting state

(b) Octet model $\mathbf{q}$-vectors for $\omega = 20$ meV. The $\mathbf{k}$-vectors satisfying the simultaneous pole equations are indicated by the black contour. Dashed lines are the nodes in $\Delta_{\mathbf{k}}$, and its relative sign is indicated.

Figure 1.6: $Bi_2Sr_2CaCu_2O_{8+\delta}$ momentum space near optimal doping

shown that the superconducting state of these material has $d_{x^2-y^2}$ symmetry, meaning that the order parameter changes sign under 90 degree rotations[37, 38]. This leads to the anisotropic charge excitation gap opening on the Fermi surface, shown in Fig. 1.6a, as determined by experiment[39, 40]. The d-wave superconducting gap function used for this figure is
$\Delta_{\mathbf{k}} = \frac{\Delta_0}{2}\left(\cos\left(k_x a_0\right) - \cos\left(k_y a_0\right)\right)$.

The $\mathbf{k}$-space origin of the scattering $\mathbf{q}$-vectors observed in $\rho_{SC}\left(\mathbf{q},\omega\right)$ is determined by assuming that the integral for $\mathcal{B}\left(\mathbf{q},\omega\right)$ is dominated by states satisfying the simultaneous pole equations for the two $\mathcal{G}_0$'s. Of this set, those with the largest joint density of states will contribute the most to the FT-LDOS. In the cuprates $|\partial_{\mathbf{k}}\Delta_{\mathbf{k}}|_{\omega=0} \ll v_F$, and these $\mathbf{q}$-vectors satisfy Eq. 1.10 for $|\Delta_{\mathbf{k}}| = \omega$. The $\mathbf{q}$-vector dispersion is dominated by the gap dispersion. For the experimental parameters above, the $\mathbf{q}$-vectors for the homogeneous non-interacting

$\mathcal{G}_0^{-1}(\mathbf{k},\omega) = (\omega + i\delta)\, I - \epsilon_{\mathbf{k}}\sigma_3 - \Delta_{\mathbf{k}}\sigma_1$ in this model are displayed in Fig. 1.6 for $\omega < \Delta_0$. Because of the symmetries of both the square lattice of the cuprates and the $d_{x^2-y^2}$ superconducting state, one octet of the Fermi surface determines all the **q**-vectors measured at one $eV = \omega$. This is called the octet model[41, 43].

Eq. 1.13 for the superconducting state FT-LDOS does not appear any different from the normal state form, Eq.1.11. It is still just a single particle measurement. So why make this distinction? In the superconducting state, different scattering processes affect the observed **q**-vectors in different ways that can only determined by the anomalous Green's function. In particular, by considering the effect of the superconducting coherence factors it is expected that scattering off of scalar potentials is primarily expressed through the amplitude of the blue **q**-vectors of Fig. 1.6. Scattering produced by time-reversal symmetry breaking potentials mainly impacts the amplitude of the red vectors[41]. Physically, the difference between these two sets of vectors is that the blue **q**-vectors span Fermi surface segments of opposite order parameter sign, while the red connect segments of the same sign. Also, unique to the superconducting state, there is order parameter scattering, due to inhomogeneities in the Cooper pairing field[45]. This response is purely expressed by the amplitude of red **q**-vectors. The order parameter phase impacts the FT-LDOS because the single-particle and anomalous Green's functions are related algebraically by their equations of motion

$$\begin{aligned} (-\omega - \epsilon_{\mathbf{k}})\, G_{\uparrow\uparrow} &= -1 + \Delta_{\mathbf{k}} F_{\downarrow\uparrow} \\ (-\omega + \epsilon_{\mathbf{k}})\, F_{\downarrow\uparrow} &= \Delta_{\mathbf{k}}^{*} G_{\uparrow\uparrow} \end{aligned} \tag{1.14}$$

Studying the amplitudes of the two sets of vectors could enable not only a determination of the scattering sources, but also the detailed structure of the full

superconducting state embodied by the Nambu formalism in Eq. 1.12.

The octet model was observed in near optimally doped $Bi_2Sr_2CaCu_2O_{8+\delta}$ by the experiments of Refs. [43, 44]. Ref. [43] showed that the two low energy LDOS modulations of largest amplitude were consistent with the octet model. Ref. [44] showed that all observed low energy modulations were at octet $\mathbf{q}$-vectors by inverting Eq. 1.10 along with $|\Delta_{\mathbf{k}}| = eV$ to produce a model Fermi surface and gap dispersion. More information on these experiments can be found in Refs. [43, 42]. The theory was first developed in Ref. [41]. This model has also been observed for optimally doped $Ca_{2-x}Na_xCuO_2Cl_2$, whose very different crystal structure, chemistry, and apical Cu atom demonstrate that octet QPI is a universal feature of these materials[46]. A magnetic field test of the phase sensitive nature of the different $\mathbf{q}$-vector amplitudes in Fig. 1.6 has been reported[47].

1.4.1 Consistency with Angle Resolved Photoemission

The octet model QPI experiments of Refs [43, 44] were noted to be consistent with the results of Angle Resolved Photoemission Spectroscopy (ARPES) by a direct comparison of inverted STM data. ARPES directly probes the momentum space spectral function by measuring the photocurrent I from electrons ejected by a sample surface in the process of photon absorption, $A(\mathbf{k},\omega) \propto I(\mathbf{k},\omega)$. Such measurements can in principle directly determine the band structure and the modulus of the gap dispersion, $|\Delta_{\mathbf{k}}|$. See Ref [39, 40] for more this on technique and its use in study of the cuprates. The observed consistency confirms that both measurements are accessing the same intrinsic cuprate electronic

structure, independent of the very different matrix elements of the two probes.

In addition, it was suggested[48] that Eq. 1.13 implies that autocorrelation $\int I(\mathbf{k},\omega)\, I(\mathbf{k}+\mathbf{q},\omega)\, d\mathbf{k}$ of experimental ARPES maps would reproduce the features of FT-LDOS **q-**maps. Excellent agreement was found in a reduced zone scheme if the photon polarization was chosen to suppress nodal quasiparticles through the ARPES matrix element[49, 50, 51]. The agreement became worse when the photon polarization allowed the nodal quasiparticles in the photocurrent[49]. These observations were found to support the hypothesis that nodal quasiparticles in STM measurements of $Bi_2Sr_2CaCu_2O_{8+\delta}$ are suppressed by tunneling through the BiO and SrO layers located between the CuO_2 plane and vacuum[53, 52]. In addition, ARPES autocorrelation found that $\mathbf{q}_1$ and $\mathbf{q}_5$ become non-dispersive at higher energies than analyzed in Refs [43, 44], and that above T_C the **q**-maps had the same spatial pattern as the octet model and these patterns did not disperse with energy[50, 51].

1.5 Tunneling Conductance Ratio Z and the Setpoint Effect

The constant current feedback technique used to control the in-plane motion of the STM tip can have an impact on the observed conductance spectra. By holding Eq. 1.9 for the tunnel current constant at the spectroscopy setpoint, the factor Me^{-kz} can be eliminated in Eq. 1.8 for the conductance:

$$\frac{dI_t}{dV}(\mathbf{r},V) = \frac{I_0\rho(\mathbf{r},eV)}{\int_0^{eV_0} d\omega\rho(\mathbf{r},\omega)} \tag{1.15}$$

While for $V \ll \phi$ it is always true that the tunnel conductance is proportional to the LDOS, if the LDOS integrated to the setpoint bias is inhomogeneous, then the constant of proportionality changes with position. In particular, Fourier

transformed conductance maps become the FT-LDOS convolved with the Fourier transform of the integrated LDOS. This can make QPI analysis impossible. Unfortunately, for underdoped $Bi_2Sr_2CaCu_2O_{8+\delta}$ at typical setpoint biases of ~100-300mV, the integrated LDOS has been observed to be very inhomogeneous[23, 24, 54, 55, 56].

Fortunately, for the superconducting state there is a solution. By taking the ratio of conductance at opposite bias polarities ($\pm|V|$ for one $|V|$) but at the same location $\mathbf{r}$, the $I_0/\int_0^{eV_0} d\omega\rho$ terms cancel leaving[46, 55]

$$Z(\mathbf{r},V)=\frac{dI_t/dV(\mathbf{r},|V|)}{dI_t/dV(\mathbf{r},|V|)}=\frac{\rho(\mathbf{r},e|V|)}{\rho(\mathbf{r},-e|V|)} \tag{1.16}$$

An example of this setpoint effect cancellation for a $T_C = 45$K underdoped $Bi_2Sr_2Ca_{0.8}Dy_{0.2}Cu_2O_{8+\delta}$ sample is presented in Fig. 1.7. The relative image contrast is identical in each column in this figure. The conductance has the same modulations as Ref. [56], and is found to be very sensitive to the setpoint bias V_0, while the ratio Z is unchanging. The weakening of these 'checkerboard' modulations at -25mV with setpoint bias is strong evidence that their origin is due to the inhomogeneous integrated LDOS in the denominator of Eq. 1.15 and not due to the LDOS itself. Note that for this setpoint cancellation to work, it is crucial that the conductance values are taken from the same spectroscopic curve.

In the superconducting state, Z is the ratio of the of the modulus squared of the coherence factors[14, 57]

$$Z(\mathbf{r},V)=\frac{|u(\mathbf{r},\omega=eV)|^2}{|v(\mathbf{r},\omega=eV)|^2} \tag{1.17}$$

The Bogoliubov wavefunction normalization constraint $|u(\mathbf{r})|^2+|v(\mathbf{r})|^2=1$ ensures that the spatial modulations in $dI_t/dV(\mathbf{r},V)$ are not canceled in Eq.

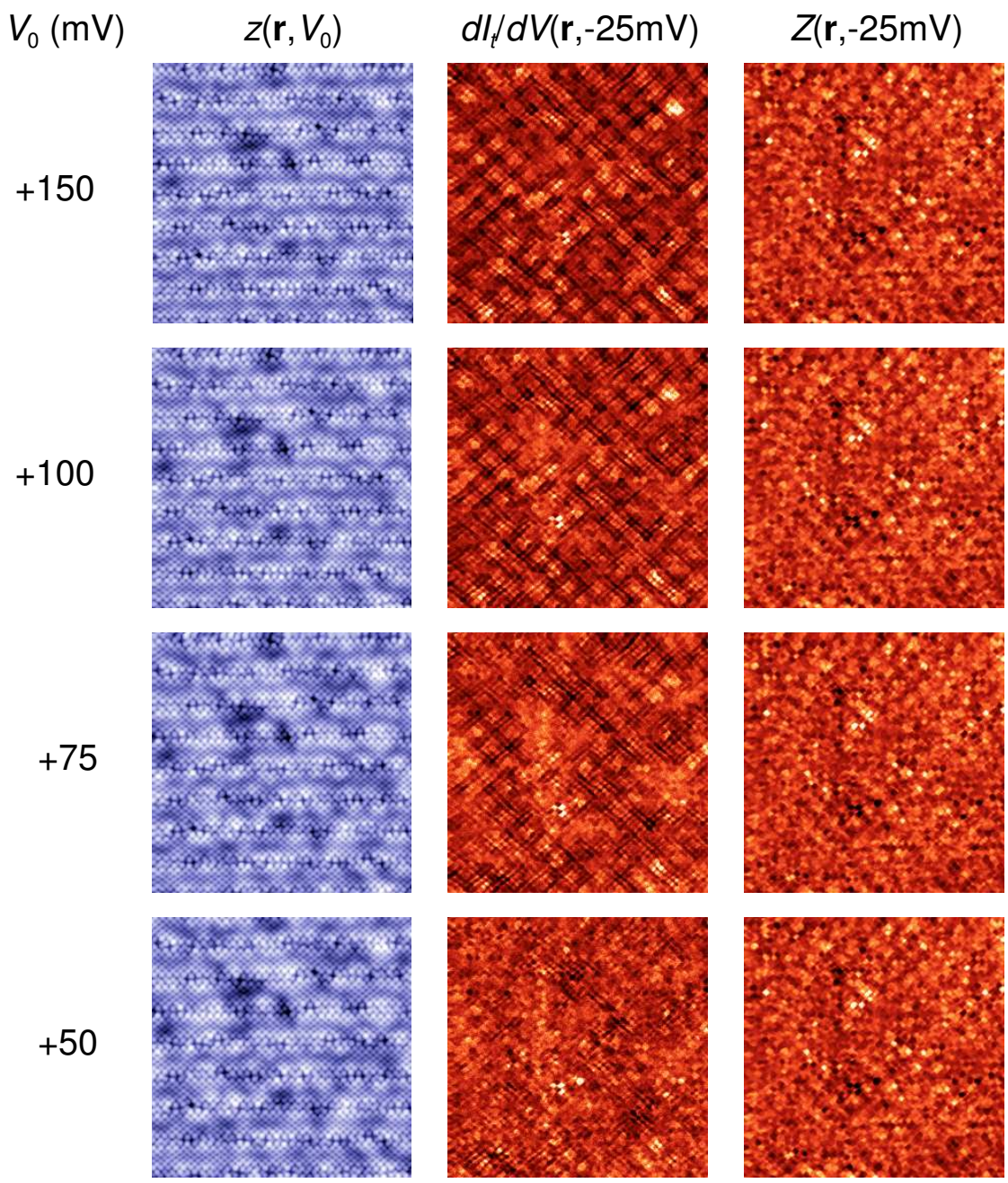

Figure 1.7: An example of the setpoint effect and its cancellation.

1.17. For instance, consider $|u(\mathbf{r})|^2$ with a sinusoidal spatial variation: $|u(\mathbf{r})|^2 = u_0 + u_1 \sin(\mathbf{k}\cdot\mathbf{r})$. The normalization constraint requires $|v(\mathbf{r})|^2 = 1 - u_0 - u_1 \sin(\mathbf{k}\cdot\mathbf{r})$ so that a local maximum in $|u(\mathbf{r})|^2$ occurs at the same location in space as a local minimum in $|v(\mathbf{r})|^2$. This anti-phase relation between the parti-

cle and hole components of Bogoliubov QPI modulations preserves the 16 dispersing octet **q**-vectors in the measured ratio Z. The appearance of octet QPI modulations following cancellation of the setpoint effect in the conductance ratio Z was first demonstrated experimentally in $Ca_{2-x}Na_xCuO_2Cl_2$[46].

1.6 Motivation for this Dissertation

Fig. 1.8 displays the phase diagram for the cuprate high temperature superconductors. At zero hole concentration, the strong on-site Coulomb repulsion of the copper atoms make these materials anti-ferromagnetic Mott insulators (AFMI). Adding a few percent of holes destroys the antiferromagnetic state and induces the pseudogap[58] (PG) state at ~3%. At ~5% the cuprates transform into *d*-wave superconductors (*d*-SC) with a maximum transition temperature of ~100K. The underdoped and overdoped regions of the phase diagram are where the hole concentration is respectively less than, and greater than, the concentration that gives the maximum transition temperature. Least understood of the phase diagram is the pseudogap region. It is characterized by anomalous transport, thermodynamic, and spin response properties. The pseudogap state disappears at a temperature T^*, but because it is not a thermodynamically ordered state, this is a cross over lacking sharp definition. The underdoped superconducting state is characterized by a thermal transition where the microscopic excitation gap Δ of ARPES[59] and STM[60, 89] does not vanish, even though as $T \rightarrow 0$ this gap appears to be a mean-field *BCS* type. Rather, this gap vanishes at T^* which rises as the hole concentration is reduced towards the Mott insulating state, even though the superconducting transition temperature is itself falling. Intuition derived from the successes of mean-field theory suggests that this gap

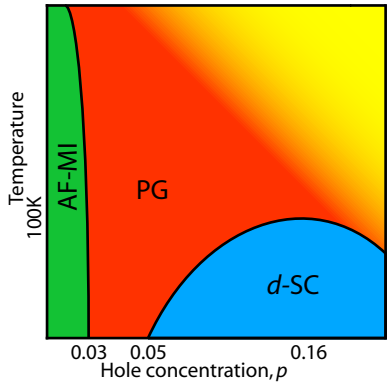

Figure 1.8: Cuprate phase diagram

maybe related to the unknown pairing mechanism drives the anomalously high superconducting transition temperatures.

The principle reason for studying QPI in the cuprates is the simultaneous existence homogeneous quasiparticles at low energies and very inhomogeneous phenomena at higher energies, as evidenced by the $\Delta(\mathbf{r})$ map in Fig. 1.3b. QPI enables the STM to become the only instrument capable of simultaneously determining both the momentum-space electronic structure and the atomic scale real-space electronic structure. By using the conductance ratio Z, QPI has become a tool to study the behavior of both the delocalized superconducting states and the $\Delta(\mathbf{r})$ structure as the hole doping is reduced towards the Mott insulating state in the cuprates.

CHAPTER 2

EXTRACTION OF QUASIPARTICLE INTERFERENCE WAVE VECTORS

> "Economics is not physics, and experiments are impossible to conduct with enough control to consistently give us predictable results." Ben Stein[61]

2.1 Experimental Data Acquisition

The spectroscopic imaging STM (SI-STM) instruments are housed in ultra low vibration laboratories, specifically designed to facilitate these projects. Each consists of an underground concrete vault conditioned to be anechoic, inside which is a nested acoustic isolation room. The inner room (total mass 3×10^4 kg) is supported on six pneumatic vibration isolators. Inside the inner acoustic isolation chamber is the cryostat itself whose structure has integrated within it 3×10^3 kg of lead. It includes another massive vibration isolation stage with three pneumatic isolators. The liquid helium vessel is suspended from this stage. The SI-STM is usually suspended from a home-made ultra low vibration sub-kelvin refrigerator inside the cryogenic vacuum space. Design of our custom built cryogenic SI-STM systems is summarized in Refs. [26, 27, 28, 62].

All $Bi_2Sr_2CaCu_2O_{8+\delta}$ crystals studied are grown by floating-zone furnace techniques in the laboratories of Prof. S. Uchida at the University of Tokyo and of Dr. H. Eisaki at AIST, Tsukuba. The samples with superconducting transition temperatures (T_C) of 20 K, 42.5K and 45 K were doped with Dy at the Ca site, $Bi_2Sr_2Ca_{0.8}Dy_{0.2}Cu_2O_{8+\delta}$ while the others were $Bi_2Sr_2CaCu_2O_{8+\delta}$. The 88K sample had ^{18}O isotope substitution. The hole density p for each sample is estimated

Table 2.1: Samples studied

Compound	T_C (K)	p
$Bi_2Sr_2Ca_{0.8}Dy_{0.2}Cu_2O_{8+\delta}$	20	0.06
$Bi_2Sr_2Ca_{0.8}Dy_{0.2}Cu_2O_{8+\delta}$	37	0.06-0.07
$Bi_2Sr_2Ca_{0.8}Dy_{0.2}Cu_2O_{8+\delta}$	45	0.08
$Bi_2Sr_2CaCu_2O_{8+\delta}$	74	0.14
$Bi_2Sr_2CaCu_2O_{8+\delta}$	88	0.17
$Bi_2Sr_2CaCu_2O_{8+\delta}$	86	0.19

by combining the results from several different probes, including magnetic susceptibility changes at T_C , c-axis length from X-ray diffraction, zero-resistivity transition at T_C , temperature dependence of resistivity, magnitude of Hall coefficient, effective carrier number from optical conductivity, mean gap values (STM), and Fermi surface volume (ARPES). Inductively coupled plasma optical emission spectroscopy was used to measure the cation ratio relative to the amount of Cu to check for sufficient crystal quality. The transition temperatures and corresponding hole dopings are reported in Table 2.1. The 20K, 45K, 74K, 88K, and 86K samples were used to study the doping dependence of QPI at 4.2K. The 42.5K sample was used to study the temperature dependence of QPI.

Each crystal is segmented in 1 mm-square plates which are mounted on the sample holder studs for insertion into the cryogenic SI-STM system, introduced in the cryogenic vacuum space and slowly cooled below 20K, mechanically cleaved, and inserted in the STM head. Once the STM scanner has approached the BiO surface of a crystal, a large field of view (FOV) of dimension 50 nm square is chosen for study. It is necessary to achieve highly repeatable subatomic resolution and register in topographic images of this surface. The same resolution is required in differential conductance $dI_t/dV\,(\mathbf{r}, V)$ maps to ensure accurate measurement of both high **q**-vectors in the QPI patterns and the **r**-space structure at high energies. The large > 40 nm FOV is required simultaneously

in order to attain sufficient Fourier space resolving power to detect any slowly dispersing **q**-vectors in the QPI patterns. In particular, the resolution Δq in **q**-space is determined by the physical length L of and image side $\Delta q = 2\pi L^{-1}$, while the Nyquist **q**-vector is given by $q_{\mathrm{Ny}} = \pi (\Delta L)^{-1}$, where ΔL is the physical size of a spectroscopic imaging pixel. For $p \gtrsim 0.11$, the Nyquist frequency is just the smallest Cu-O reciprocal lattice vector, $q_{\mathrm{Ny}} = 2\pi/a_0 = 2\pi/3.83\text{Å}$ with a_0 the Cu-O-Cu bond length. Then $L = 65$nm and 256x256 pixels are optimal. For $p < 0.11$, there is additional spectral contrast on the O atoms[55] so that the Nyquist wave vector needs to be $q_{\mathrm{Ny}} = 5\pi/4a_0$ to prevent this contrast from folding onto the QPI **q**-vectors. At these dopings, $L =$50nm with 256x256 pixels.

A repeated series of $dI_t/dV\,(\mathbf{r}, V)$ maps meeting these specifications and without loss of atomic register to the crystal lattice due to drift or distortion for periods of up to a year, are carried out in each FOV. They are designed to achieve a signal-to-noise ratio in every spectrum of at least 20:1 (since many of the modulations to be studied are only a few percent of the average value of $dI_t/dV\,(\mathbf{r}, V)$) and to achieve simultaneously an energy resolution specification $\delta E \sim 2$ meV. These procedures were repeated for several samples at each of six different hole-densities. To complete this large data set, three different SI-STM systems were used.

The analysis of the T_{C}=86K sample was presented in the original full octet model inversion of Ref. [44]. The analysis was performed on the conductance dI_t/dV, and not on the conductance ratio Z Eq. 1.16. In particular, this work forms part of the doctoral dissertation of Professor Kyle McElroy at the University of Colorado, Boulder[42].

2.2 The Fourier Transform Power Spectrum, Averaging, and S/N

To analyze the data, all real space $Z(\mathbf{r}, V)$ data sets have the mean value $\langle Z(\mathbf{r}, V)\rangle_{\mathbf{r}}$ subtracted and are multiplied by a quadratic window before Fourier transformation to minimize leakage effects on low intensity signals. Leakage is due to the finite extent of space acquired by digital sampling, and results in a wave vector $\mathbf{q_0}$ of the Fourier transform $Z(\mathbf{q}_0, V)$ having a contribution from $Z(\mathbf{q}, V)$ at all other wave vectors $\mathbf{q}$. Since the ratio of largest to smallest $\mathbf{q}$-vector amplitude is as large as 20, the window does make a difference in the $\mathbf{q}(\omega)$ dispersion extraction presented in this chapter. All $\mathbf{q}(\omega)$ were determined from the locations of local maxima in the Fourier transform amplitude $|Z(\mathbf{q}, V)|$ as suggested in Fig. 1.5b. To increase the signal-to-noise (S/N) ratio, several averaging techniques were applied the the Fourier transform power spectral density (PSD), $|Z(\mathbf{q}, V)|^2$.

The physical dimensions of all $\mathbf{q}$-vectors are calibrated against the location of the Cu-O-Cu reciprocal lattice vectors in the topography $z(\mathbf{r}, V)$ acquired simultaneously with the spectroscopic maps. The first technique is to break the original PSD up into blocks of four nearest neighbor pixels, and then replace each block with the average value of the four pixels. As a result of such averaging, a PSD that is originally 256 pixels square becomes 128 pixels square, and the S/N of each pixel increases by a factor of 2. This is discussed in Refs. [63, 64]. We refer to this as 'reduction averaging'. In general, averaging over n pixels in the PSD increases the S/N by a factor of $\sqrt{n}$[65]. The next type of PSD averaging depends on the symmetry of the $\mathbf{q}$-vector, as discussed in Secs. 2.3, 2.4 below. Finally, the square root operation $\sqrt{|Z(\mathbf{q}, V)|^2} = |Z(\mathbf{q}, V)|$ approximately doubles the S/N. This is seen from an estimation of the standard

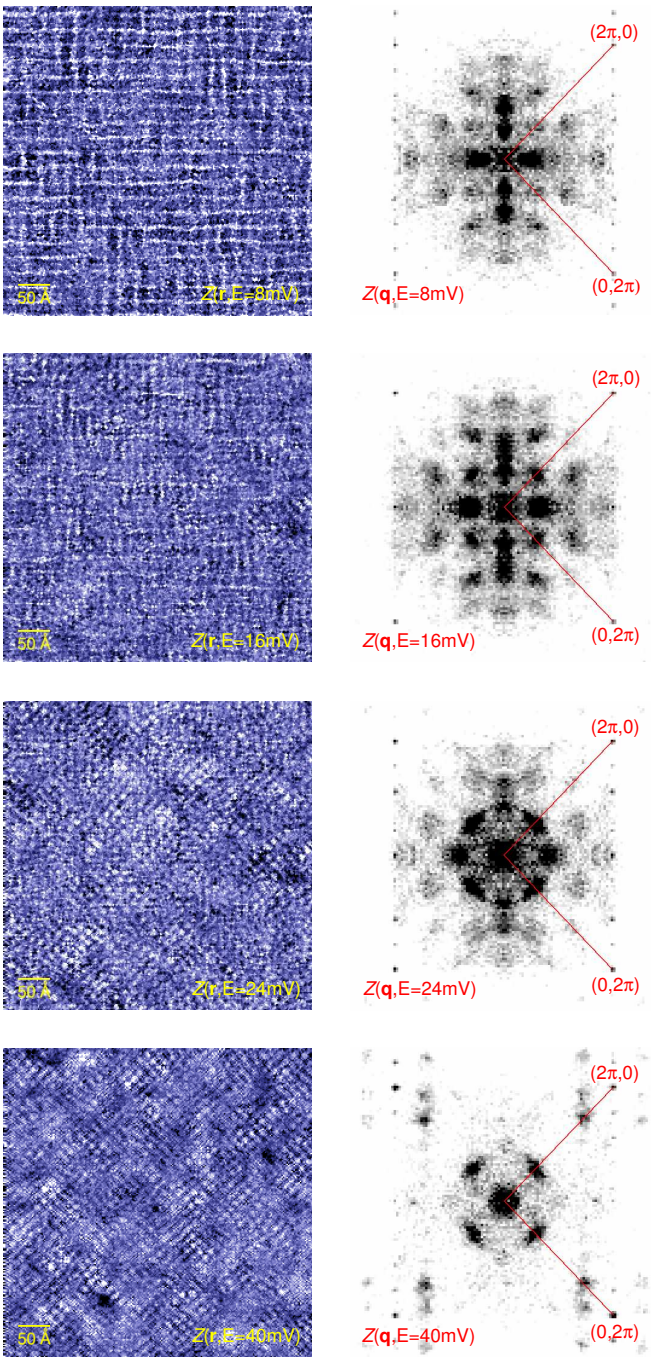

Figure 2.1: Example pairs of $Z(\mathbf{r}, V)$, processed $|Z(\mathbf{q}, \omega)|$ at 4.2K for T_C= 45K

deviation from partial derivatives.

Examples of $Z(\mathbf{r}, V)$, raw quadratically windowed $|Z(\mathbf{q}, V)|$, and $|Z(\mathbf{q}, V)|$ after reduction averaging and the symmetrization averaging described in Sec.

2.4 are presented in Fig. 2.1. These modulations in Z can be compared to the modulations in conductance dI_t/dV visible in Fig. 1.3a. Again, the QPI analysis of Refs. [43, 44] was performed on the conductance.

2.3 Symmetry Constrained Wave Vectors

Some $\mathbf{q}$-vectors are constrained to disperse along high symmetry directions. These are $\mathbf{q}_1$ and $\mathbf{q}_5$, which disperse along the $d_{x^2-y^2}$ antinodal and Cu-O-Cu bond direction, and $\mathbf{q}_7$ and $\mathbf{q}_3$ which disperse $d_{x^2-y^2}$ nodal direction. The labeling here is from Fig. 1.6. For these, one-dimensional linecuts of $|Z(\mathbf{q}, V)|$ data along the high symmetry directions are taken with multi-pixel averages in the transverse direction. This type of averaging has been discussed in Ref. [64]. The peak locations q_i are found by non-linear least squares fitting a Lorentzian function

$$f(q) = \frac{a}{\left(\frac{q-q_i}{b}\right) + 1}$$

with either an exponential or linear background term. In many cases, $\mathbf{q}_1$ and $\mathbf{q}_5$ are found simultaneously with two lorentzian functions and a fixed location Gaussian function for the Cu-O-Cu reciprocal lattice vector. An example of the linecuts and resulting fits used to extract these $\mathbf{q}$-vectors are shown in Fig. 2.2 for the T_C = 20K sample. The doping dependence of the linecuts at 4.2K for $\mathbf{q}_1$ and $\mathbf{q}_5$ is displayed in Fig. 2.3. The doping dependence of the linecuts at 4.2K for $\mathbf{q}_3$ and $\mathbf{q}_7$ is displayed in Fig. 2.4. The temperature dependence of the linecuts for T_C = 42.5K for $\mathbf{q}_1$ and $\mathbf{q}_5$ is displayed in Fig. 2.5. The temperature dependence of the linecuts for T_C = 42.5K for $\mathbf{q}_7$ is displayed in Fig. 2.6

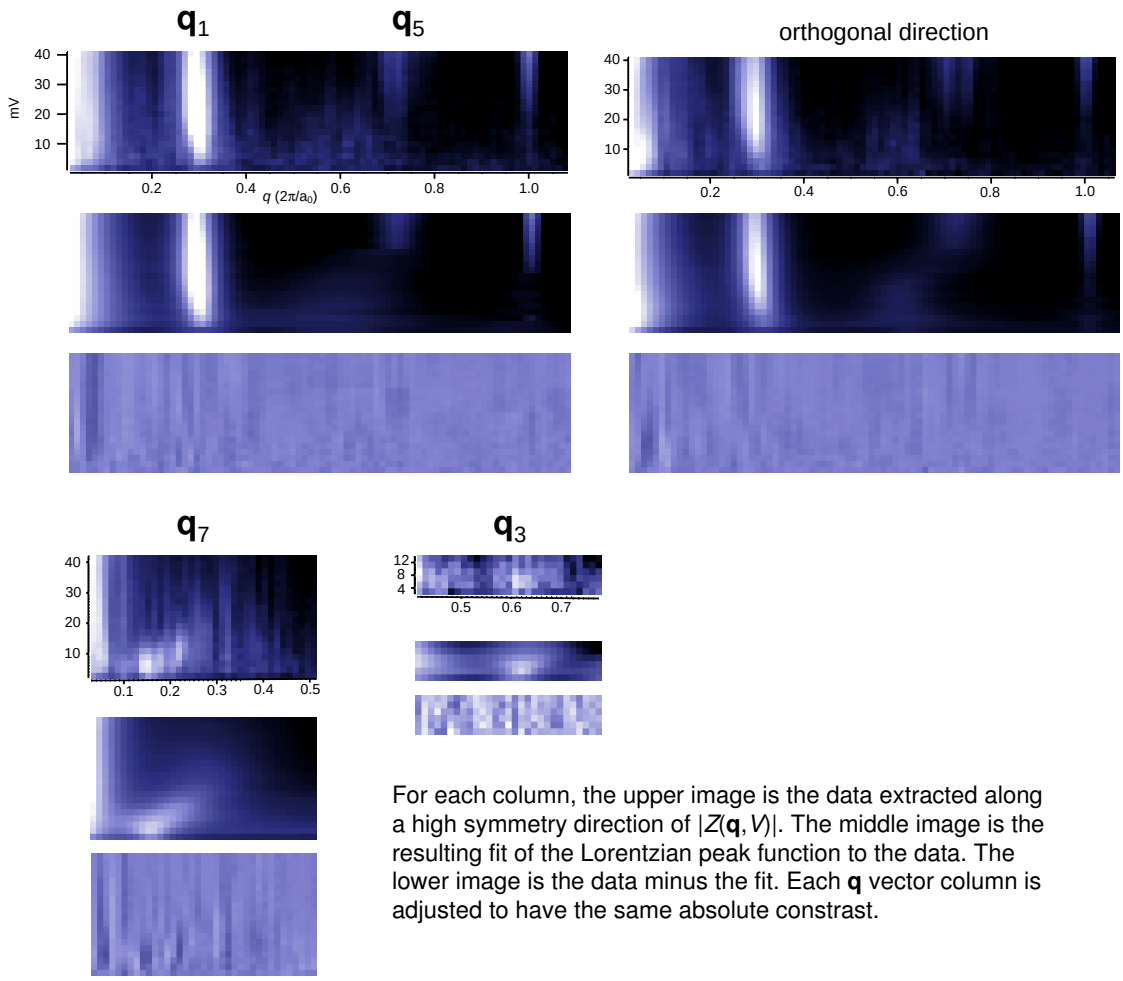

For each column, the upper image is the data extracted along a high symmetry direction of $|Z(\mathbf{q}, V)|$. The middle image is the resulting fit of the Lorentzian peak function to the data. The lower image is the data minus the fit. Each **q** vector column is adjusted to have the same absolute constrast.

Figure 2.2: Example of constrained **q**-vector fits for T_C= 20K sample.

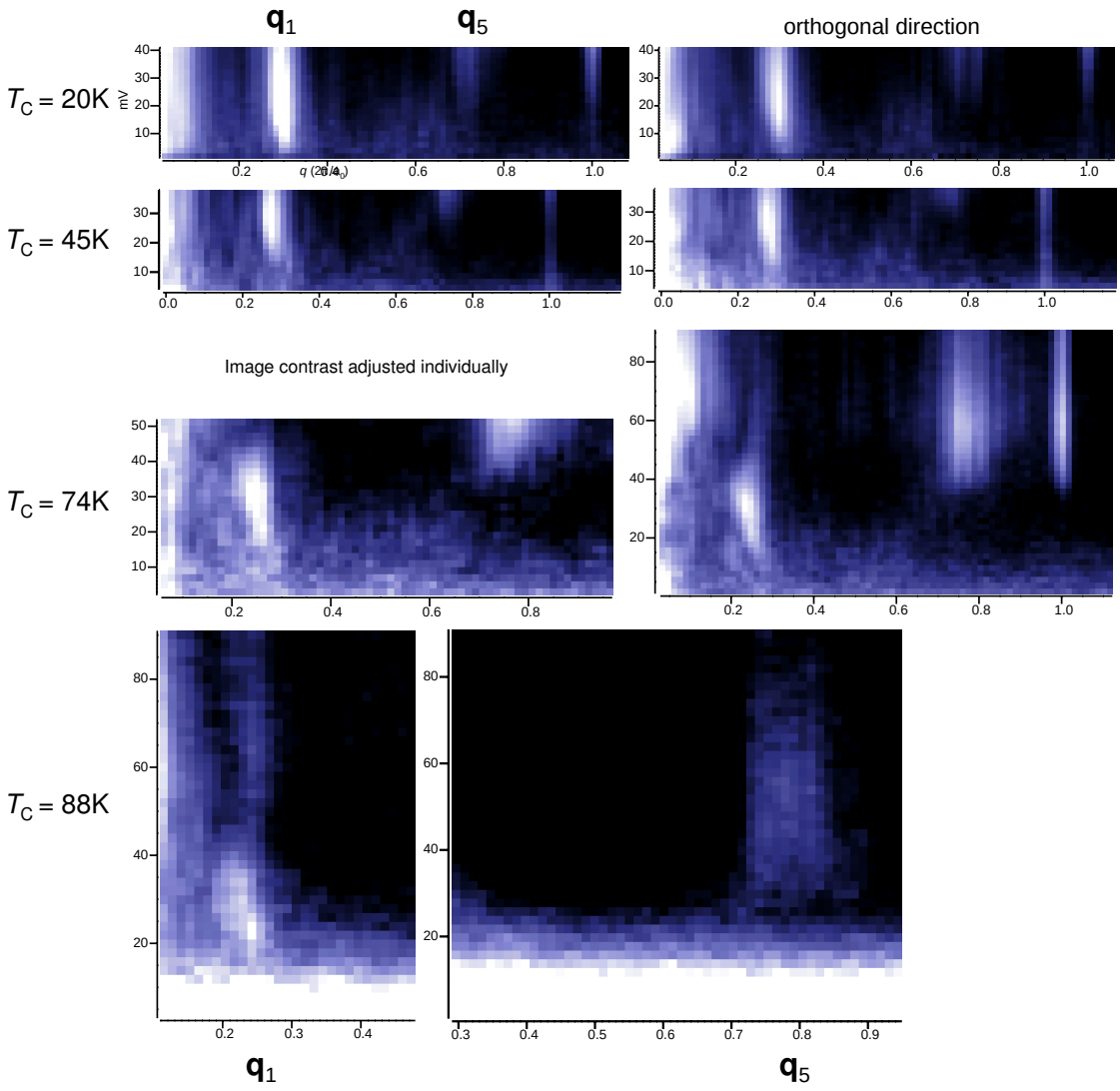

Figure 2.3: Doping dependence of $\mathbf{q}_1$, $\mathbf{q}_5$ linecuts

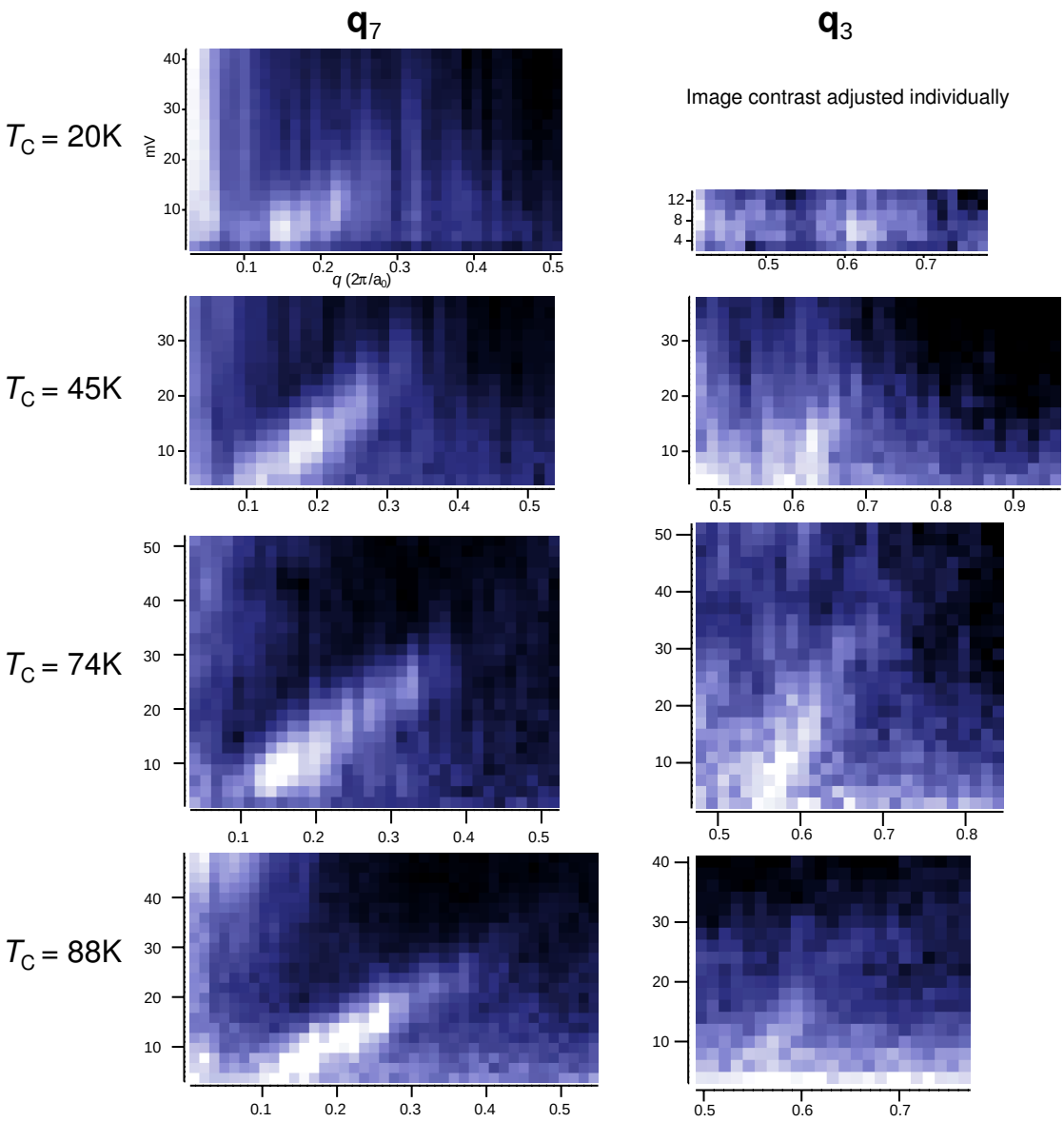

Figure 2.4: Doping dependence of $\mathbf{q}_3$, $\mathbf{q}_7$ linecuts

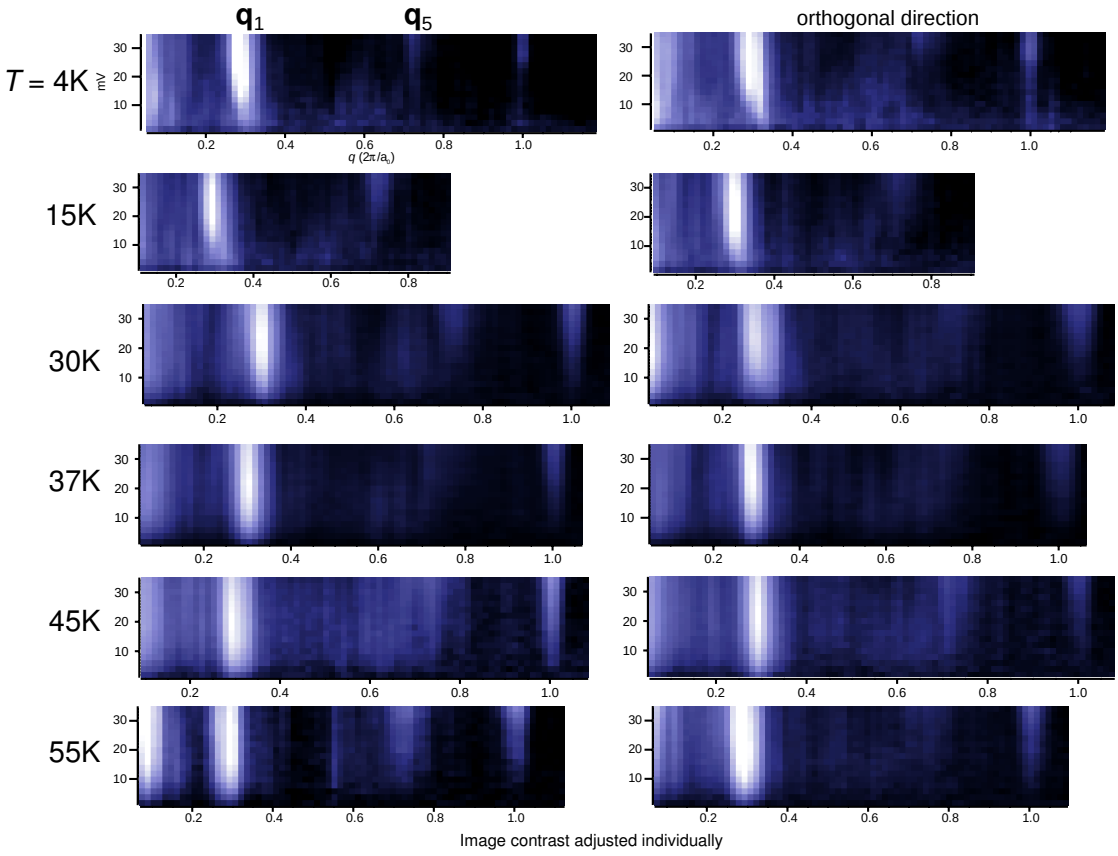

Figure 2.5: Temperature dependence of $\mathbf{q}_1$, $\mathbf{q}_5$ linecuts

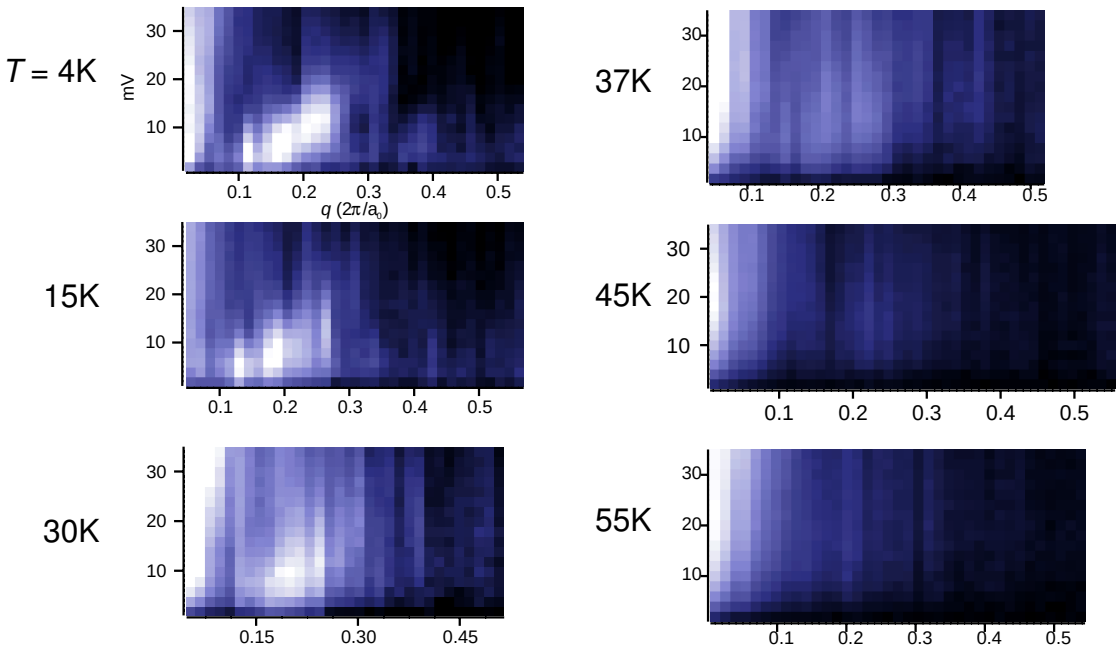

Figure 2.6: Temperature dependence of $\mathbf{q}_7$ linecut

2.4 Unconstrained Wave Vectors

The **q**-vectors unconstrained to lie along high symmetry directions are $\mathbf{q}_2$, $\mathbf{q}_6$, and $\mathbf{q}_4$ of Fig. 1.6. For these, following the reduction averaging of Sec. , the PSD is symmetrized along the crystalline *a*-axis. This is 'symmetrization averaging', examples of which are presented in the second column of Fig. 2.1. These **q**-vectors are fit with two-dimensional Lorentzian functions of the from

$$f(\mathbf{q}) = \frac{a}{\left(\frac{q_x - q_{xi}}{b_x}\right)^2 + \left(\frac{q_y - q_{yi}}{b_y}\right)^2 + 1}$$

along with an additional background term that is either exponential or linear. Examples of some fits are presented in Fig. 2.7.

The octet vector $\mathbf{q}_4$ often proved difficult to find. It appears that its experimental spectral weight has a different, more asymmetric distribution than $\mathbf{q}_2$, $\mathbf{q}_6$. Ref. [66] notes that for the homogeneous response function theory this is to be expected, as $\mathbf{q}_4$ is at the endpoint of a high intensity arc while all the other **q**-vectors are formed at the intersection of high intensity arcs, as depicted in Fig. 14 of Ref. [64]. The author did not attempt to find a more suitable peak function for $\mathbf{q}_4$.

The doping dependence of the reduction averaged and symmetrized $|Z(\mathbf{q}, V)|$ at 4.2K is presented in Fig. 2.8. The temperature dependence of the reduction averaged and symmetrized $|Z(\mathbf{q}, V)|$ for T_C = 42.5K is presented in Fig. 2.9. The red lines in these figures connect the origin with the Cu-O-Cu bond reciprocal lattice vector.

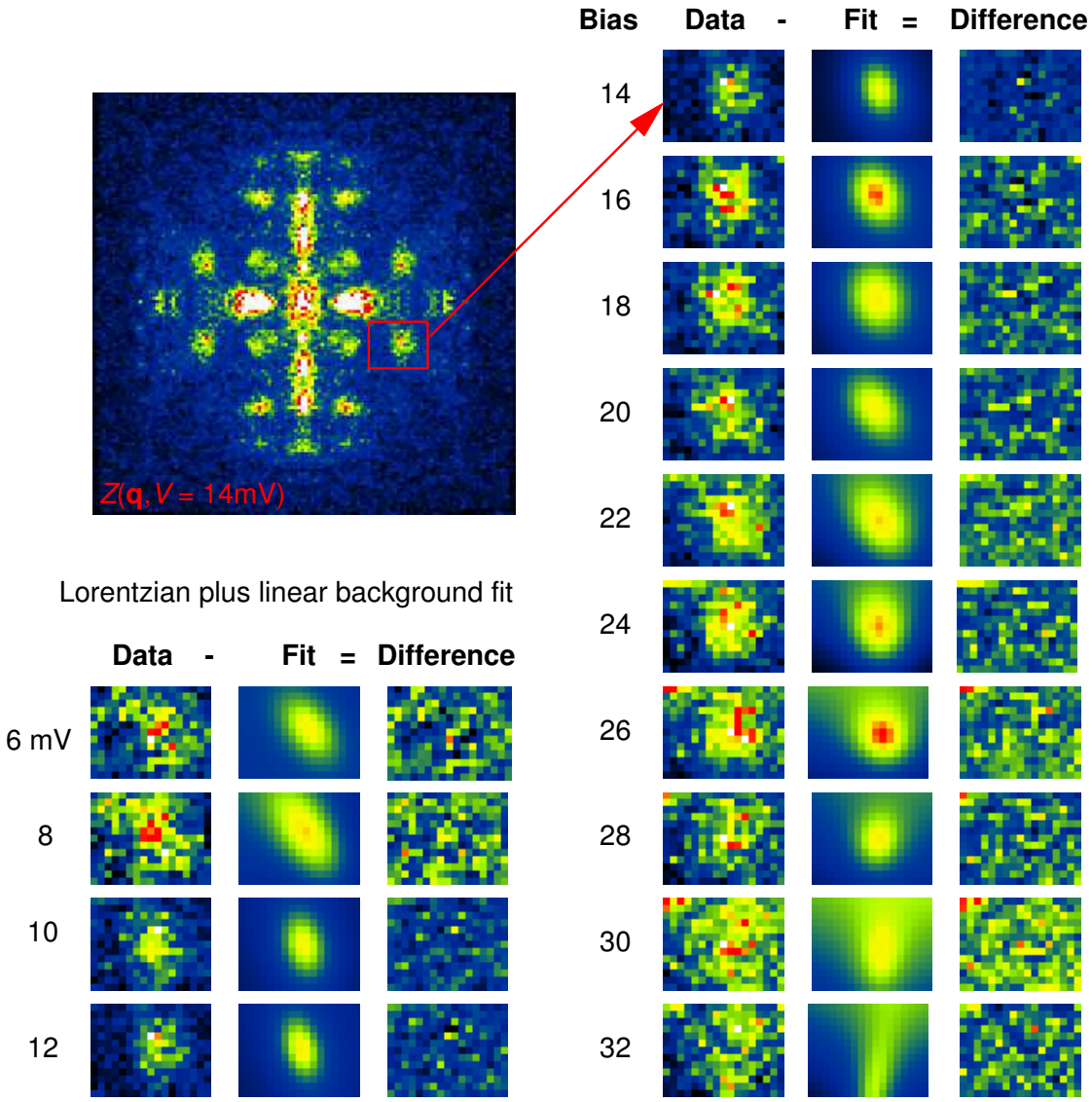

Figure 2.7: Example of unconstrained fit to $\mathbf{q_2}$ for T_C= 74K sample

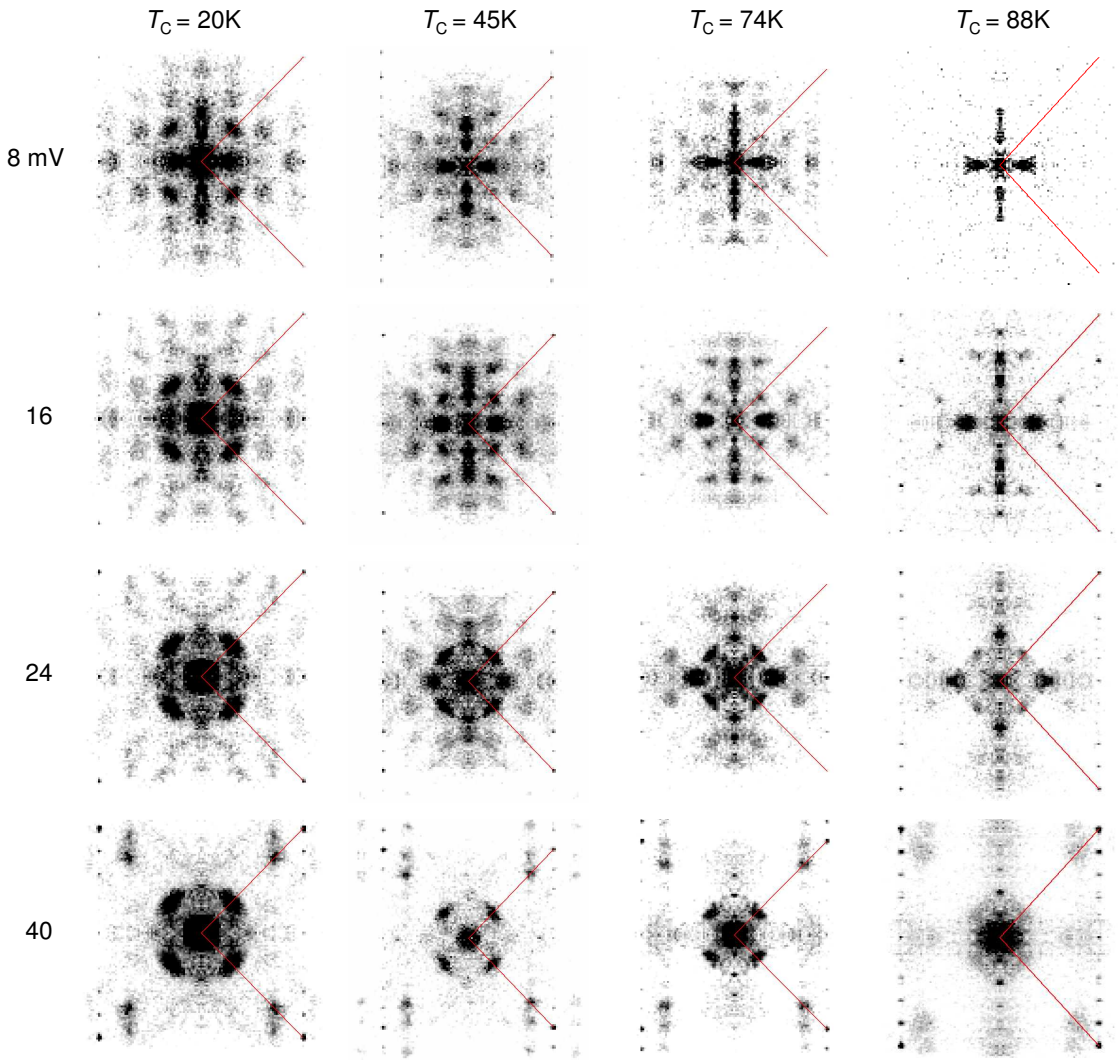

Figure 2.8: Doping dependence of processed $|Z(\mathbf{q}, V)|$

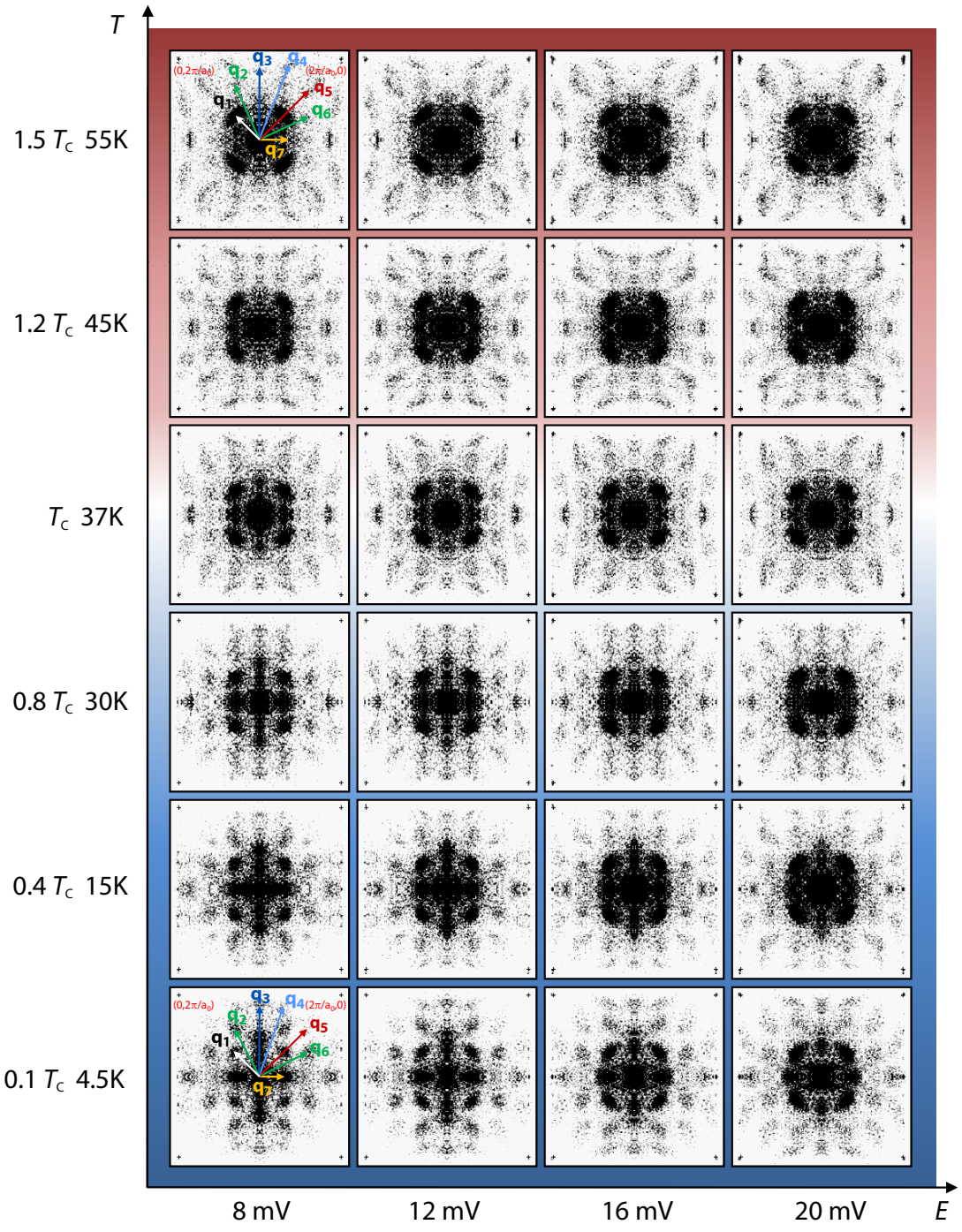

Figure 2.9: Temperature dependence of processed $|Z(\mathbf{q}, V)|$

2.5 Noise and Line Shape Analysis

By extracting the noise distribution from $|Z(\mathbf{q}, V)|^2$, the χ^2 goodness of fit test can be used to independently evaluate how well the Lorentzian peak functions represents the underlying data. To extract the noise, we take an area of $|Z(\mathbf{q}, V)|^2$ outside the highest $\mathbf{q}$-vector that contains a signal. A histogram of this area is made as a function of bias voltage, and an exponential function is fit to each histogram to yield the single distribution parameter. An exponentially distributed noise in the power spectrum is expected when the pre-transform data has Gaussian noise[67]. In this case, the standard deviation of the power spectrum is the variance of the un-transformed data. This method determines an implied Gaussian standard deviation as a function of bias voltage for each data set. See Fig. 2.10 for an example for the T_C= 88K sample.

By taking the single exponential distribution parameter, synthetic Monte Carlo noise data sets can be generated and propagated through all the processing, including the averaging described in Secs. 2.3, 2.4. The result is inevitably a central limit theorem Gaussian distribution for the processed data as in Fig. 2.11

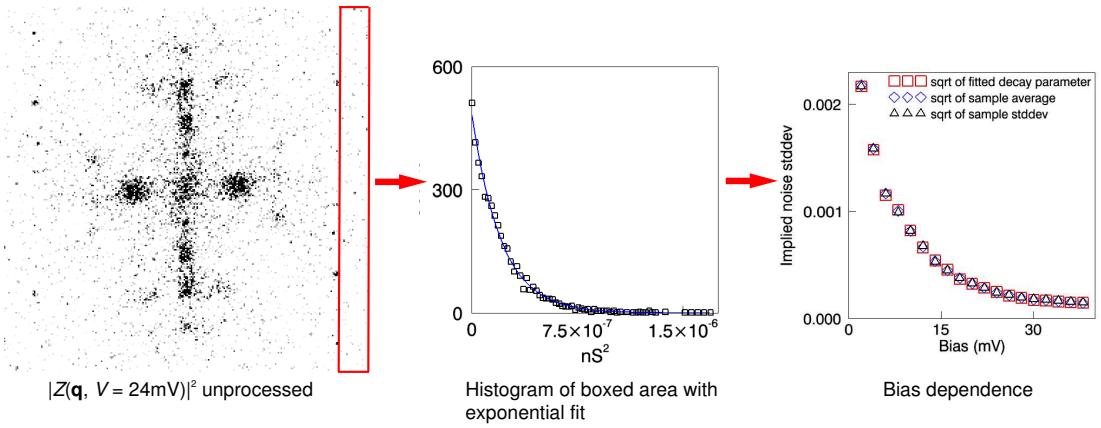

Figure 2.10: Determining noise from unprocessed $|Z(\mathbf{q}, V)|^2$

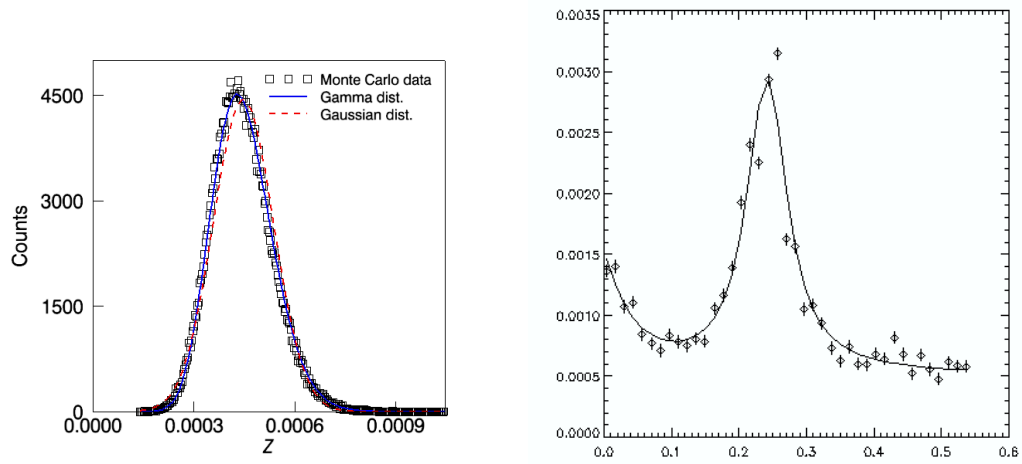

(a) Monte Carlo noise histogram for processed data

(b) Fit to $\mathbf{q_7}$. $\chi^2 = 518$ for 35 degrees of freedom.

Figure 2.11: Example of **q**-vector fit with Monte Carlo noise estimate

for the example in Fig 2.10. This means that the non-linear least squares fit is the maximum likelihood estimator, and the χ^2 goodness of fit test can give the statistical probability that the model is right[63]. Unfortunately, by this Monte Carlo technique for all ratio data analyzed the probability that the Lorentzian model is correct is zero within IEEE double precision accuracy. Fig. 2.11 shows an example fit where the lorentzian model has a zero maximum likelihood of being the correct model. However, by looking at this fit over the data it is also obviously quite a good representation. This means that within the noise presented here, there is room to improve the QPI model beyond the simple octet model approximation.

One difficulty with the above analysis is that it implies that the noise in $Z(\mathbf{r}, V)$ has a Gaussian distribution. But $Z(\mathbf{r}, V)$ is a ratio of two numbers with the same Gaussian distribution due to the amplifier noise present in the conductance measurements. Such ratios are known not to have Gaussian distributions[68]. Then the noise represented by Fig. 2.10 is likely not due to amplifier noise.

Many theories indicate that the FT-LDOS should have intrinsic noise from the random distribution of impurity sites[64, 69, 70, 71, 72]. However at present it is not known what the limiting source of noise is for $|Z(\mathbf{q}, V)|^2$.

CHAPTER 3

OCTET MODEL INVERSION TO MOMENTUM SPACE

"Space and time are modes by which we think, not conditions under which we live" - Albert Einstein[73]

3.1 Octet Equations and Algebraic Inverse

With the **q**-vectors extracted from the data, the octet model needs to be inverted. The symmetries of the square Cu-O lattice and the $d_{x^2-y^2}$ superconducting order parameter, Fig. 1.6, produce the following equations for the **q**-vectors, Eq. 1.10, in terms of the locations **k** of the momentum space poles:

$$\begin{aligned}
\mathbf{q}_1 &= (2k_x,\, 0) \\
\mathbf{q}_2 &= (k_x + k_y,\, k_y - k_x) \\
\mathbf{q}_3 &= (k_x + k_y,\, k_x + k_y) \\
\mathbf{q}_4 &= (2k_x,\, 2k_y) \\
\mathbf{q}_5 &= (0,\, 2k_y) \\
\mathbf{q}_6 &= (k_x - k_y,\, k_x + k_y) \\
\mathbf{q}_7 &= (k_x - k_y,\, k_y - k_x)
\end{aligned}$$

As implicit functions for **k** in terms of the $\mathbf{q_i}$, these equations are overdetermined. Explicitly, the combinations used are

$$\begin{aligned}
2k_x &= q_1,\, q_{2x} - q_{2y},\, q_{6y} - q_{6x},\, (q_3 - q_7)/\sqrt{2},\, q_5 - \sqrt{2}q_7,\, q_{4x} \\
2k_y &= q_5,\, q_{2x} + q_{2y},\, q_{6y} + q_{6x},\, (q_3 + q_7)/\sqrt{2},\, \sqrt{2}q_7 - q_1,\, q_{4y}
\end{aligned} \tag{3.1}$$

3.2 Over Determination and Statistical Sampling

In Sec. 2.5 it was shown that the random noise affecting the fit used to determine the **q**-vector is not well understood. This then makes the usual maximum likelihood estimators for the uncertainties in the inverted **k**-vectors unreliable. The overdetermined nature of Eqs. 3.1 offers a route to uncertainty estimation. With the numerous **q**-vectors at each bias voltage, these equations yield numerous values for the location of one point **k.** The methods of Secs. 2.3 and 2.4 give 5-9 statistically independent **q**-vectors. Note that the two orthogonal Cu-O directions have two statistically independent $\mathbf{q_1}$ and two statistically independent $\mathbf{q}_5$ values. By taking as many statistically independent combinations of Eqs. 3.1 as the data allows[44], a sample distribution is formed from which statistical estimates can be made. The sample mean value is the estimate for **k**, and the sample standard deviation is the estimate of the uncertainty. These create the data points and error bars that are plotted in Figs. below. In this sampling method, the components k_x and k_y are not statistically independent. Their correlation is estimated from their sample covariance, which is used when estimating the errors of quantities that are functions of **k**. The final step in inversion is to reflect each **k**-vector sample across the Brillouin zone (π, π) diagonal to completely populate the first quadrant.

By using this sampling method, errors due to systematic affects such as nonlinear shear of the controlling piezos (Fig. 1.1) and tip structure factor are included in the reported uncertainty. The consistency of these estimates is checked below by the value of χ^2 produced in least squares fits to the **k** statistics.

3.3 Fermi Surface and *d*-wave Quasiparticle Gap Determination

It was implied in Sec. that the octet QPI dispersion in the cuprates measures the $d_{x^2-y^2}$ electron excitation gap dispersion according to $\Delta_{\mathbf{k}} = eV$ for $eV < \Delta_{max}$. But since the locus of minimum excitation in momentum space tracks the normal state Fermi surface[14], by dropping out the bias dependence of from the inverted octet **k**-vectors the resulting set is a measurement of that surface. So the momentum space output of the octet QPI model consists of two things: an excitation gap, and a Fermi surface. For regular metals, these have separate sources. The Fermi surface is determined by the band structure, while the excitation gap is determined by the Cooper pairing potential. For strongly correlated oxides, like the cuprates, these issues are open scientific questions.

The while the octet model specifies how to invert **q**-vectors, is assumes no functional form for the Fermi surface or the gap dispersion. Following Ref. [44], the model Fermi surface is a least-squares one parameter fit of this **k**-space data to a quarter circle. The model fits as a function of doping at 4.2K are plotted over the **k**-vectors in Fig. 3.1 and the fit parameters are listed in Table 3.1, where we include the χ^2 divided by the degrees of freedom (D.O.F) statistic determined by the uncertainties specified in the previous section. The Fermi surface data derived from QPI does not reach the Brillouin zone boundaries. This is consistent with ARPES observations, where the Fermi surface states at the antinode have very low intensity due to the pseudogap, and the truncated Fermi surface has been named the 'Fermi arc'[59, 39].

To extract the *d*-wave gap dispersion, we parametrize each **k**-vector by its

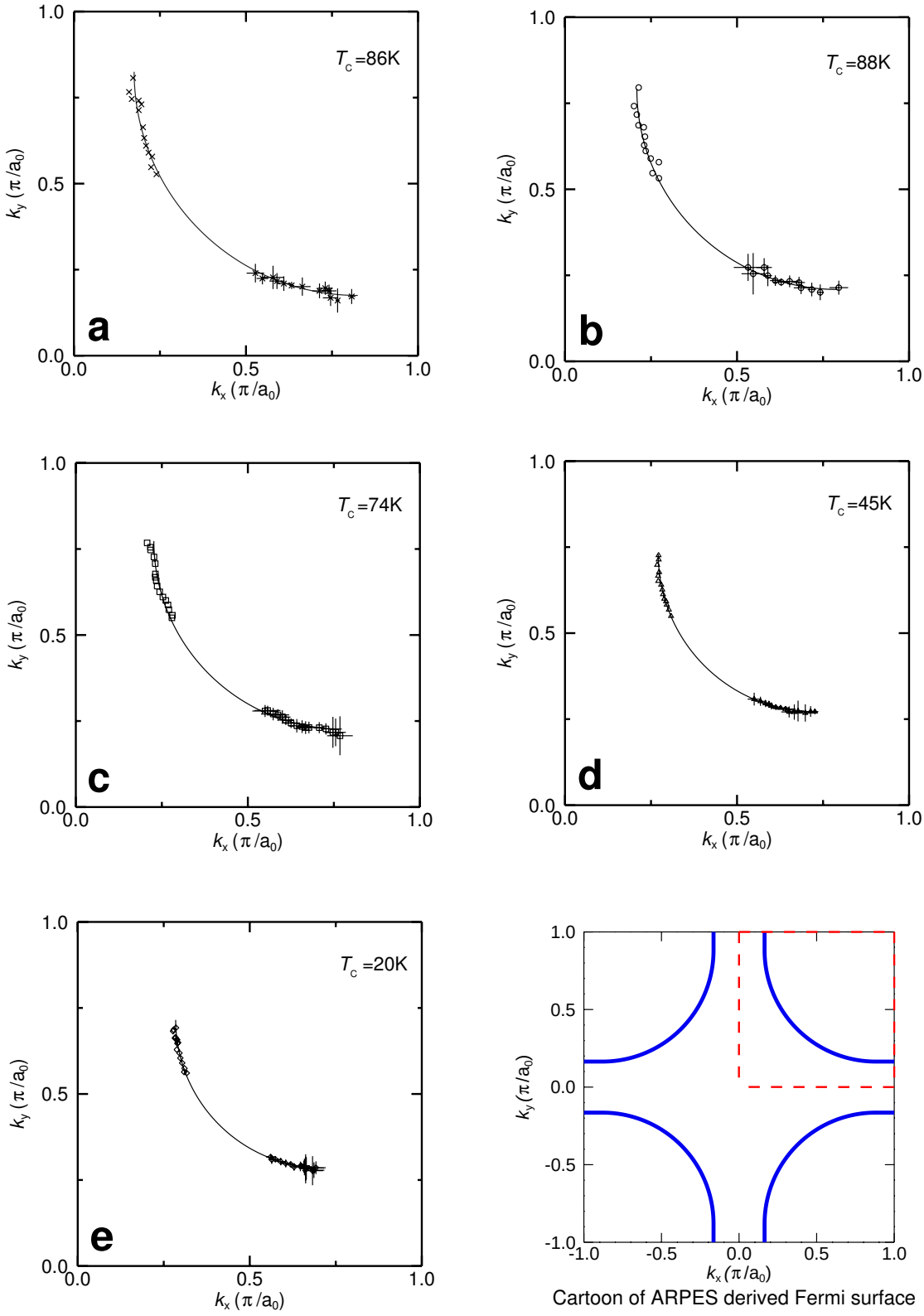

Figure 3.1: QPI-derived Fermi surfaces at 4.2K

Table 3.1: Doping dependence of QPI-derived Fermi surface model

Sample T_C (K)	Radius (π/a_0)	χ^2/(D.O.F)
86	0.65 ± 0.01	0.30
88	0.582 ± 0.009	0.28
74	0.557 ± 0.009	0.32
45	0.458 ± 0.004	0.045
20	0.431 ± 0.005	0.10

Table 3.2: Doping dependence of QPI-derived $\Delta_{\mathbf{k}}$ model

Sample T_C (K)	Δ_{QPI}(meV)	B	σ_Δ(mV)	χ^2/(D.O.F)
86	39 ± 2	0.82 ± 0.02	2	0.33
88	42 ± 3	0.87 ± 0.02	2	0.25
74	56 ± 3	0.81 ± 0.02	2	0.59
45	73 ± 6	0.77 ± 0.01	2	0.27
20	114 ± 12	0.715 ± 0.009	3	0.20

angle $\theta_{\mathbf{k}}$ about (π, π) and fit the gap to the function

$$\Delta(\theta_{\mathbf{k}}) = \Delta_{QPI}\left[B\cos(2\theta_{\mathbf{k}}) + (1-B)\cos(6\theta_{\mathbf{k}})\right] \tag{3.2}$$

This form was introduced earlier in ARPES studies[74] and has been found to describe both tunneling data[44] and electronic Raman spectroscopy[75]. These fits are made separately from the Fermi surface fits. The error on $\theta_{\mathbf{k}}$ is found from the k_x, k_y sample by including the covariance using partial derivative error propagation. The Δ error is the RMS bias modulation amplitude of the lock-in amplifier (see Appendix B) used to make the spectroscopic tunneling maps. The $\theta_{\mathbf{k}}$ points and corresponding fits are plotted for each doping in Fig. 3.2. The fit parameters are reported in Table 3.2. We find that the doping dependence of the parameter B is not inconsistent with that found by ARPES and Raman spectroscopy.

The χ^2/(D.O.F.) values reported in Tables 3.1 and 3.2 are systematically too low for the uncertainties determined by the method of Sec. 3.2 to be the true estimates. But because χ^2 is inversely proportional to these uncertainties, con-

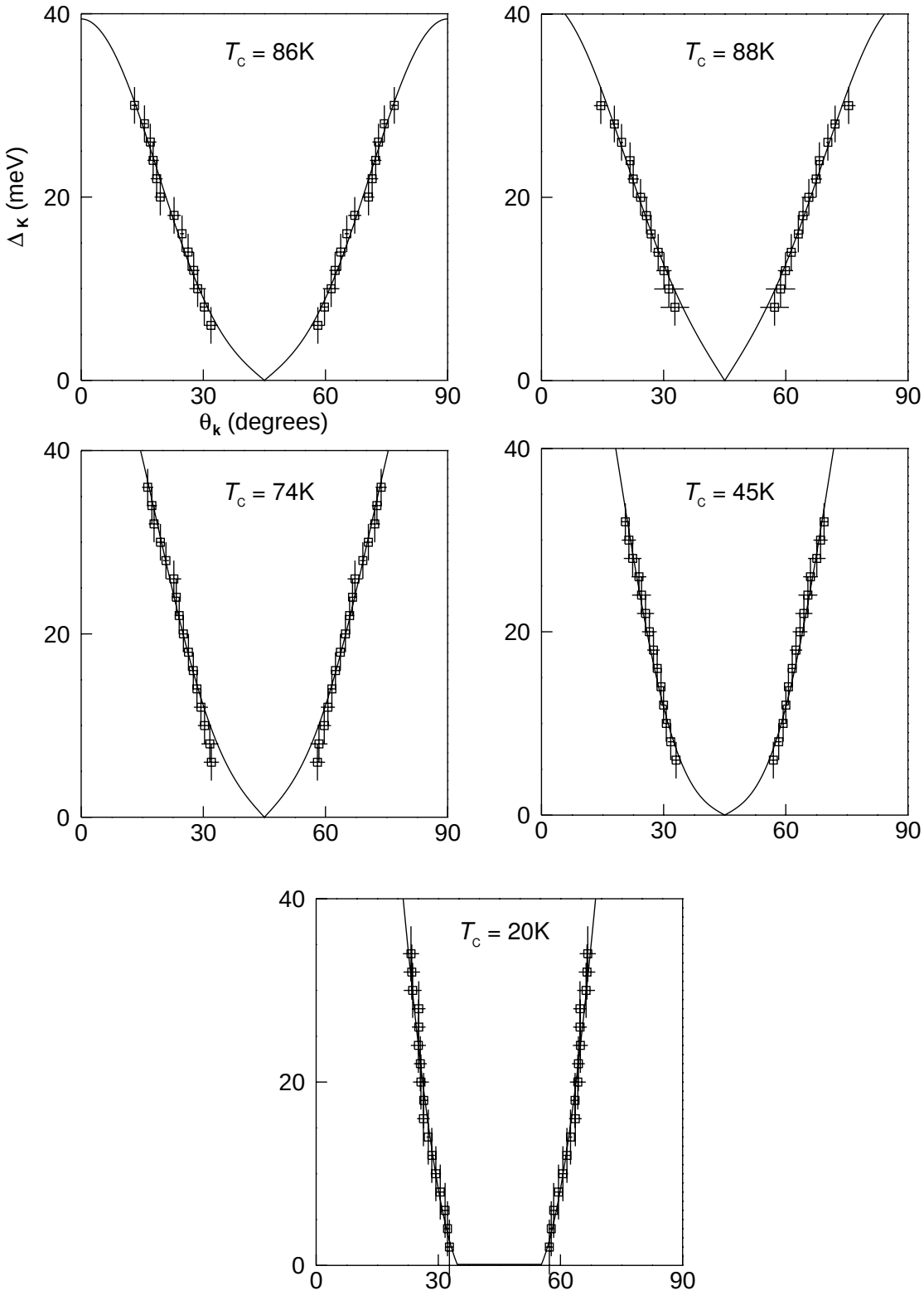

Figure 3.2: QPI-derived $\Delta_{\mathbf{k}}$ at 4.2K

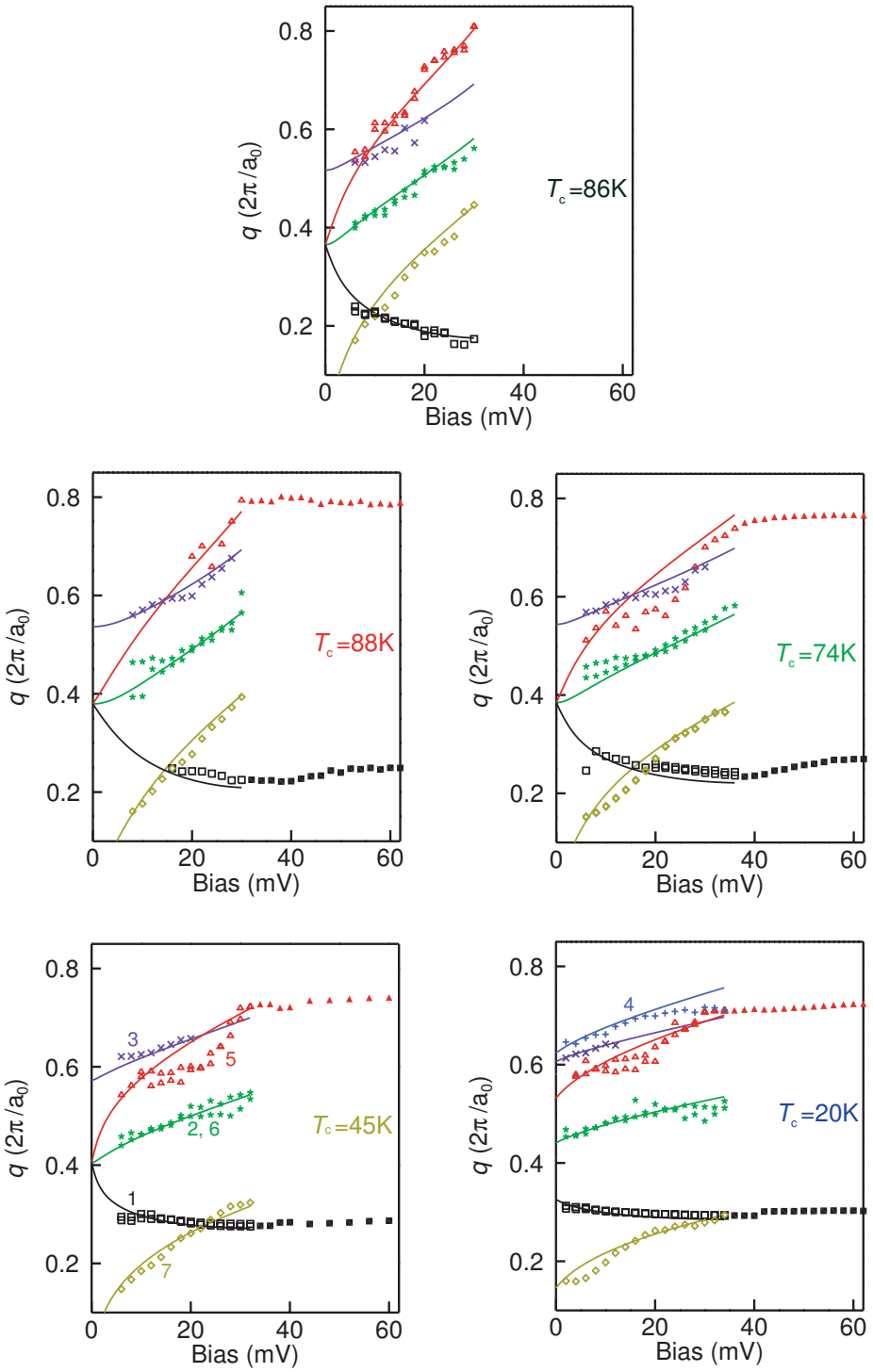

The symbols are the measured **q**-vectors as a function of bias voltage.
The solid lines are the scattering vectors of the octet model fit.

Figure 3.3: Doping dependence of **q**-vectors and model internal consistency

sistency with the χ^2 test means that they are too large. Under the assumption that these sample statistics are Gaussian, then all the uncertainties reported here are very conservative. To be sure, this assumption is unverified, and the limiting source of uncertainty has not been determined.

In this section, the doping dependence at 4.2K of the inverted octet QPI model are presented. The temperature dependent data for the T_C= 42.5K are presented in Ch. 4.

3.4 Internal Consistency of Momentum Space Model

We emphasize that the octet inversion outlined above is not a direct fit of the model to the spectroscopic data. But with 5-9 **q**-vectors measuring the same **k**-vector, the model is heavily over determined, allowing us to replace the statistical sample by its mean and standard deviation in the above **k**-space fits. To demonstrate the degree of internal consistency of this statistical model we plot as solid lines in Fig. 3.3 the **q**-vectors that the model fits generate over the experimentally measured **q**-vectors (symbols). Again, the data presented here are for the doping dependence at 4.2K. The temperature dependent **q**-vector data for the T_C= 42.5K are presented in Ch. 4.

CHAPTER 4

EVOLUTION OF QUASIPARTICLE INTERFERENCE WITH DOPING

"Regretfully, nowadays the contents of the theorem are so densely clouded by folklore that it is sensible to begin with a statement what is meant when I say 'the Luttinger theorem'." - Igor Dzyaloshinskii[77]

4.1 Fermi Arc Diminishing with Doping and the Luttinger Theorem

The doping evolution of the Fermi surface becomes clear when the data and models in Fig. 3.1 are plotted on the same graph, as shown in Fig. 4.1a. The QPI derived Fermi surface is seen to decrease monotonically with doping, consistent with Luttinger's theorem[76]. This theorem equates twice the area enclosed by the Fermi surface to the density n of delocalized electrons in the system. By following the ARPES derived Fermi surface[39] suggested in the bottom corner of Fig. 3.1, the QPI Fermi arc can be extended to the Brillouin zone boundaries with vertical lines, and the Luttinger theorem can be applied to the resulting contour to count n. Because p in the cuprates measures the hole density relative to half filling, the relation $1 - n = p$ can be used in Fig. 4.1b(red diamonds) to compare to the estimated p in Table 2.1. Perhaps surprisingly, it is found that the traditional Luttinger count fails by a significant amount.

The ends of the QPI Fermi arc are observed to to fall along a line connecting the $(0, \pi/a_0)$, $(\pi/a_0, 0)$ Brillouin zone points, plotted by the dashed line in Fig. 4.1a. If twice the area between the arc and the $(0, \pi/a_0) - (\pi/a_0, 0)$ line is used

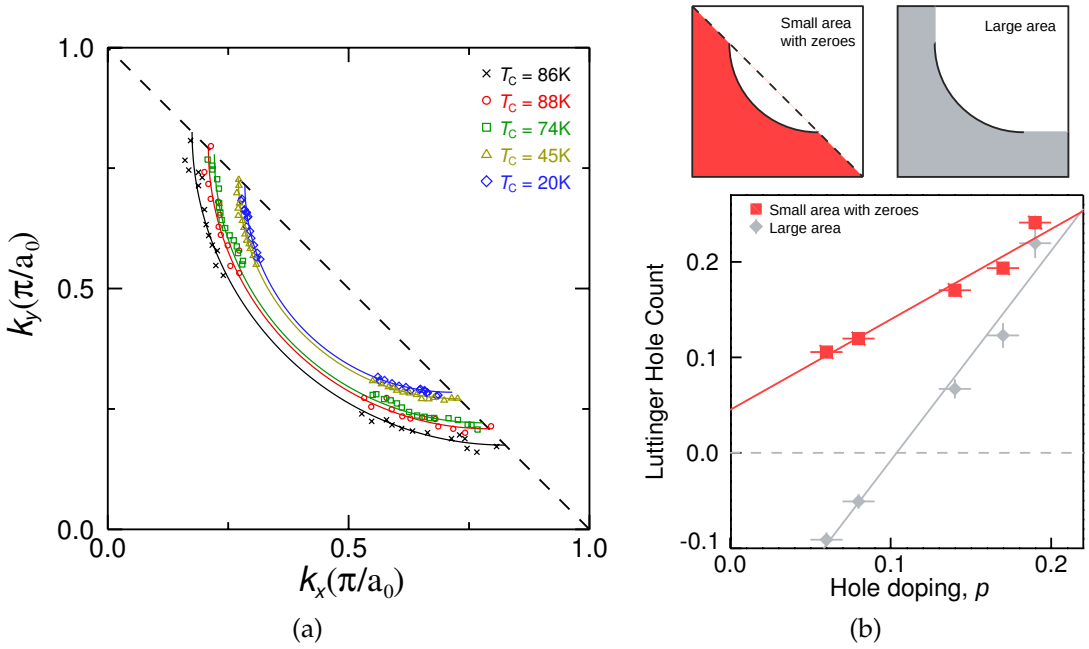

Figure 4.1: Doping evolution of the Fermi surface and Luttinger count

to estimate p, the result, shown in Fig. 4.1b (black squares) is in much better agreement with Table 2.1. What is going on here? The failure of the Luttinger theorem shouldn't be surprising, because it is based on perturbation expansion in powers of the electron interaction. At half filling, $p = 0$, the cuprates are Mott insulating antiferromagnets. This ground state cannot reached by perturbation expansion from the non-interacting band theory, according to which these materials should be metals with $p = 1$. The incorrect hole count from the large Fermi surface area means that at low doping the normal state of the cuprates also is not preturbatively connected to the non-interacting theory. To count the electrons in a strongly interacting band, the Luttinger theorem must be generalized to include contours of zeroes at the chemical potential in the single particle Green's function as well as the poles[77]. The good estimate of the hole count provided by the small Fermi surface area is consistent with the generalized Luttinger theorem if the single particle Green's function has a contour of zeroes

along the $(0, \pi/a_0) - (\pi/a_0, 0)$ line. The distinction between electron counting in the large and small area Fermi surfaces is shown schematically in Fig. 4.1b on the right.

While the generalized Luttinger theorem counts the occupied electron number in correlated bands, not all are delocalized and contribute to the carrier density. The contours of poles at the chemical potential enclose states with an approximate simple pole near the chemical potential that represent propagating, if damped, waves that can carry a current if phase space permits. The contours of zeroes at the chemical potential enclose states where the pole structure of the simple theory has been destroyed by an interaction-induced divergence in the self energy. These states cannot carry current. Counts of carrier density from the low temperature Hall coefficient and Drude weight in optical conductivity both show that number of carriers are driven to zero linearly as $p \to 0$ [78, 79]. The small area hole count in Fig. 4.1b shows that the QPI Fermi arc is not inconsistent with the transport data if there is a contour of poles connecting the arc tips along the $(0, \pi/a_0) - (\pi/a_0, 0)$ line. The main inconsistency is the implied non-zero intercept at zero doping, but this might be due the limitation of representing these contours with a quarter circle and straight line. Fig. 4.2 shows the pole contours of a more sophisticated Green's function[80] with a contour area that vanishes with the doping.

In contrast, in the non-interacting theory these materials should be have a hole carrier density of $1 + p$ [81]. Interestingly, the slope of the line through the small area count in Fig. 4.1b is 1, while the slope of the line through the large area count is 2.

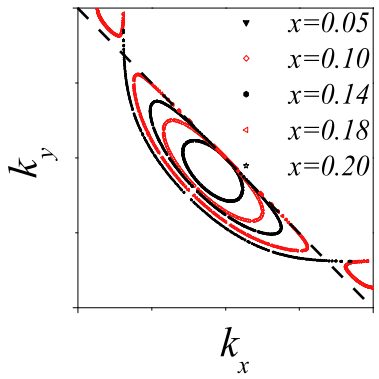

Figure 4.2: Proposed Fermi surface of Ref. [80]

4.2 Evolution of the Quasiparticle Interference Gap

The doping dependence of the QPI *d*-wave gap is summarized in Fig. 4.3. There are several features in these graphs. The gap slope at $\theta_{\mathbf{k}} = 45^{\circ}$ decreases with doping, until finally for the T_C = 20K underdoped sample the data indicate that the nodal point has collapsed to a finite line of zero energy excitations. Except for this sample, this is consistent with the doping dependence of the gap slope inferred from low temperature thermal conductivity data [citation?] and also direct ARPES measurements. This is remarkable because there are no data points at gap energies comparable to those probed by thermal conductivities. It is inferred from extrapolation of Eq. 3.2, a function chosen because $\Delta = \Delta_0 \cos(2\theta_{\mathbf{k}})$ fails to fit the data. One limiting factor in acquiring QPI data at the lowest biases is the strong increase of noise in the ratio Z as the bias approaches the chemical potential, see Fig. 2.10.

Another feature is that where there are data points, the slope is increasing monotonically as the doping is reduced, while the data point of highest gap energy changes only weakly. This is discussed further in Sec. 4.3.

Most striking though, is that Δ_{QPI} of Eq. 3.2 increases monotonically as the

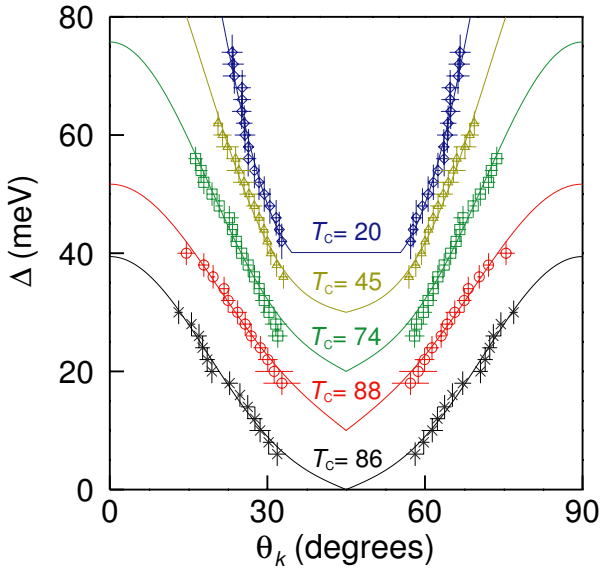

Figure 4.3: Doping evolution of Δ_{QPI}

doping falls towards the Mott insulating state (Table 3.2). If these materials were traditional BCS-Eliashberg superconductors with a large area Fermi surface, then Δ_{QPI} would be the maximal pairing amplitude setting the scale for T_C, which would be fantastically high. It is important to remember that Δ_{QPI} is an extrapolation to a **k**-space region outside of available data points where the generalized Luttinger theorem indicates there are no Green's function poles. Without appeal to other measurements, such deductions based on its value are dubious. Both the doping dependence and absolute scale of Δ_{QPI} agree with ARPES data[39, 82, 83], where the excitation gap at the antinode is known as the 'pseudogap' and is the source of the truncated Fermi arc in the normal state.

4.2.1 Relationship to the Real Space Gap Map $\Delta(\mathbf{r})$

An understanding of the relationship between the inferred QPI gap and the real space excitation gap revealed by the gap map $\Delta(\mathbf{r})$ (See Figs. 1.2b and 1.3b)

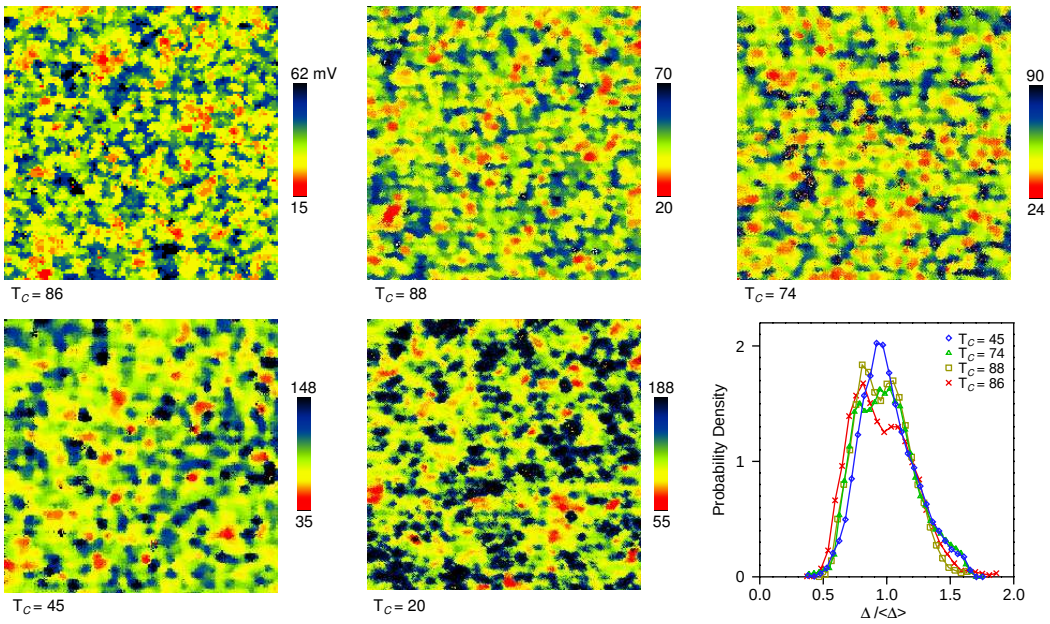

Figure 4.4: Doping evolution of $\Delta(\mathbf{r})$

requires a brief review of established properties. This will be done by analyzing gap maps acquired in the same nanoscale surface area used to determine the QPI properties. Fig. 4.4 presents these gap maps for each sample studied. At each doping the gap maps all have the same spatial structure, consisting of patches of size ~3nm^2 with the same local gap value[23, 24]. As $p \rightarrow 0$, the distribution of gap values across the patches changes so that the mean value $\langle \Delta(\mathbf{r}) \rangle$ increases[24, 84, 85, 86]. This distribution changes with doping such that rescaling by the mean value causes the distributions to collapse to the same doping independent curve[86]. This is demonstrated for the samples studied by the graph in the lower right corner of Fig. 4.4.

The local conductance curves are also varying with the gap size. Each local patch of the same $\Delta(\mathbf{r})$ value has its own characteristic spectroscopic lineshape that changes little across doping. So a gap patch with $\Delta = 50$meV has a nearly identical LDOS curve for both the overdoped T_C = 86K sample and the under-

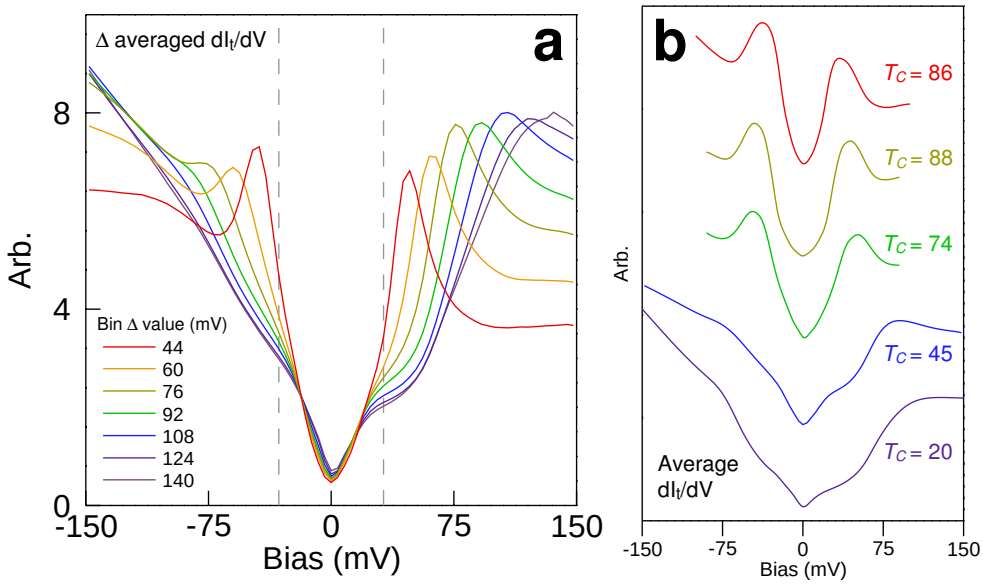

Figure 4.5: Doping evolution of averaged conductance

doped T_C = 45K sample. As the gap size increases, the coherence peak height relative to the background decreases and broadens[84, 85]. The evolution of these features with $\Delta(\mathbf{r})$ is displayed in Fig. 4.5a, produced by averaging the local curves with the same value of $\Delta(\mathbf{r})$ for the T_C = 45K gap map in Fig. 4.4. These features, along with a gap size variance that increases as the doping decreases, creates the averaged conductance curves in Fig. 4.5b. The coherence peak in the averaged conductance has disappeared as doping decreases by underdoped T_C = 64K[84, 85].

As the doping falls towards zero, the gap determined by real space spectroscopy and the gap inferred from the QPI dispersion both evolve in a continuous fashion. In Fig. 4.3 we see that both average of the gap map $\langle\Delta(\mathbf{r})\rangle$ and the QPI gap Δ_{QPI} agree well. This would be the expected if the underdoped cuprates were BCS-Eliashberg superconductors with a large area Fermi surface. But given the implied **k**-space pole structure from the generalized Luttinger theorem, it is not clear whether Fig. 4.3 represents a coincidence or if it represents

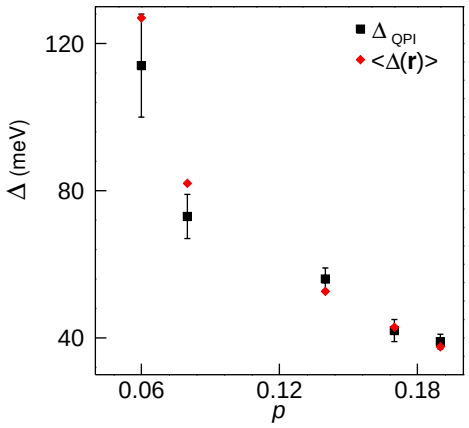

Figure 4.6: Relation between Δ_{QPI} and $\langle \Delta(\mathbf{r}) \rangle$

a real relationship between the excitation gap of the low energy quasiparticles and the higher energy states near $\Delta(\mathbf{r})$.

Finally, the gap map data in Fig. indicates that T_C = 20K has a gap map spatial structure that deviates from the other samples. This is at least partially due to poor tip resolution, which cannot resolve the spectroscopic structure of the oxygen atoms. The LDOS at $\omega = \Delta(\mathbf{r})$ is known to have strong contrast variation across subunit cell Cu-O-Cu bonds for T_C = 45K [55, 87].

4.3 Loss of Dispersion and Fermi Arc Termination

Figs. and summarize the octet model inverted locus of minimal excitation gap $|\Delta_{\mathbf{k}}| = eV$. As the bias voltage moves farther away from the chemical potential, the octet **k**-vectors disperse away from the nodal region. At a certain bias voltage, the **k**-dispersion suddenly terminates. Fig. 4.7 plots the gap dispersion at every bias voltage, showing that the octet dispersion terminates at the bias voltage shown by the dashed grey line. This bias voltage is identical to within the several millivolt uncertainty of the average 'kink' energy observed in the real-

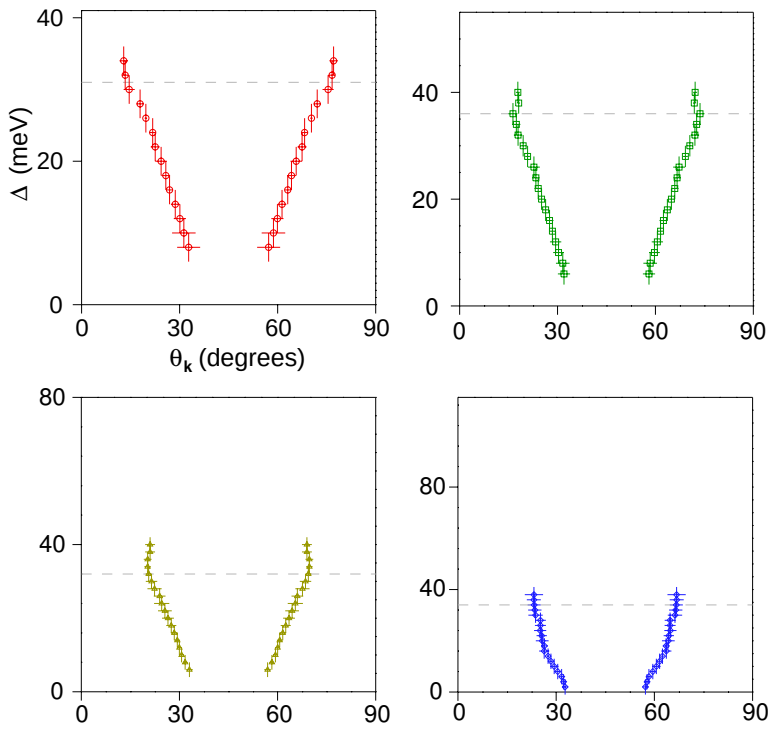

Figure 4.7: Loss of dispersion in $\Delta_{\mathbf{k}}$

Table 4.1: Termination point deviation from $(0, \pi/a_0) - (\pi/a_0, 0)$ line

T_C (K)	Δk (π/a_0)	k_x (π/a_0)	k_y (π/a_0)
86	0.015	0.022	0.011
88	0.007	0.020	0.027
74	0.018	0.057	0.037
45	0.0012	0.0081	0.010
20	0.016	0.019	0.029

space spectroscopy of underdoped cuprates[24, 86, 88, 89]. The kink energy is a weak inflection point identified by a local minimum in $d^2I_t/dV^2\,(\mathbf{r}, V)$[86], and is visible in Fig. 4.5 near the grey dashed lines marking the QPI termination energy. Real-space spectroscopy has identified that below the kink energy the excitations are homogeneous, whereas above this energy they exhibit strong heterogeneity. This can be seen for the gap-averaged spectra in Fig. 4.5, and a striking example is visible in Fig. 3 of Ref [24].

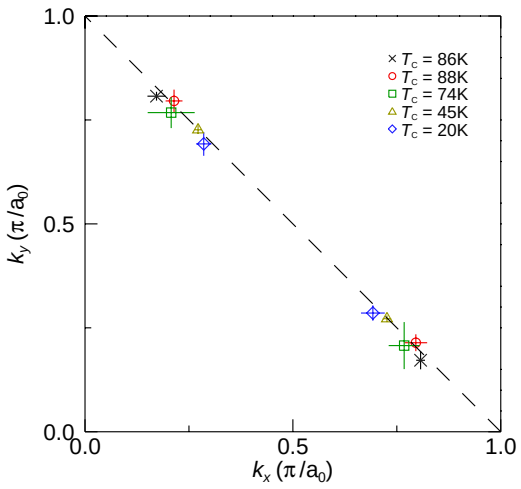

Figure 4.8: Fermi arc termination points

The point in **k**-space where the octet model dispersion terminates is near the $(0, \pi/a_0) - (\pi/a_0, 0)$ line, within the octet sample error. Fig. graphically shows the relationship between the termination point for each doping and the $(0, \pi/a_0) - (\pi/a_0, 0)$ line. Table 4.1 lists for each doping the deviation Δk of the terminating **k**-point from the $(0, \pi/a_0) - (\pi/a_0, 0)$ line, and the octet sample standard deviations $\delta k_x, \delta k_y$ which represents the uncertainty. Just as the dispersion stops, the peak amplitudes of $\mathbf{q}_2$, $\mathbf{q}_3$, $\mathbf{q}_6$, and $\mathbf{q}_6$ decay away until they approach the noise floor and disappear a few millivolts later. This is show in Fig. 4.9a-d. In contrast, the $\mathbf{q_1}$ and $\mathbf{q}_5$ peaks remain well above the noise floor beyond the dispersive termination. In the non-dispersive regime we label these $\mathbf{q}_1^*$ and $\mathbf{q}_5^*$ and plot with the filled symbols in Fig. 3.3. The peak amplitudes for $\mathbf{q_1}$, $\mathbf{q}_1^*$ and $\mathbf{q}_5$, $\mathbf{q}_5^*$ are shown in Fig. 4.9e-f. This behavior of dispersive **q**-vectors at low biases followed by a loss of dispersion at high bias was demonstrated by ARPES autocorrelation studies of the superconducting state[51].

From the introduction to octet QPI in Sec. 1.4, it is the **q**-vectors spanning regions of **k**-space with opposite order parameter sign that disappear as dispersion is lost. In contrast, the amplitudes of the **q**-vectors spanning regions of

the same order parameter sign maintain an appreciable signal and become non dispersive.

4.4 Doping Dependence of Non-Dispersive q-Vectors

The non-dispersive wave-vectors $\mathbf{q_1^*}$ and $\mathbf{q_5^*}$ at biases above the termination energy follow the doping dependence of the Fermi-arc termination. This is illustrated by the arrows in the schematic Brillouin zone of Fig. 4.10a. These non-dispersive features are not harmonics tied to a static $4a_0$ modulation: $\mathbf{q_1^*}$ is not locked at $(1/4)\times(2\pi/a_0)$ and $\mathbf{q_5^*}$ is not locked at $(3/4)\times(2\pi/a_0)$ although their sum adds to $2\pi/a_0$. Thus we demonstrate that they are determined by the point of intersection of the Fermi arc and the $(0, \pi/a_0) - (\pi/a_0, 0)$ line. This is displayed in the Z($|\mathbf{q}|$) data along the Cu-O bond direction of Fig. 4.10c which shows the evolution of the 48 mV $\mathbf{q_1^*}$ and $\mathbf{q_5^*}$ peaks with doping. We focus in Fig. 4.10d on the $\mathbf{q_5^*}$ peak from these data, overlaying the fits used to extract the peak location as well as the terminating k_y point determined from Fig. 4.7.

In Sec. 1.5 it was demonstrated through Fig. 1.7 and Eq. 1.15 that checkerboard modulations in low bias tunneling conductance have their origin in the LDOS integrated to the setpoint bias (denominator of Eq. 1.15) and not the LDOS itself (numerator of Eq. 1.15). This means that the states responsible for the checkerboard patterns come from higher energies in the integral. In particular, Fig. 1.7 and Eq. 1.15 suggests that for T_C = 45K underdoped $Bi_2Sr_2Ca_{0.8}Dy_{0.2}Cu_2O_{8+\delta}$ a large contribution to the checkerboard comes from empty states lying between +50 and +100meV. These are the same energies where the non-dispersive peaks marking the ends of the Fermi arc are observed.

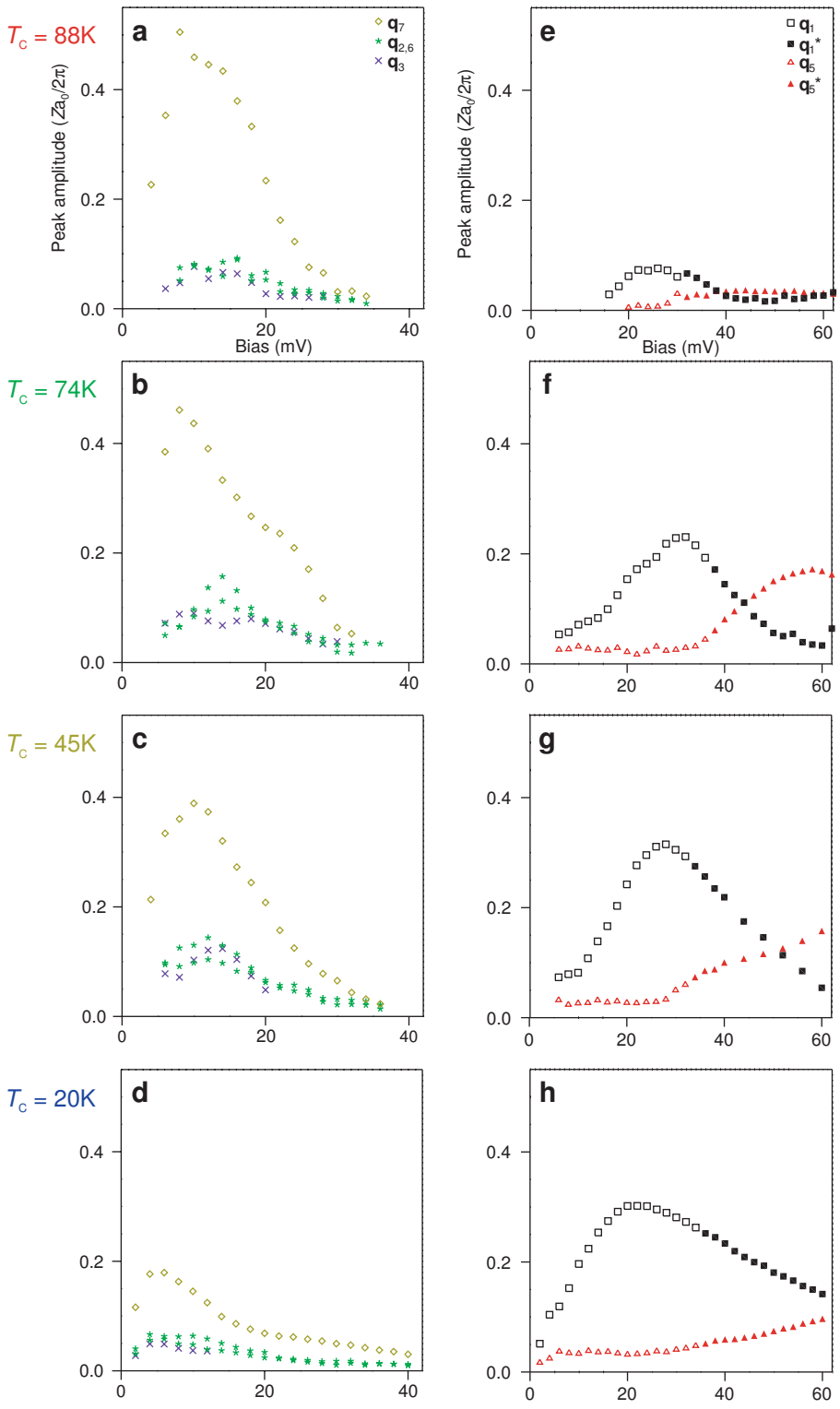

Plots of the peak amplitude density for the scattering vectors **a-d:** $\mathbf{q}_2$,$\mathbf{q}_3$,$\mathbf{q}_6$, and $\mathbf{q}_7$. **e-h:** $\mathbf{q}_1$ and $\mathbf{q}_5$. Comparison of the peak amplitudes for the T_C=86K data set cannot be made because the analysis was performed on conductance maps which suffer from the constant current setup effect.

Figure 4.9: Evolution of **q**-vector peak amplitude with doping and bias.

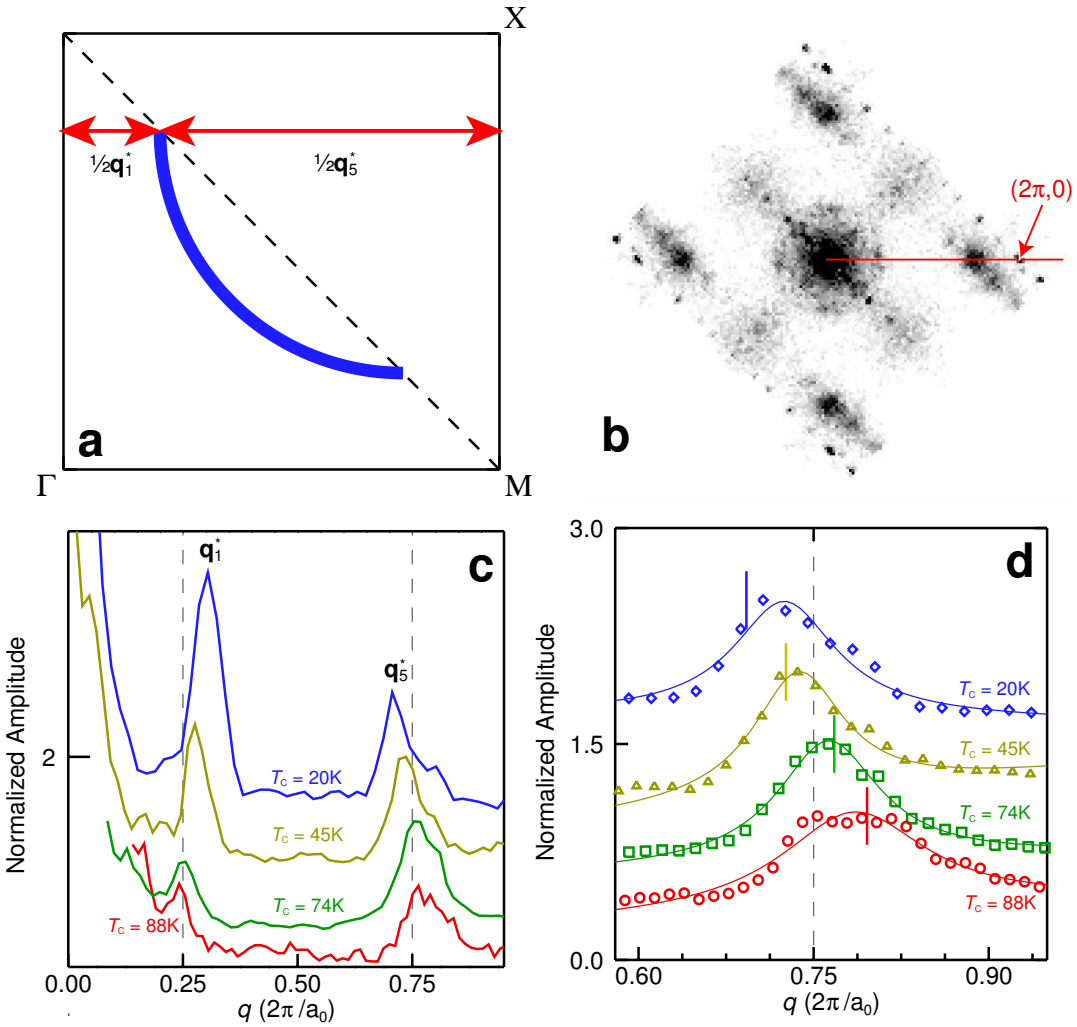

b. $Z(\mathbf{q}, V = 48\text{mV})$ for $T_C = 74$K. The red line schematically indicates the source of the data in c. and d. The arrow locates the Cu reciprocal lattice vector. The other parts to the figure are described in the text.

Figure 4.10: Non-dispersive wave vectors inferred from Fermi arc end points

Further, the characteristic wave-vectors of the checkerboard change with doping consistent with the change of the Fermi arc relative to the $(0, \pi/a_0) - (\pi/a_0, 0)$ line[90]. These two observations suggest that the loss of both QPI dispersion and electronic homogeneity have the same physical source as the checkerboard and that the wave vectors characterizing its patterns are determined by the terminating points of the Fermi arc.

4.5 Simultaneous Real-Space and Momentum-Space Determination

For energies above the termination energy where QPI dispersion is lost, $Z(\mathbf{q}, V)$ becomes rather static and featureless. However, because this crossover energy is the same point where local electronic homogeneity is lost, the real space $Z(\mathbf{r}, V)$ develops complex structure as disorder sets in. The excitations become better defined in real-space than in momentum-space. This is displayed for T_C = 45K in Fig. which can be compared to Fig. 2.1. The higher real space resolution in Fig. 4.11 emphasizes the local nature of the excitations. The patterns visible are short correlation length $4a_0$-wide Cu-O-Cu bond-centered unidirectional domains. The individual domains are fairly disperse and embedded in a glassy background. They appear similar to those reported in Refs [28, 55] for the current ratio maps $R(\mathbf{r}, 150\text{mV}) = I_t(\mathbf{r}, +150\text{mV}) / I_t(\mathbf{r}, -150\text{mV})$. The difference here is that while the glassy domain structure is more or less constant in energy, there are strong fluctuations in the intensity of the $Z(\mathbf{r}, V)$ maps. The intensity appears approximately constant across ~3nm size patches.

In Sec. 4.2.1, it was reviewed that the gap map $\Delta(\mathbf{r})$ exhibits a nearly identical structure. By comparing Fig. 4.11a-c with the simultaneously acquired gap map of Fig 4.11d., $Z(\mathbf{r}, V)$ appears to exhibit the strongest intensity for the locations $\mathbf{r}$ that satisfy $\Delta(\mathbf{r}) = eV$. (Note the markers in the color scale). As a quantitative test, Fig. 4.12 compares the image $Z(\mathbf{r}, V = \Delta(\mathbf{r}))$ to $R(\mathbf{r}, 150\text{mV})$ side by side. The intensity fluctuations are gone, and the patterns are now identical to those in R. Further, the energy at each location $\mathbf{r}$ can be rescaled to the value $\Delta(\mathbf{r})$ at that location, defining a new local energy scale $e(\mathbf{r}) = V/\Delta(\mathbf{r})$.

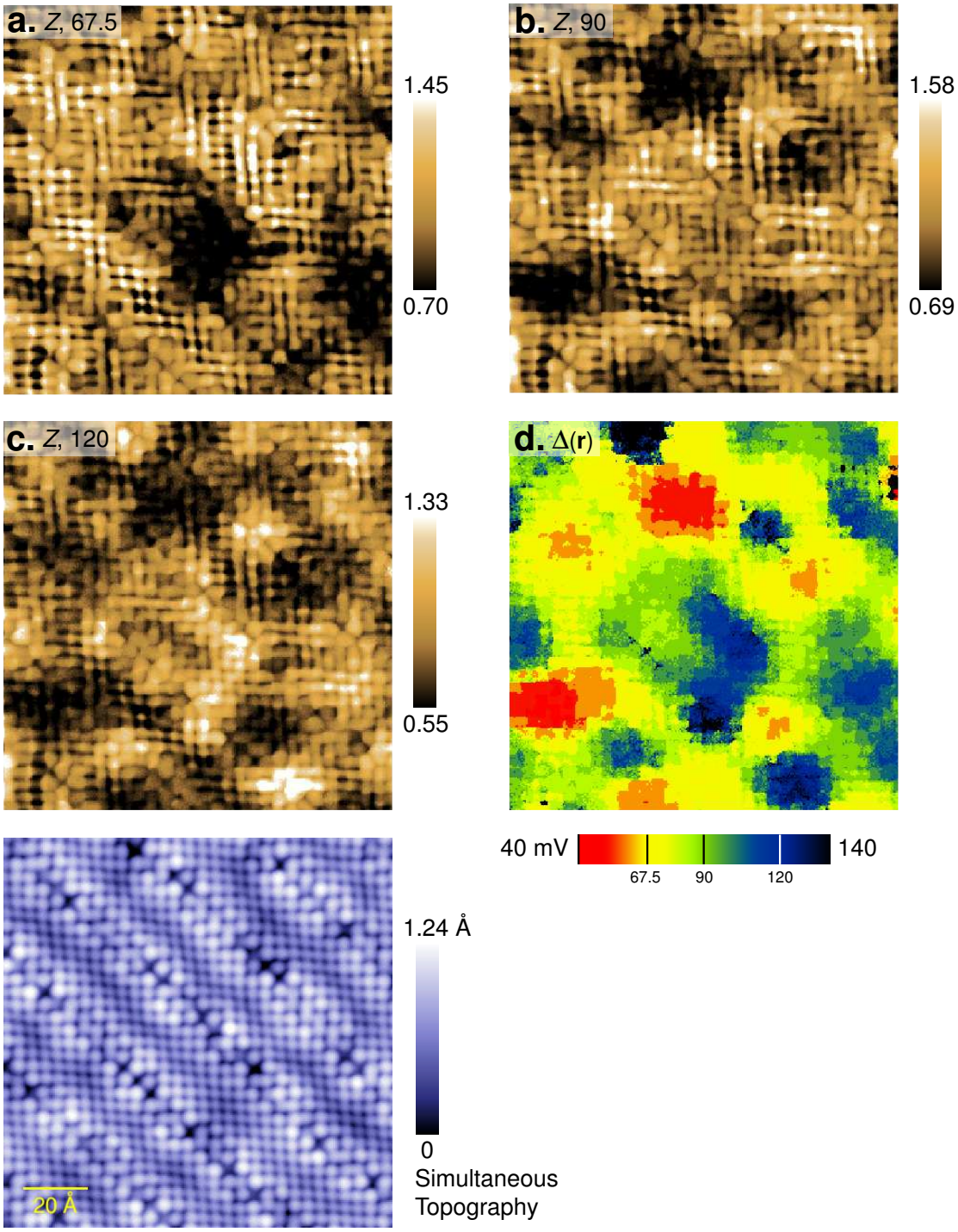

Figure 4.11: Z disorder above QPI termination bias

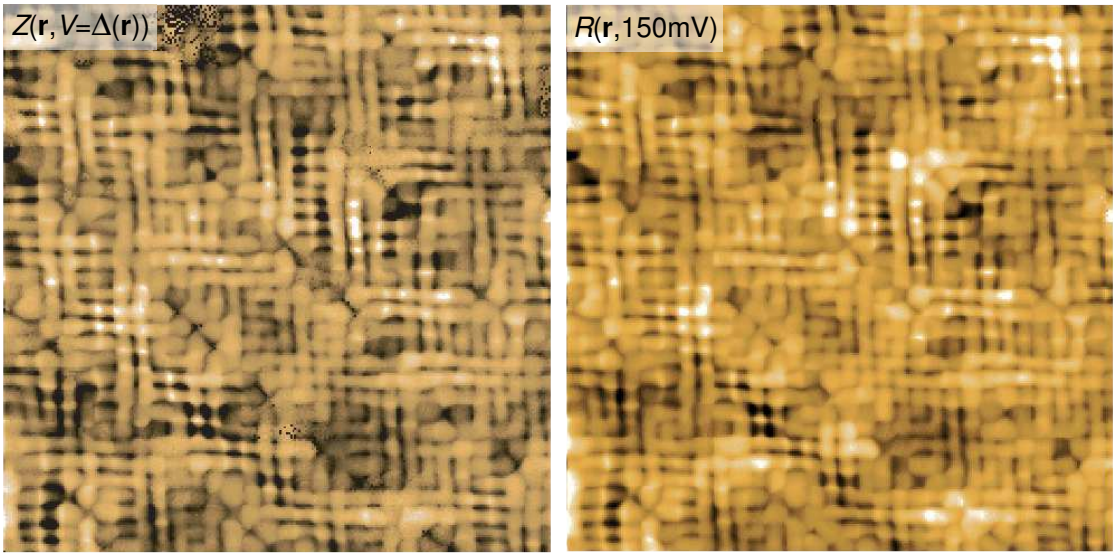

Figure 4.12: $Z\left(\mathbf{r},\Delta\left(\mathbf{r}\right)\right)$compared to $R\left(\mathbf{r},150\text{mV}\right)$

Fig. 4.13 plots $Z\left(\mathbf{r},e\right)$ from the data of Fig. 4.11 for several values of e, each image with identical absolute color scale. Two features are prominent. The images have maximum intensity at $e=1$, demonstrating that the Cu-O-Cu bond centered patterns of the electronic cluster glass in Refs [28, 55] are the atomic scale structure of excitations to the local gap $\Delta\left(\mathbf{r}\right)$. The other feature we see is that away from $e=1$, the images continue to exhibit the same pattern. The source of inhomogeneity in $\Delta\left(\mathbf{r}\right)$ must also be the source of inhomogeneity for the electronic excitations that lie between the termination energy and $\Delta\left(\mathbf{r}\right)$. One source of $\Delta\left(\mathbf{r}\right)$ disorder with strong experimental evidence is the random distribution of dopant atoms that provide the hole carriers[54, 42].

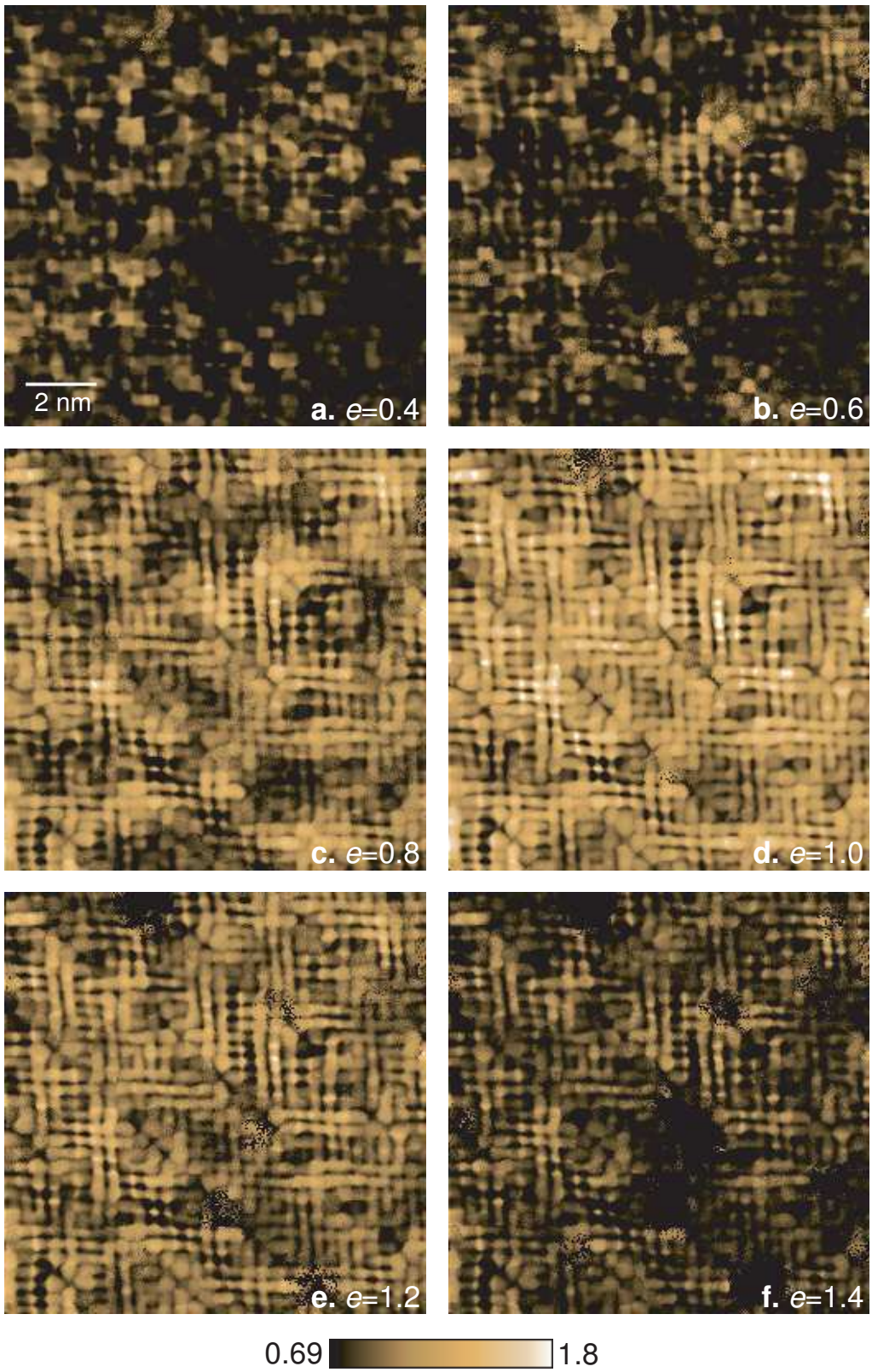

Figure 4.13: Z scaled in energy by $e(\mathbf{r}) = V/\Delta(\mathbf{r})$

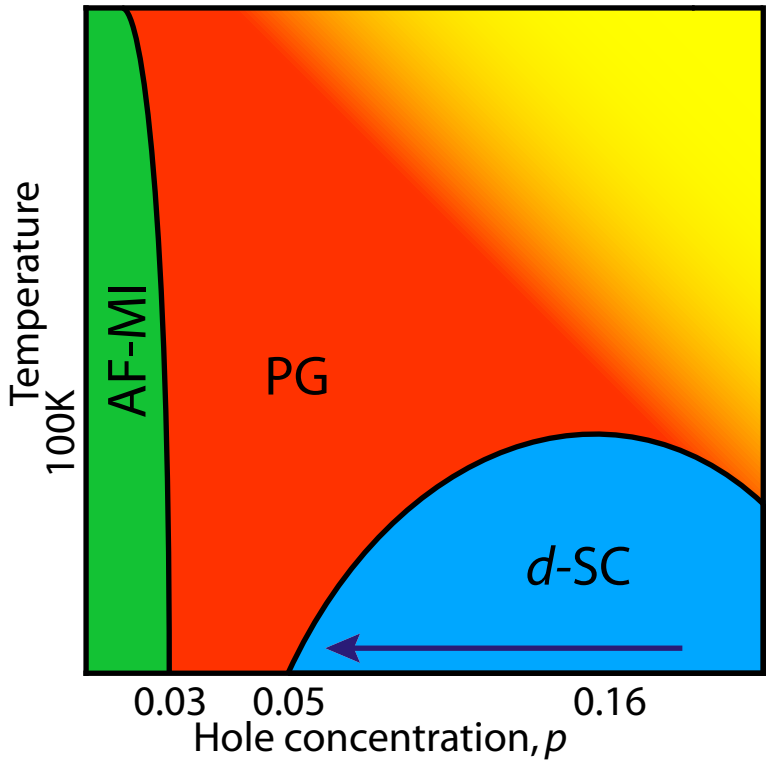

Figure 4.14: Phase diagram trajectory probed by QPI in this chapter

4.6 Summary

At low biases near the chemical potential, a homogeneous electronic structure well defined in momentum space is observed. Consistent with this, *d*-wave superconducting QPI patterns are observed to disperse out to a crossover energy where a certain class of **q-**vectors disappear and non dispersive behavior sets in. At this energy, electronic homogeneity is lost as detected by kinks in real space spectroscopy while in momentum space this corresponds to the location where the Fermi arc intersects the $(0, \pi/a_0) - (\pi/a_0, 0)$ line. Above this energy, the real space patterns exhibit fluctuating glassy short range $4a_0$ wide Cu-O-Cu patterns that are characteristic of excitations to the disordered local gap $\Delta(\mathbf{r})$ energy. It is observed that Δ_{QPI} of the homogeneous low energy QPI model for momentum space is quantitatively the same as the average $\langle \Delta(\mathbf{r}) \rangle$. Because homogeneity is lost, the physical basis for this is unknown, but it is consistent with the momentum space gap continuity in the ARPES observations of Kanigel *et. al.* [91]. The evolution of Δ_{QPI} is followed as the doping is reduced towards the Mott insulating state along the phase diagram trajectory of Fig. 4.14. It is observed that Δ_{QPI} increases directly with the pseudogap energy, even as both T_C and the superfluid density are reduced to near zero.

CHAPTER 5

EVOLUTION OF QUASIPARTICLE INTERFERENCE WITH TEMPERATURE

"Every time we look at another experiment, we make the problem easier. It is like looking in the back of the book for the answer, which is slowly being unveiled by the details of the various experiments. There is no reason to require the experiments. The only reason that we cannot do this problem of superconductivity is that we haven't got enough imagination" Richard P. Feynman[92]

5.1 The Pseudogap and Phase Incoherent Superconductivity

By tracking the quasiparticle interference for $T \ll T_C$ it was deduced that the excitation gap of BCS-like quasiparticle in the underdoped cuprates is strongly impacted by the heterogeneous pseudogap. This is puzzling. Because it does not vanish at T_C, the pseudogap cannot be a BCS superconducting gap. In the underdoped cuprates, the convergence of a layered CuO_2 structure and a superfluid density very much below the valence density[93] conspire to make the superconducting order susceptible to fluctuations, and specifically phase fluctuations [94, 95]. Then thermal unlocking of the superconducting phase would drive T_C below the mean-field, BCS value which is controlled by the ground state superconducting gap. However, above T_C the pairing mechanism is still active over microscopic correlation lengths and a superconducting amplitude can persist. For instance, consider the superconducting order parameter $\left\langle c_{\mathbf{k}\uparrow} c_{-\mathbf{k}\downarrow} \right\rangle = |\Delta(\mathbf{k})| e^{i\phi}$. In a simple scenario of thermal unlocking[14], the

phase acquires a finite correlation length above T_C, $\langle \phi(\mathbf{r})\,\phi(\mathbf{r}+\mathbf{R})\rangle \propto e^{-R/L}$. This leads to a complex order parameter varying spatially throughout the sample such that $\langle c_{\mathbf{k}\uparrow} c_{-\mathbf{k}\downarrow}\rangle = 0$, while the amplitude remains finite,

$$\sqrt{\left\langle \left| c_{\mathbf{k}\uparrow} c_{-\mathbf{k}\downarrow} \right|^2 \right\rangle} = |\Delta(\mathbf{k})| \neq 0$$

The first moment of the superconducting order parameter vanishes but the second moment persists.

Experimentally, phase fluctuating superconductivity above T_C in these materials has been detected by many probes. Terahertz conductivity measurements [96] find a phase correlation time consistent with the motion of vortices generated by thermal phase unlocking. The Nearnst effect, a measurement of the electric field generated by application of a thermal gradient in a magnetic field, is also consistent with diffusion of thermally excited vortices[97]. Torque magnetometry detects a diamagnetic susceptibility that increases with magnetic field, which implies the superconducting fluctuations are from the phase component [98]. In contrast, the amplitude fluctuations of BCS superconductors above T_C exhibit diamagnetism that decreases with applied field[99]. A Josephson like signal is found in superconducting-normal-pseudogap tunnel junctions as a direct consequence of fluctuating pairs[100]. Finally, microwave measurements of the critical exponent of the superfluid density near T_C are consistent with the 3DXY universality class of thermal phase unlocking transitions[101]. The region in the phase diagram where the phase fluctuation (ϕ-fl) phenomena occur are displayed in Fig. 5.1. Since this is not an ordered thermodynamic phase and because these measurements couple to the fluctuations differently, the upper bound for this region is not well defined but it is below the pseudogap crossover.

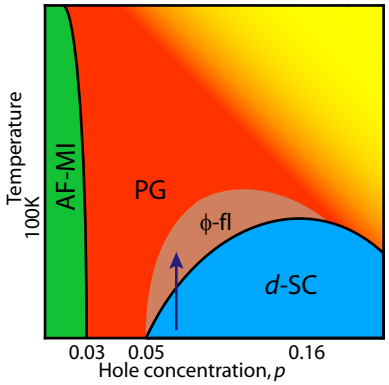

Figure 5.1: Phase diagram trajectory probed by QPI in this chapter

All of the above measurements are integrated over the microscopic quantum numbers of the superconducting electronic state. The $d_{x^2-y^2}$ complex order parameter in the cuprates has quantum number dependence so that these probes cannot observe the detailed behavior of the fluctuating superconductivity. To address this issue, the quasiparticle interference was measured at six different temperatures from $T \ll T_C$ through T_C to 1.5 T_C on a single crystal of underdoped $Bi_2Sr_2Ca_{0.8}Dy_{0.2}Cu_2O_{8+\delta}$. The crystal was chosen to be strongly underdoped with a T_C of 37+/-3K so that the thermal broadening implied by Eq. 1.7 would not obscure any dispersing QPI patterns. The dark blue line in Fig. 5.1 marks the phase diagram trajectory probed by these experiments.

5.2 Observed Modulation Patterns

Fig. 5.2 shows the conductance ratio modulations $Z(\mathbf{r}, V)$ measured at the temperatures 4.5K $\ll$ T_C, 37K $=$ T_C, and 55K $=$ 1.5T_C while Fig. 5.5 shows their Fourier transforms $Z(\mathbf{q}, V)$. $Z(\mathbf{q}, V)$ for all temperatures is in Fig. 2.9, and the topography of Fig. 5.4a demonstrates the spatial quality of the tunnel junction achieved above T_C. The same set of octet QPI wavevectors is visible

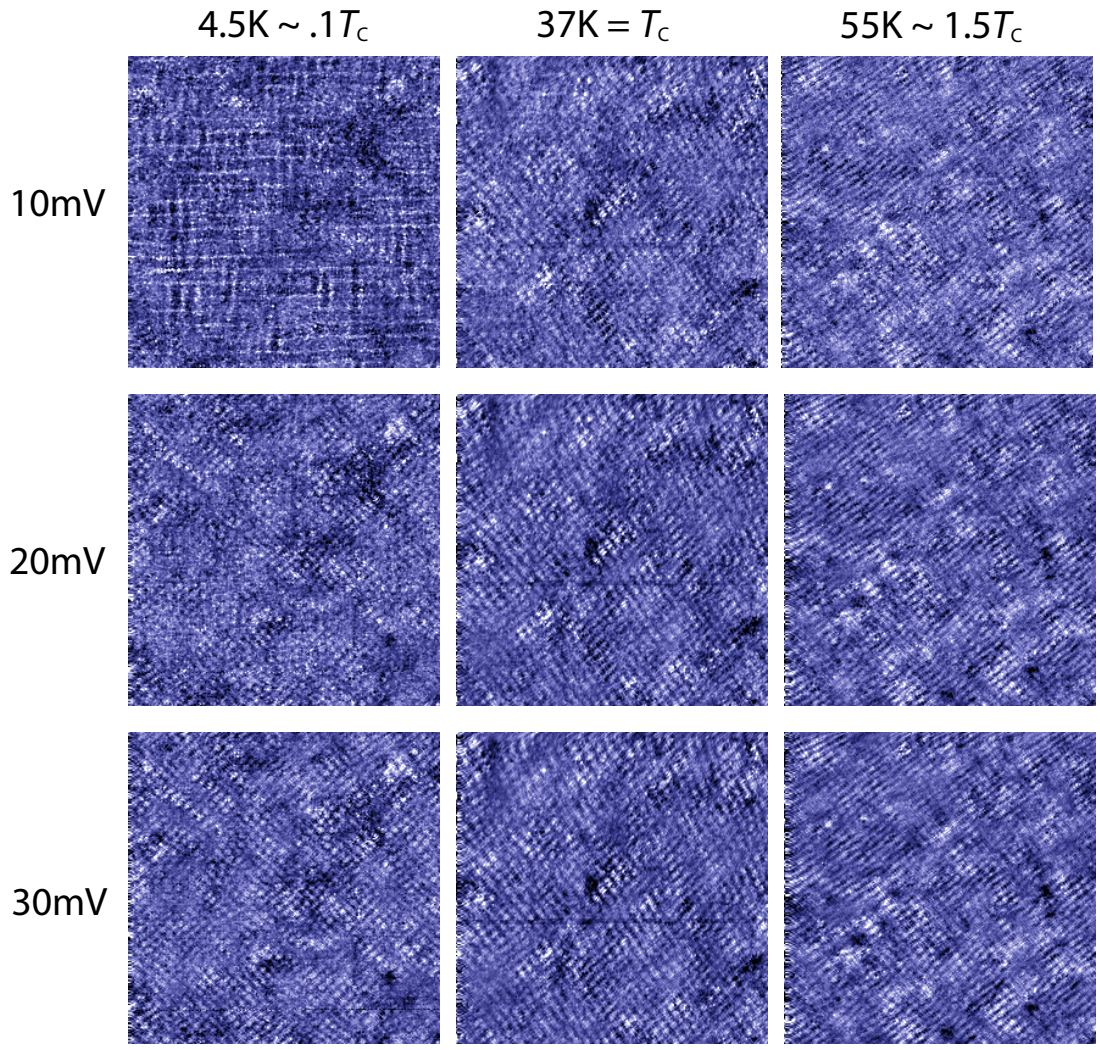

Figure 5.2: 50nm $\times$ 50nm $Z(\mathbf{r}, V)$ at 3 temperatures

in $Z(\mathbf{q}, V)$ at all temperatures, even above the bulk superconducting transition. Fig. 5.3 shows the evolution of the dispersion of the high symmetry $\mathbf{q}$-vectors $\mathbf{q_1}$, $\mathbf{q_5}$, and $\mathbf{q}_7$ with temperature from the data in Figs. 2.5 and 2.6. This smooth evolution strongly indicates that the particle-hole symmetric octet phenomenology remains valid at all temperatures observed. The octet model of QPI wavevector dispersion is controlled by the dispersion of $|\Delta(\mathbf{k})|$ (See Sec. 1.4 and ref. [41]) meaning that $|\Delta(\mathbf{k})|$ remains finite at all temperatures ob-

served – even above T_C. Conceptually, this is very easy to understand. Both the energy of the quasiparticle excitation gap $|\Delta(\mathbf{k})|$ and the tunneling measurements $Z(\mathbf{r}, V) = |u(\mathbf{r}, \omega = eV)|^2 / |v(\mathbf{r}, \omega = -eV)|^2$ are not directly dependent on the superconducting phase ϕ. Theoretical calculations for phase incoherent d-wave QPI including the phase coupling of Eq.1.14 verify this intuitive picture in detail[66]. These measurements identify the persistence of octet QPI above T_C as the spectroscopic signature of phase fluctuating d-wave superconductivity. By inverting these octet model $\mathbf{q}$-vectors we can learn about phase-fluctuating quasiparticles.

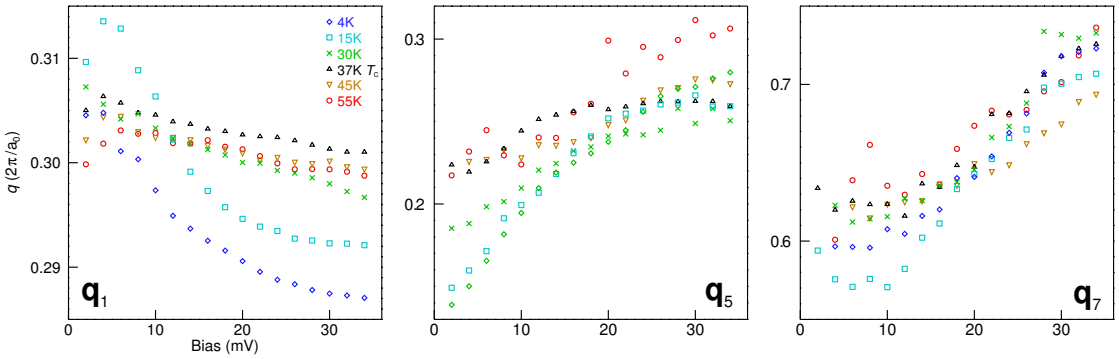

Figure 5.3: Temperature evolution of $\mathbf{q}_1$, $\mathbf{q}_5$, and $\mathbf{q}_7$ dispersion

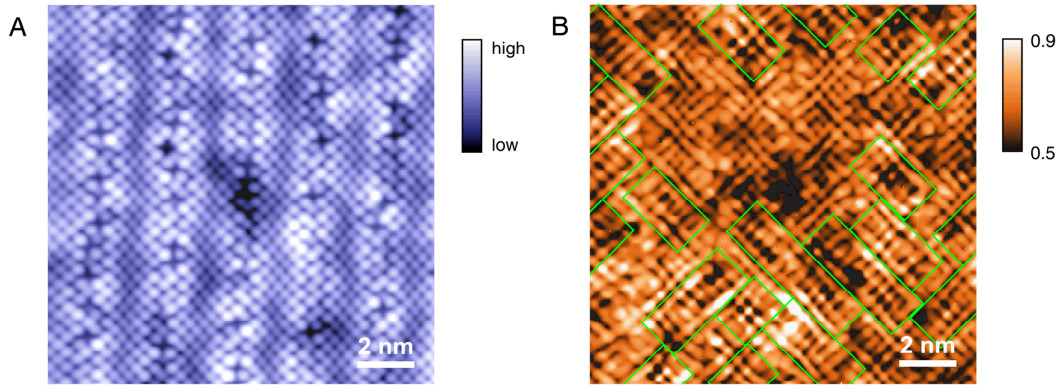

Figure 5.4: Cu-O-Cu bond centered patterns above T_C at 45K

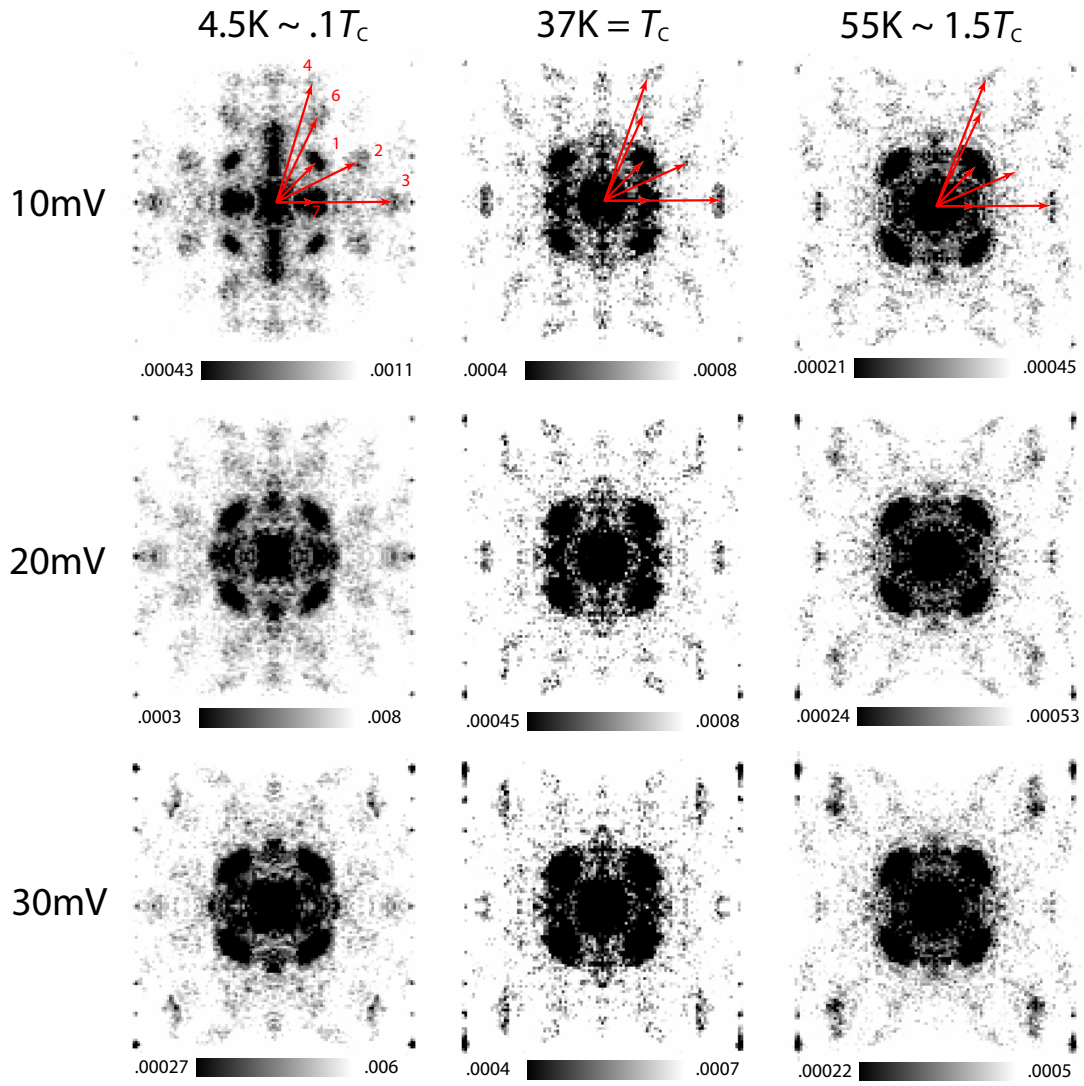

Figure 5.5: $Z(\mathbf{q}, V)$ at 3 temperatures highlighting the persistence of octet dispersion above T_C

The continuous evolution of the octet **q**-vectors in Fig. 5.6 through T_C and well into the pseudogap state makes proposals that the pseudogap originates from an alternative ordered electronic state with a static wave vector **Q**[102] both logically implausible and quantitatively inconsistent[103]. The internal consistency of the octet model, presented by the solid lines in Fig. 5.6, demonstrates that the low energy modulation below $|E| < 40mV$ can only be due to

ordered or phase fluctuating superconductivity[66]. In contrast, the higher energy non-dispersive excitations of Sec. 4.5, characteristic of the local gap $\Delta(\mathbf{r})$, persist unaltered above T_C as Fig. 5.4 demonstrates with the R-map[55] at 45K.

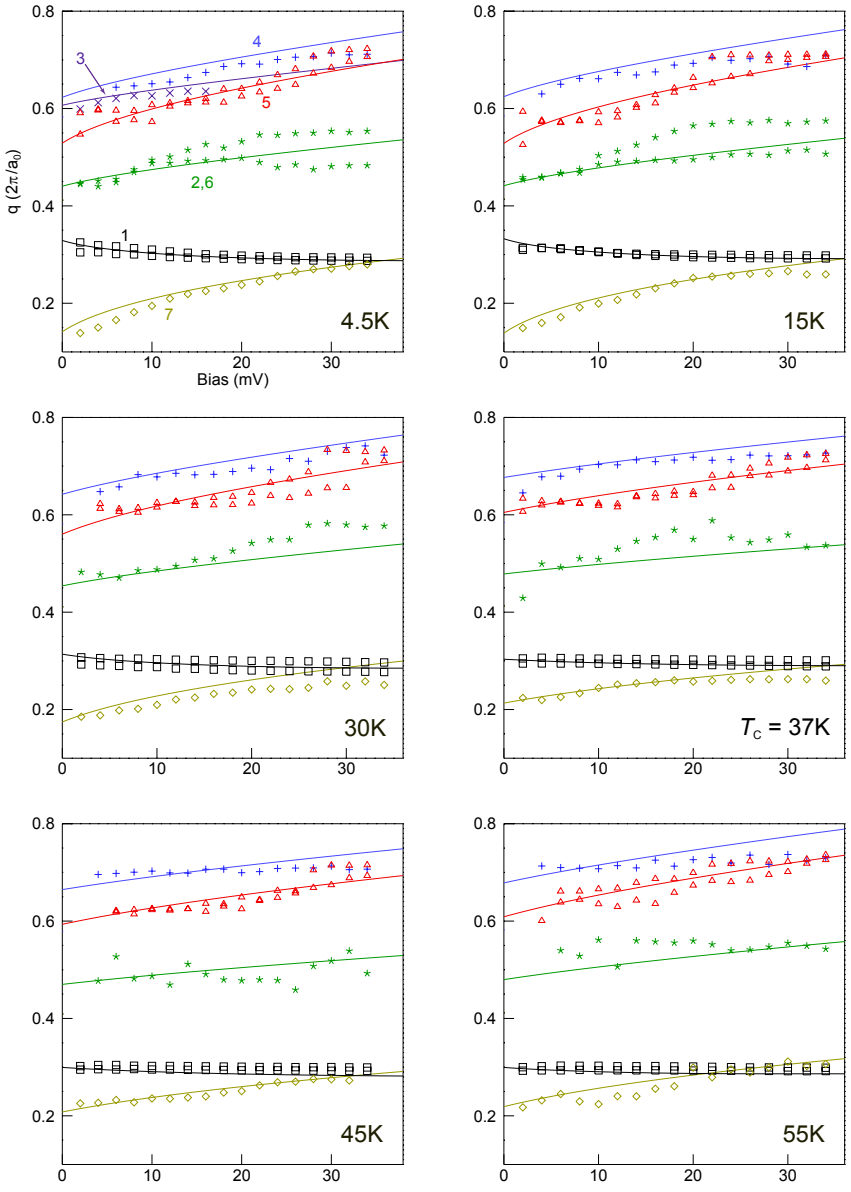

Figure 5.6: Internal consistency of the octet model at all temperatures

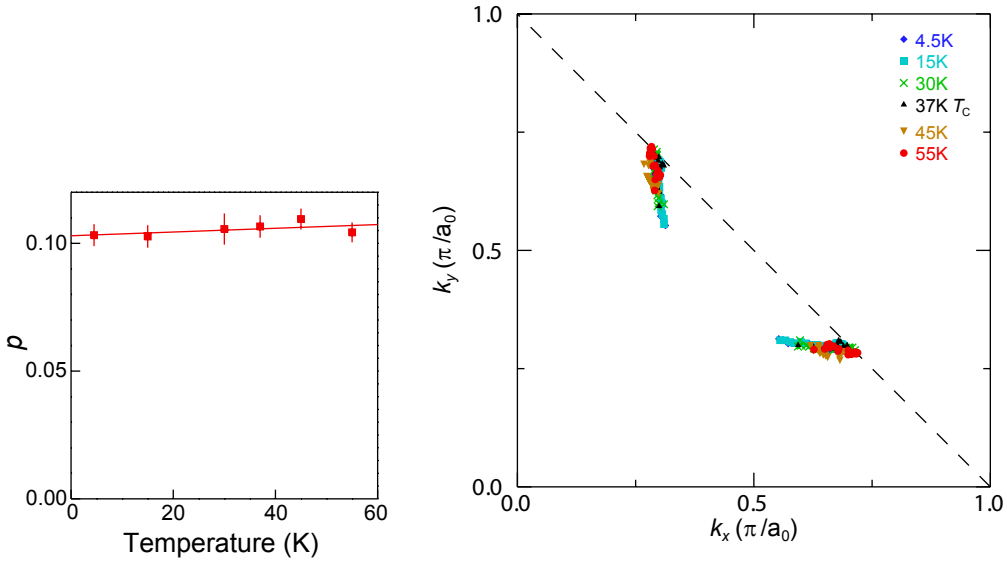

(a) Generalized Luttinger count (b) Observed **k**-space scattering loci over plot

Figure 5.7: Temperature independence of generalized Luttinger hole density

5.3 Fermi Arc Contour

In BCS superconductors, the locus of **k**-space points with minimum excitation gap changes negligibly with temperature. This is because the locus is the normal state Fermi surface which has a temperature scale, the Fermi temperature, that is factor of ~10^4 larger than T_C[81, 14]. The normal state of the cuprates is not a Fermi liquid, but the observation by ARPES of normal state Fermi arc phenomena[59, 39, 40, 91] verify that this is true for the cuprates as well. Then the octet QPI Fermi arc contour should change little with temperature. The evolution of the octet Fermi arc with temperature is displayed in Fig. 5.8. At all temperatures the quasiparticle dispersion continues to terminate just before reaching the line connecting the $(0, \pi/a_0)$, $(\pi/a_0, 0)$ Brillouin zone points, plotted by the dashed line. The fitted arcs in Fig. 5.8 indeed appear to change little with temperature. Fig. 5.7a plots the temperature dependence of the generalized Luttinger count from Ch. 4.1, demonstrating that this carrier count is

changing little with temperature. The straight line fit indicated in Fig. 5.7a yields the slope $7.3 \pm 9.9 \times 10^{-5}$ holes/$(CuO_2 \cdot \text{Kelvin})$ so that the change with temperature is consistent zero within octet statistics. The zero-temperature hole density from the fit is $.103 \pm 0.004$ holes/CuO_2. Tab. 5.1 has the full parameters for the linear least squares fit. In Fig. 5.7b the **k**-space loci generating the observed scattering patterns at each temperature are plotted simultaneously. Since the bias range (quasiparticle energy range) of observation is the same at all temperatures, this indicates that the quasiparticle gap is pulling back away from the nodal line (See Fig. 1.6a) as the temperature rises.

Table 5.1: Fig. 5.7a data fit to $p = p_0 + bT$

p_0 holes/CuO_2	b holes/$(CuO_2 \cdot \text{Kelvin})$	a, b correlation coefficient	χ^2
$.103 \pm 0.004$	$7.3 \pm 9.9 \times 10^{-5}$	-0.872	1.25

5.4 The Quasiparticle Gap and Gapless Excitations

Having failed to detect a statistically significant change in the Fermi arc contour with temperature, any detected change in the momentum space structure supporting QPI must come from $|\Delta(\mathbf{k})|$. Fig. 5.9 plots the octet $|\Delta(\theta_{\mathbf{k}})|$ structure at each temperature simultaneously, and in Fig. 5.13 they presented separately. The solid lines are the fit to Eq. 3.2. Figs. 5.7b, and 5.13 hint that the gap structure is pulling back away from the node as the temperature increases, leaving behind a region of gapless excitations that is increasing in length. This length can be estimated by extrapolation of the Eq. 3.2 fit to zero bias, producing Fig. 5.11a. The octet error estimates in Fig. 5.11a are not good enough for conclusive determination of the temperature evolution of the gapless length. This difficulty has two sources. In Fig. 5.9, there is significant overlap of the octet error esti-

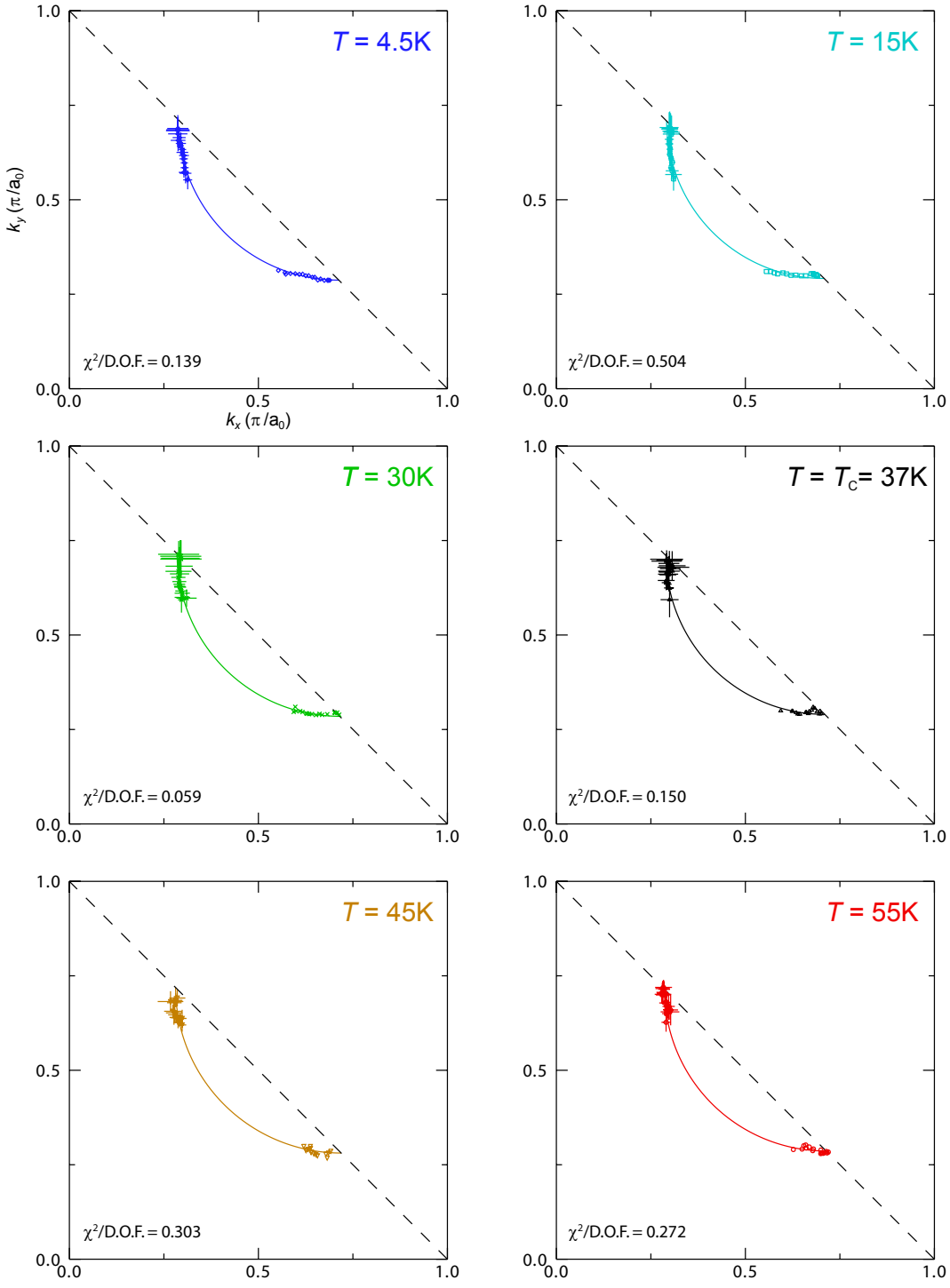

Figure 5.8: Temperature evolution of the Fermi surface

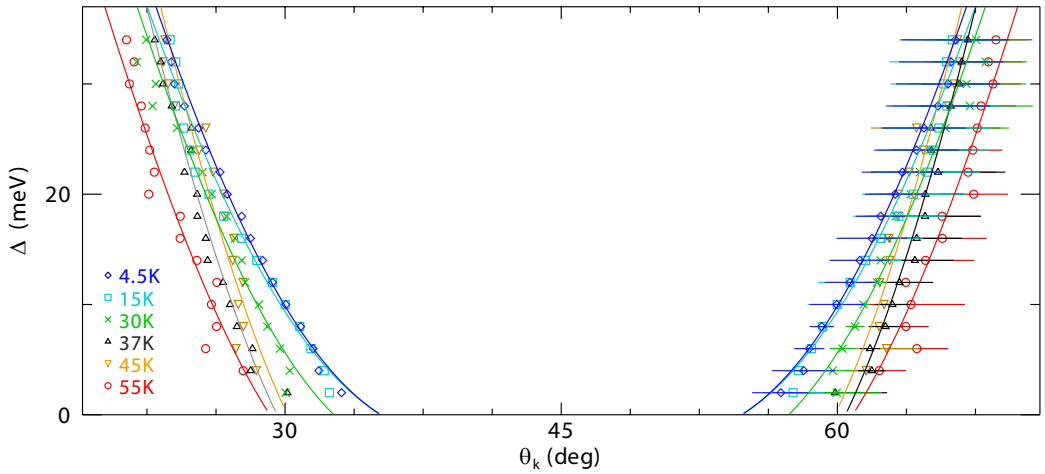

Figure 5.9: Simultaneous plot of $|\Delta(\theta_{\mathbf{k}})|$

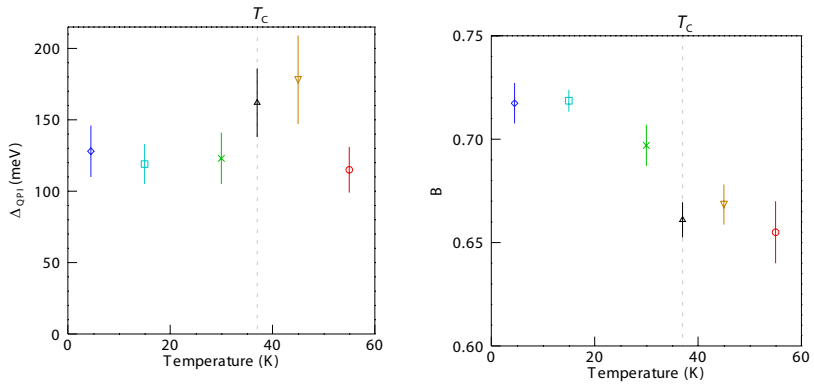

(a) Δ_{QPI} (b) B

Figure 5.10: Temperature dependence of parameters from fits to Eq. 3.2

mates of $\theta_{\mathbf{k}}$ for the different temperatures. Secondly, the model values of Δ_{QPI} are much larger than the largest quasiparticle energy measured, indicating that the measured data does not adequately constrain the parameters for Eq. 3.2. Fig. 5.10 plots the temperature dependence of Δ_{QPI} and B.

To address the inadequacy of Eq. 3.2, the more constrained function of a straight line is used to extrapolate $|\Delta(\theta_{\mathbf{k}})|$ to zero bias. This enables an extrapolation based on one fitting parameter, the intercept of the line, rather than two, Δ_{QPI} and B. Straight line fits to the data for $|\Delta(\theta_{\mathbf{k}})| \leq 14meV$ give the estimate

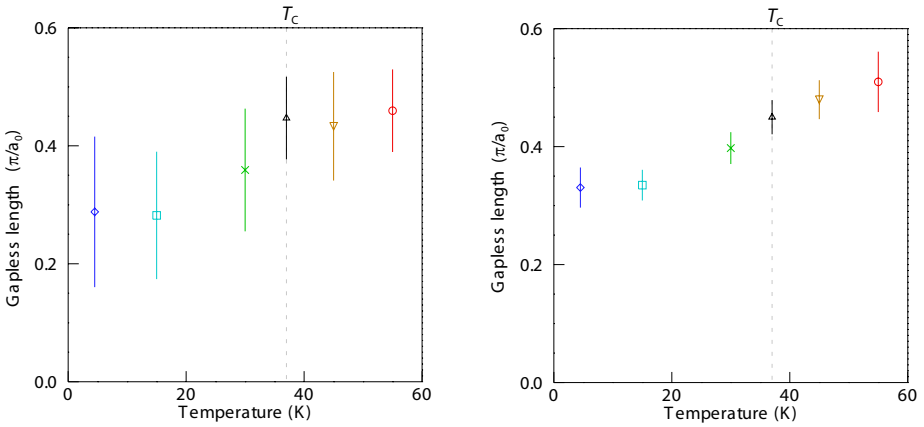

(a) Extrapolated from fits to Eq. 3.2

(b) Extrapolated from the linear fits in Fig. 5.14

Figure 5.11: Length of gapless excitations

for temperature evolution of the length of gapless excitation in Fig. 5.11b. The fits are presented in Fig. 5.14. Though in terms of the χ^2 metric it is dubious to claim that straight lines are better than Eq. 3.2, their lack of curvature leaves less freedom in the model parameters and gives the more acceptable octet error bars in Fig. 5.11b. So although there is systematic error in the absolute length associated with the choice of model for extrapolation, the size of the error bars gives good confidence that the relative length of gapless excitations is increasing monotonically with temperature. As an independent measure, the spatial average of the zero bias conductance in Fig. 5.12 is consistent with this QPI gap length.

To address the issue of overlapping $\theta_{\mathbf{k}}$ octet error estimates, note that in every fit to the inverted $\mathbf{k}$-space locus χ^2 is absurdly low for the number of degrees of freedom. This indicates that the octet error estimates are much larger than one standard deviation of the true sample mean and that the resulting errors on the fit parameters are a conservative overestimate. Estimation of the growth of the length of gapless excitations is at the very edge of what the analysis method-

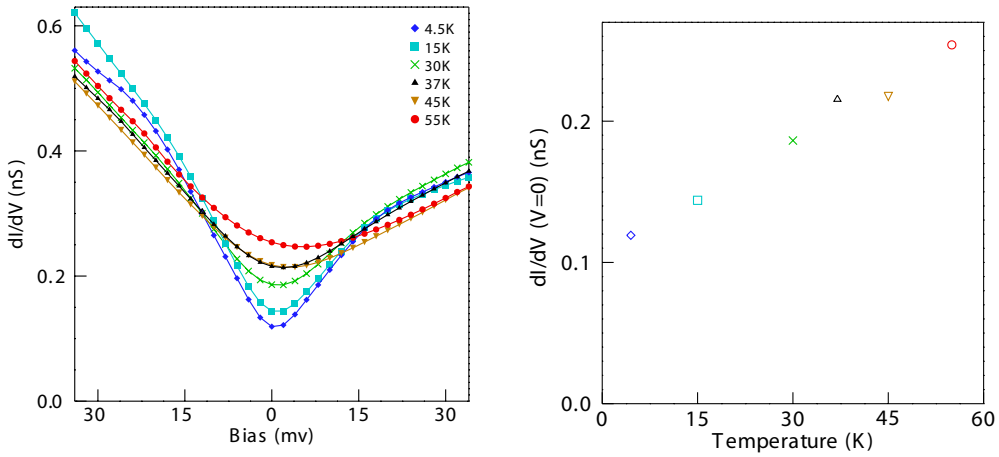

(a) Full spectra

(b) Zero bias conductance

Figure 5.12: Temperature Dependence of Average Conductance

ology presented in Ch. 3 can accurately produce. Higher accuracy than this requires more sophisticated techniques to accurately estimate the true standard deviation of the mean.

5.5 q-vector Peak Amplitude

The octet model analysis of the temperature evolution of QPI presented above has not revealed any evidence of the bulk superconducting transition. However, as Fig. 5.15a-c shows, the peak amplitudes of **q**-vectors spanning regions of **k**-space with opposite order parameter sign drop precipitously with increasing temperature, falling by a factor of 30 for $\mathbf{q}_7$. In contrast, in Fig. 5.15d-f the amplitudes of the **q**-vectors spanning regions of the same order parameter sign maintain an appreciable signal through T_C and do not exhibit monotonic behavior. (See Fig. 1.6a and Sec. 1.4) Its appealing to interpret the scattering processes illustrated in Fig. 5.15d-f as due to order parameter inhomogeneities created from the phase fluctuations. However, the detailed microscopic theory of order

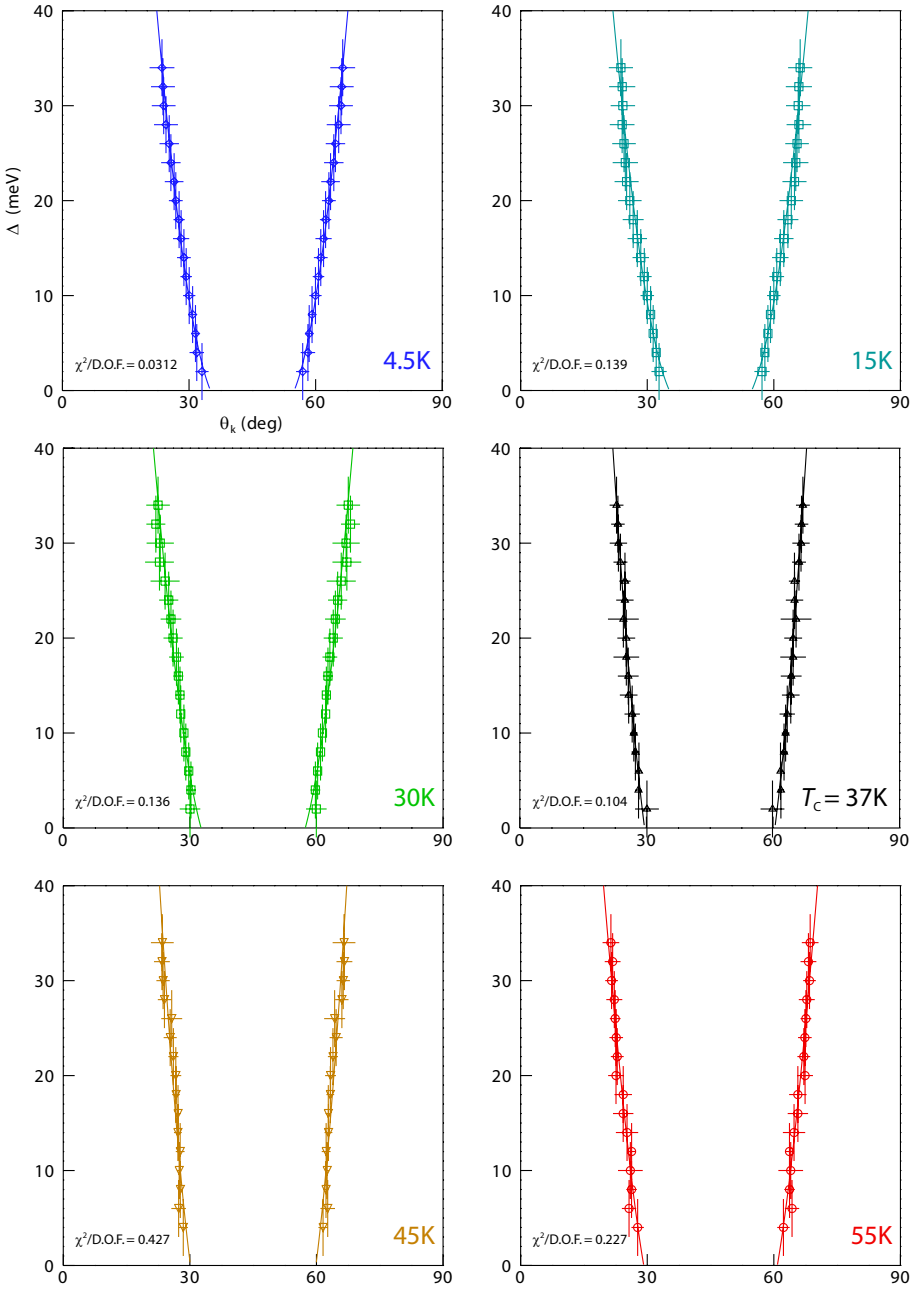

Figure 5.13: Temperature evolution of $|\Delta(\theta_{\mathbf{k}})|$ with fits to Eq. 3.2

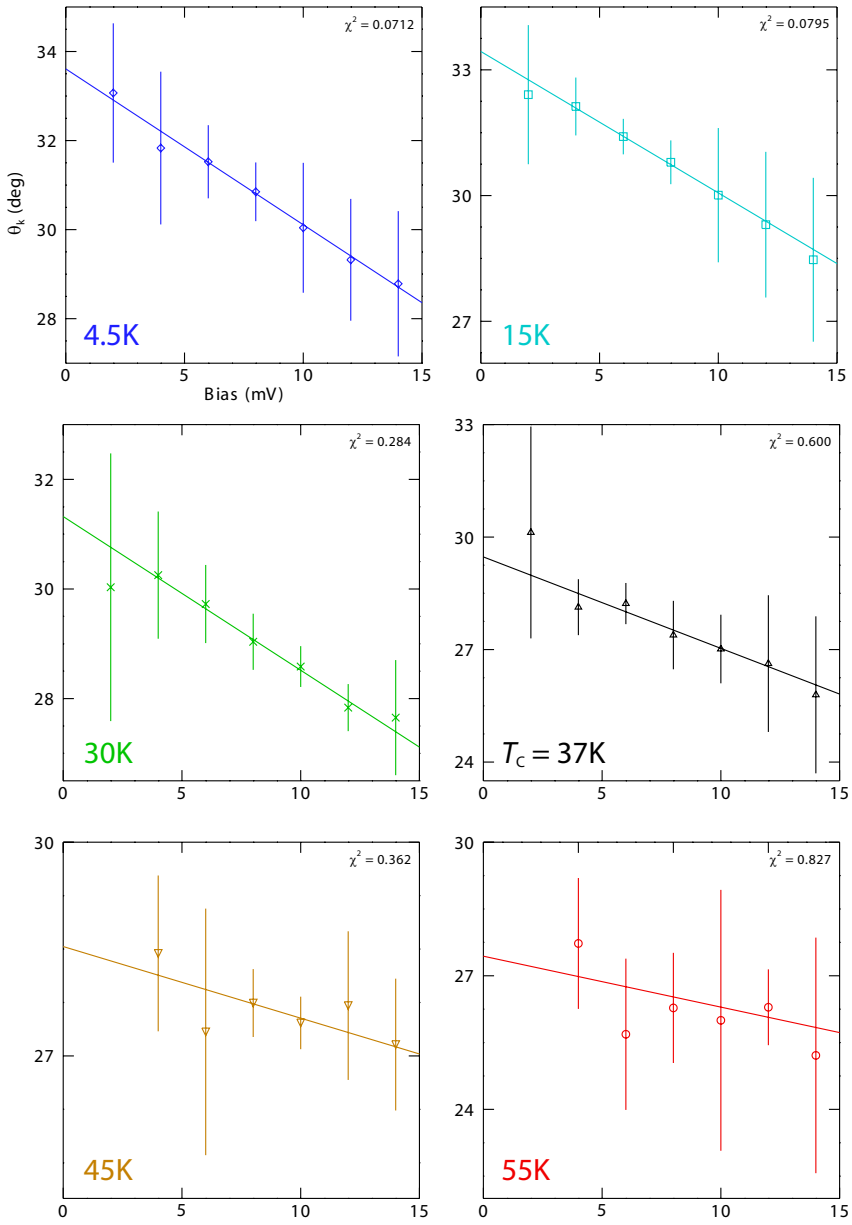

Figure 5.14: Linear fits for extrapolation of gapless excitation length

parameter scattering does not account for the phase of the order parameter and focuses instead on amplitude inhomogeneities. Similarly, Fig. 5.15a-c could be due to depletion of the superfluid density which reduces the screening response to impurities and defects. But this also has not been considered in detail. It is noteworthy that in several calculations of phase-fluctuating *d*-wave superconductivity above T_C the simple pole in the single particle Green's function becomes a factional power branch cut singularity[66, 104, 105].

A previous STM experiment pioneering spatially resolved studies above T_C in the psuedogap state had a different conclusion[106]. Fig. 5.15 allows reconciliation between the previous and present experiments. By comparing Fig S2 of Ref. [106] (the source of the Fourier analysis in the main text) with Fig. 5.2 it appears that the signal-to-noise ratio in the present experiment is higher than in the previous work. In the previous experiment, the lower signal-to-noise ratio prevented the observation of all scattering vectors except for $\mathbf{q_1}$, which according to the present analysis of Fig. 5.3, has the least dispersion.

5.6 Summary

This chapter has presented the following experimentally determined characteristics for the interference modulations of the low energy excitations in the underdoped cuprate pseudogap regime:

1. The set of seven scattering wave vectors $\mathbf{q}_i$ of the superconducting octet model persist above T_C and evolve continuously from the superconducting state, Figs. 5.5, 5.3, and 5.6.

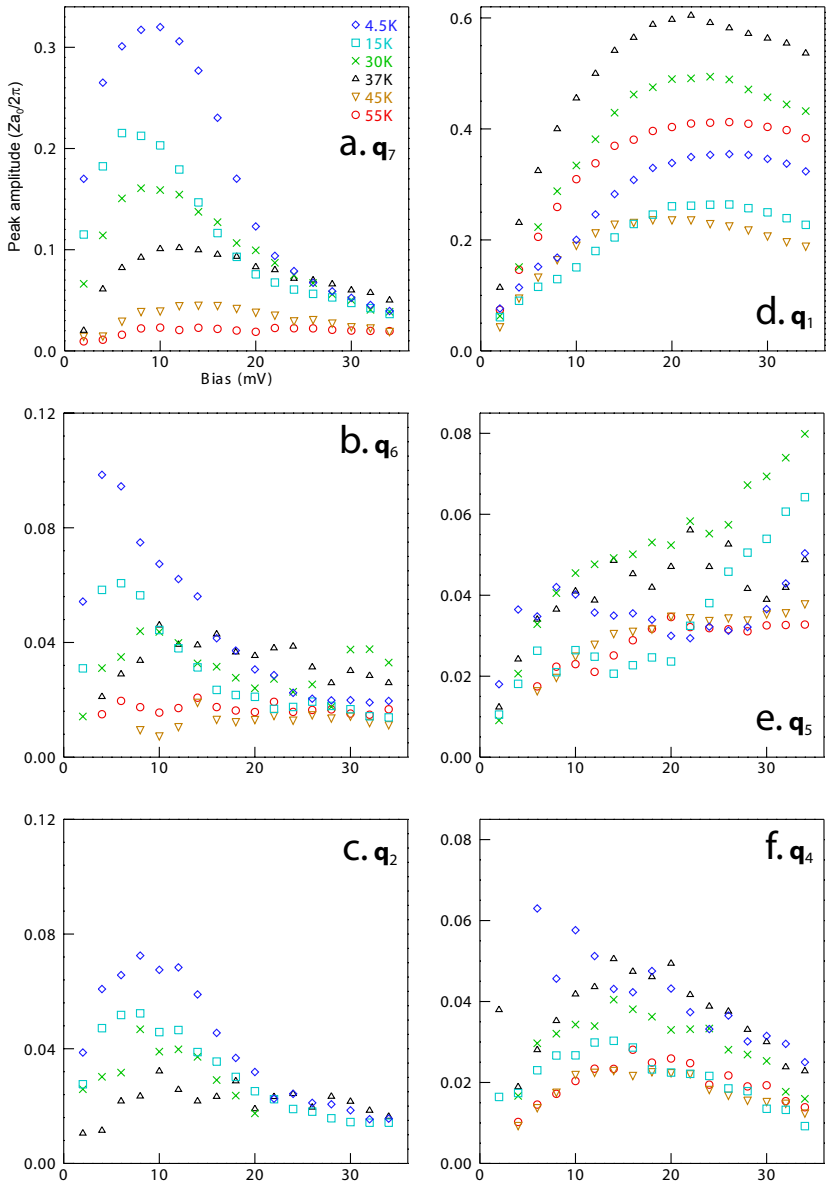

Figure 5.15: Temperature evolution **q**-vector peak amplitude

2. All the $\mathbf{q}_i$ remain dispersive in a manner internally consistent with the octet model representation of momentum space, Fig. 5.6 (solid lines).

3. Since it is modulations in the conductance ratio $Z(\mathbf{r}, V)$ (Sec. 1.5) that are analyzed with the octet QPI model , the $\mathbf{q}_i$ retain their particle-hole symmetry above T_C.

4. The modulations occur in the same energy range and are generated from the same $\mathbf{k}$-space contour at all temperatures, Figs 5.7a and 5.8.

5. The precise locations on the contour that generate the scattering change with temperature as the excitation gap $|\Delta(\mathbf{k})|$ moves back from the nodes, leaving a growing arc of gapless excitations, Figs. 5.7b, 5.11b, and 5.14. It the small lines with $|\Delta(\mathbf{k})| > 0$ in front of the $(0, \pi/a_0)$, $(\pi/a_0, 0)$ line that are the momentum space locations of the states responsible for the phase fluctuation signals in the experiments of Refs. [96, 97, 98, 101].

6. The peak amplitudes of $\mathbf{q}_i$ spanning regions of $\mathbf{k}$-space with opposite order parameter sign diminish greatly, while $\mathbf{q}$-vectors spanning regions of the same order parameter sign maintain an appreciable signal through T_C, Fig. 5.15.

The scattering amplitudes in the underdoped cuprates exhibit the same behavior as the superconducting state is weakened by increasing temperature (Fig. 5.15), falling doping (Fig. 4.9), or increasing magnetic field (Ref. [47]). Since transport and thermodynamic measurements have identified T_C as a phase unlocking transition, a reasonable hypothesis is that phase fluctuations are the mechanism destroying superconductivity on the underdoped side. However, for the cases of falling doping and magnetic field the fluctuations would have to be quantum in nature[95] and not thermal[94]. This would explain why the vor-

tex core in a magnetic field is not consistent with a *d*-wave BCS amplitude suppressed structure[107, 108] and immediately leads to the prediction that such structure will be recovered for the very overdoped cuprates. Finally, the hypothesis of a fractional power Green's function could in the future be tested by extracting the power from analysis[66] of normal state QPI data and comparing it to that already obtained from normal state ARPES[105] studies.

CHAPTER 6

CONCLUDING REMARKS

"One of my favorite times in the academic year occurs in early spring when I give my class of extremely bright graduate students, who have mastered quantum mechanics but are otherwise unsuspecting and innocent, a take-home exam in which they are asked to deduce superfluidity from first principles. There is no doubt a special place in hell being reserved for me at this very moment for this mean trick, for the task is impossible." Robert Laughlin[109]

6.1 Impact on the Broader Context of Cuprate Physics

Interpreting the momentum space structure implied by quasiparticle interference in terms of a generalized Luttinger theorem (Ch. 4) provides a framework for understanding the experimental data on underdoped cuprates. The two-component behavior seen in various measurements arises from the two momentum surfaces of the theorem: the familiar surface of Green's function poles as well as the surface of Green's zeroes created by strong correlations. The superconducting component comes from poles while the pseudogap component comes from the zeroes. The component that appears at the superconducting transition T_C is from the poles while the component that evolves continuously through T_C is from the zeroes.

- In the two component analysis of the carrier count from the Hall coefficient, the temperature independent term originates from the poles while the thermally activated term comes from the zeroes. This analysis also

shows that the extracted activation energy agrees well with the pseudogap energy measured by ARPES[110].

- In optical conductivity measurements, the Drude peak comes from the poles while the mid-IR band comes from the zeroes[79, 111]. The peak energy of this band is consistent with twice the energy of the ARPES pseudogap.
- In electronic specific heat measurements, the jump at T_C and its decrease with decreasing doping comes from the poles while the drop in the normal state specific heat with decreasing temperature is due to the zeroes[112].
- The linear doping dependence of the superfluid density[93] is due to the poles, which exhibit identical doping behavior in Fig. 4.1b.
- In Raman measurements, the B_{2g} symmetry component from the nodal region of momentum space comes from the poles, while the B_{1g} component from the antinodes is due to the zeroes[75].
- In STM, the homogeneous low energy spectrum comes from the poles and the higher energy heterogeneous gap structure comes from the zeroes. (Ch. 4.2.1) The low energy spectrum has strong changes through T_C[113, 114] while the heterogeneous gap disappears at the much higher temperature T^*[60, 89].
- In ARPES, the nodal region exhibiting quasiparticle peaks below T_C and the Fermi arc above is from the poles, while the peak-less antinodal region that remains gapped above T_C is from the zeroes[39, 40, 91, 82, 74, 59, 83, 115, 116].

This simple picture of poles and zeroes is most accurate in the very underdoped regime. In reality, the detailed picture across the phase diagram is more

complicated. All of these properties evolve continuously into the overdoped region where non-interacting Fermi liquid behavior without a zero surface is recovered[117, 118, 119]. This cannot only be due to the Fermi surface topology change in overdoped $Bi_2Sr_2CaCu_2O_{8+\delta}$ where the anti-bonding pole surface moves entirely in front of the hypothesized zero surface along the $(0, \pi/a_0)$, $(\pi/a_0, 0)$ line[120]. The temperature independent component of the Hall carrier count deviates from p near $p = 1/8$[110], well below the topology change. The inhomogeneous STM gap distribution suggests that a linear combination of momentum space states is required to describe the eigenstates as translational invariance has been lost. Near optimal doping this hypothesized linear combination would include momentum space states both with and without the surface of zeroes. Accordingly, ARPES does not observe a sharp division in momentum space between the pseudogap and the superconducting quasiparticle peaks but rather a small region where the two overlap[121]. Therefore the ARPES normal state Fermi arc and QPI Fermi arc should not coincide exactly but the QPI Fermi arc should be slightly longer.

It is this region of overlap between the pseudogap and quasiparticle peaks in ARPES data that should coincide with the region where the QPI- determined $|\Delta(\mathbf{k})|$ remains finite above T_C. This small region is the source of the observed phase fluctuation behavior. At the same time, this picture of poles and zeroes is not consistent with the simplest idea of the pseudogap as a phase- fluctuating pairing precursor to a superconducting state that condenses at T_C. The antinodal states, with Green's function zeroes, can never contribute to the superconducting condensate. Despite this, in the underdoped regime there are ARPES measurements of the psuedogap consistent with Cooper pairing above T_C[122, 123] and the observation by STM of a particle-hole symmetric pseudogap[60]

consistent with a strongly scattered d-wave superconducting gap[86]. If the underdoped psuedogap is due to phase fluctuating pairs then the pairs are phase fluctuating down to $T = 0$ and never condense. The observation of gap continuity below T_C[59, 91, 83] and Fig. 4.6 as well as the STM observation[86, 89, 113] of continuous evolution of the pseudogap into the superconducting gap on a large area Fermi surface suggests an intimate relation between the superconducting gap and the pseudogap.

6.2 Comparison with Theory

The following are key spectroscopic features that any theory of the high temperature superconductivity in the underdoped cuprates should address

1. Momentum space anisotropy with sharp coherent quasiparticles in the region of the d-wave order parameter node and broad peak-less incoherent features near the antinode.
2. The nodal states are the low energy d-wave superconducting excitations and they exhibit a homogeneous spectrum well described in momentum space. The antinodal states are the higher energy excitations of the pseudogap with a characteristic energy scale rising as p decreases toward the Mott insulating state. As demonstrated in Sec. 4.5 these states are better described in real space.
3. This anisotropy is generated from strong correlations such that the nodal states are described by surfaces of poles in the single particle Green's function while the antinodal states are described by surfaces of zeroes.

4. The boundary in momentum space between the poles and zeroes are demarcated by the line connecting $(0, \pi/a_0)$, $(\pi/a_0, 0)$ in the Brillouin zone.
5. The real space configuration of antinodal excitations have contrast on the O atoms and locally break C_4 rotational symmetry[55].
6. The thermal phase transition out of the superconducting state is due to phase fluctuations

Much of these feature are captured by Resonating Valence Bond (RVB) theory of high temperature superconductivity, an early proposal by Phil Anderson[124] for a strongly correlated, all electronic mechanism for pairing. In this framework, the relevant Hamiltonian for the CO_2 plane is the Hubbard model in the strongly correlated limit

$$\mathcal{H} = \sum_{\langle i,j\rangle,\sigma} t_{ij} c^{\dagger}_{i\sigma} c_{j\sigma} + \sum_{i,\sigma} U n_{i\sigma} n_{i\bar{\sigma}} \tag{6.1}$$

t_{ij} is the amplitude for hopping from lattice site j to i, $\langle i, j\rangle$ denotes sum over nearest neighbors, and U is the Coulomb repulsion between electrons occupying the same lattice site. In the strongly correlated limit, U is much larger than the bandwidth of the $U = 0$ system, strongly suppressing double occupancy of a lattice site and creating the Mott insulating state at half filling, $p = 0$. The remaining Cu spin-1/2 degrees of freedom are subject to an antiferromagnetic superexchange $J = 4t^2/U$. This is minimized by forming delocalized singlet bonds between pairs of spins, creating a spin liquid. Anderson proposed that a good approximation to this state is formed by starting with a BCS singlet wavefunction, fixing the pair number, and projecting out doubly occupied states. Removing electrons by doping the system with mobile holes

allows the RVB singlet pair number to vary and the material becomes superconducting. Thus in the RVB model, phase fluctuations are a consequence of the localization tendency because Cooper pair number and phase are incompatible observables[14]. Mean-field slave-boson studies of Eq. 6.1 in the limit $U \rightarrow \infty$[125], studies of projected wavefunction by the Gutzwiller method (reviewed in Ref. [126]) implemented by variational Monte Carlo[127, 128], and cellular dynamical mean field theories[129, 130] find properties 1-3 and 6.

While semi-quantitatively accurate and providing a good conceptual framework, RVB theory misses some key details. Foremost is the experimental observation of a static antiferromagnetic ground state and not a spin liquid at $p = 0$. In this case the antiferromagentic Brillouin zone boundary is the $(0, \pi/a_0)$, $(\pi/a_0, 0)$ line in momentum space. In the simplest hypothesis, property 4 is a connection to the physics of the antiferromagnet at $p = 0$. Experimentally, X-ray absorption studies find that the doped holes are introduced on O $2p$ orbitals[131, 132]. Consideration of the oxygen orbitals leads to a description of the cuprates as charge-transfer[133] insulators rather than Mott insulators. Superconductivity is produced from the spin of doped O holes interacting with the spin of the Cu^{2+}[134]. As in RVB, this is a strongly correlated and local superexhange mechanism. The destruction of the $p = 0$ antiferromagnet by doping could lead to an electronic liquid crystal[135], stripes[136, 137], or a valence bond solid (VBS)[138, 139] all of which give property 5. (These do not exhaust the possibilities) Stripes and VBS are distinguished by the ground state spin configuration on the Cu atoms. Stripes are antiferromagentic with different ordering vectors than at the state $p = 0$, while VBS has local singlet bonds centered on the O atoms.

Studies of one loop renormalization group flows of the two dimensional Hubbard model produce property 4[140, 141]. Starting in the weak coupling regime, strongly anisotropic scattering in the particle-particle and particle-hole channels send the flows to strong coupling. This scattering drives both d-wave pairing and antiferromagnetic fluctuations. It is strongest a for momentum transfer of (π, π) between states near the antinodes, forming an insulating spin liquid from these states and truncating the Fermi surface at its intersection with the $(0, \pi/a_0)$, $(\pi/a_0, 0)$ line. This theory has been used to describe[142] the anisotropic scattering in angle-dependent magnetoresistance measurements [143] that produce the unusual T-linear scattering rate in the normal state[144], and appears also to describe the q-vector scattering amplitudes of Fig. 4.9 well. In this context, these amplitudes are inconsistent with charge density wave formation[90, 115, 123] because the amplitudes associated with charge scattering follow the angular decay of the ARPES superconducting quasiparticle peak[121] rather than increasing near the proposed nesting segments. While the renormalization group calculations are strictly only valid in the overdoped regime, the strong coupling fixed point was identified with that of the spin liquid in doped two-leg ladders describing the underdoped regime. This led to a phenomenological proposal for the cuprate single particle Green's function[80, 145].

APPENDIX A

CHANGE OF BASIS IN TUNNELING SPECTRAL FUNCTION

We will begin by looking at the real-space propagator

$$\left\langle \Psi^{\dagger}\left(\mathbf{r},t\right)\Psi\left(\mathbf{r}\right)\right\rangle$$

$\Psi^{\dagger}\left(\mathbf{r},t\right)$is the quantum field operator that creates an electron at position $\mathbf{r}$ and time t. In the Heisenberg picture this is

$$\left\langle \Psi^{\dagger}\left(\mathbf{r},t\right)\Psi\left(\mathbf{r}\right)\right\rangle =\left\langle U^{\dagger}\left(t\right)\Psi^{\dagger}\left(\mathbf{r}\right)U\left(t\right)\Psi\left(\mathbf{r}\right)\right\rangle \tag{A.1}$$

$U\left(t\right)$ is the time evolution operator. In terms of the eigenstates ν of the underlying Hamiltonian, the quantum field operator can be written as

$$\Psi^{\dagger}\left(\mathbf{r}\right)=\sum_{\mu}c_{\mu}^{\dagger}\left\langle \mu|\mathbf{r}\right\rangle =\sum_{\mu}c_{\mu}^{\dagger}\psi_{\mu}^{*}\left(\mathbf{r}\right) \tag{A.2}$$

Again, $\psi_{\nu}\left(\mathbf{r}\right)$ is the wavefunction for state ν. Inserting Eq. A.2 into Eq. A.1 gives

$$\left\langle \Psi^{\dagger}\left(\mathbf{r},t\right)\Psi\left(\mathbf{r}\right)\right\rangle =\sum_{\mu\mu'}\psi_{\mu'}^{*}\left(\mathbf{r}\right)\psi_{\mu}\left(\mathbf{r}\right)\left\langle U^{\dagger}\left(t\right)c_{\mu'}^{\dagger}U\left(t\right)c_{\mu}\right\rangle$$

For $\mu'\neq\mu$, $\left\langle U^{\dagger}\left(t\right)c_{\mu'}^{\dagger}U\left(t\right)c_{\mu}\right\rangle =0$ since by assumption the state μ is eigenstate of the underlying Hamiltonian and such a state cannot transition into another eigenstate $\mu^{'}$ as time evolves. And so

$$\left\langle \Psi^{\dagger}\left(\mathbf{r},t\right)\Psi\left(\mathbf{r}\right)\right\rangle =\sum_{\mu}\left|\psi_{\mu}\left(\mathbf{r}\right)\right|^{2}\left\langle U^{\dagger}\left(t\right)c_{\mu}^{\dagger}U\left(t\right)c_{\mu}\right\rangle =\sum_{\mu}\left|\psi_{\mu}\left(\mathbf{r}\right)\right|^{2}\left\langle c_{\mu}^{\dagger}\left(t\right)c_{\mu}\right\rangle \tag{A.3}$$

Note that the spin quantum number has been ignored here.

To make the connection with tunneling, the tunnel current Eq. 1.2 can be written (see Ref.[13] Eq. 8.73 of that text)

$$\begin{aligned} I_{t} &= \int_{-\infty}^{\infty}\frac{d\omega}{2\pi\hbar}\sum_{\mu\nu}\left|T_{\mu\nu}\right|^{2}\left[\left\langle c_{\nu}\left(\omega+eV\right)c_{\nu}^{\dagger}\right\rangle_{1}\left\langle c_{\mu}^{\dagger}\left(\omega\right)c_{\mu}\right\rangle_{2}-\right.\\ &\quad\left.\left\langle c_{\nu}^{\dagger}\left(\omega+eV\right)c_{\nu}\right\rangle_{1}\left\langle c_{\mu}\left(\omega\right)c_{\mu}^{\dagger}\right\rangle_{2}\right] \end{aligned}$$

Inserting Tersoff and Hamann's tunneling matrix element $T_{\mu\nu}$ Eq. 1.6,

$$\begin{aligned} I_t &= \left|\frac{\hbar^2}{2m}4\pi\Omega_1^{-1/2}Re^{\kappa R}\right|^2 \int_{-\infty}^{\infty}\frac{d\omega}{2\pi\hbar}\sum_{\nu}\left[\left(\sum_{\mu}\left|\psi_\mu\left(\mathbf{r}_0\right)\right|^2\left\langle c_\mu\left(\omega\right)c_\mu^\dagger\right\rangle_2\right)\times\right. \\ &\left.\left\langle c_\nu^\dagger\left(\omega+eV\right)c_\nu\right\rangle - \left(\sum_{\mu}\left|\psi_\mu\left(\mathbf{r}_0\right)\right|^2\left\langle c_\mu^\dagger\left(\omega\right)c_\mu\right\rangle_2\right)\left\langle c_\nu\left(\omega+eV\right)c_\nu^\dagger\right\rangle_1\right] \end{aligned}$$

Substituting the time Fourier transform of Eq. A.3 into the parenthesis,

$$\begin{aligned} I_t &= \left|\tfrac{\hbar^2}{2m}4\pi\Omega_1^{-1/2}Re^{\kappa R}\right|^2 \int_{-\infty}^{\infty}\frac{d\omega}{2\pi\hbar}\sum_{\nu}\left[\left\langle\Psi\left(\mathbf{r}_0,\omega\right)\Psi^\dagger\left(\mathbf{r}_0\right)\right\rangle_2\left\langle c_\nu^\dagger\left(\omega+eV\right)c_\nu\right\rangle_1\right. \\ &\left. - \left\langle\Psi^\dagger\left(\mathbf{r}_0,\omega\right)\Psi\left(\mathbf{r}_0\right)\right\rangle_2\left\langle c_\nu\left(\omega+eV\right)c_\nu^\dagger\right\rangle_1\right] \end{aligned}$$

This can be re-expressed with the spectral functions as

$$\begin{aligned} I_t &= \left|\frac{\hbar^2}{2m}4\pi Re^{\kappa R}\right|^2 \int_{-\infty}^{\infty}\frac{d\omega}{\hbar}A_2\left(\mathbf{r}_0,\omega\right)\left(\sum_{\nu}\frac{1}{2\pi\Omega_1}A_1\left(\nu,\omega+eV\right)\right) \\ &\times\left[n_F\left(\omega+eV\right)-n_F\left(\omega\right)\right] \end{aligned}$$

By Eq. 1.3, the quantity in parenthesis is the density of states per unit volume of the tip, $g_1\left(\omega+eV\right)$. Finally we arrive at

$$I_t = \left|\frac{\hbar^2}{2m}4\pi Re^{\kappa R}\right|^2 \int_{-\infty}^{\infty}\frac{d\omega}{\hbar}A_2\left(\mathbf{r}_0,\omega\right)g_1\left(\omega+eV\right)\left[n_F\left(\omega+eV\right)-n_F\left(\omega\right)\right]$$

APPENDIX B

RESOLUTION OF LOCK-IN AMPLIFIER DIFFERENTIAL CONDUCTANCE

Differential conductance of tunnel junctions measured with a lock-in amplifier suffers from voltage broadening about the DC bias voltage. This is because lock-in amplifiers measure dI_t/dV by $\Delta I_t/\Delta V$ where ΔI_t is the current response of the tunnel junction to a driving AC bias modulation voltage $\Delta V = V_{AC}\cos(\omega t)$. Choosing the bias modulation drive so that $\Delta I_t/\Delta V$ accurately measures dI_t/dV the requires that the conductance vary little over the peak-to-peak drive voltage range. But because the current response diminishes with the bias modulation amplitude, an inadequate experimental signal-to-noise ratio can force measurements with an undesirably high bias modulation amplitude. Here, a quantitative description for the voltage broadening of a lock-in amplifier is developed.

By driving a tunnel junction with a bias voltage

$$V(t) = V_{DC} + V_{AC}\cos(\omega t)$$

the current response is

$$I(t) = I_{DC} + I_1\cos(\omega t) + I_2\cos(2\omega t) + \ldots$$

In general, the current will respond at all harmonics of the drive frequency in a Fourier series. The phase-sensitive lock-in amplifier is set to measure the Fourier coefficient I_1, so that a spectroscopic curve is more precisely a measurement of $I_1(V_{DC})$.

We chose the drive frequency so as to avoid any dynamic response by the junction. By assuming no dynamic response, the current will be purely resis-

tive, meaning in-phase with the drive voltage and the time dependence will be given parametrically by $I(V(t))$ where $I(V)$ is the DC relation. The Fourier coefficient is then

$$\begin{aligned} I_1 &= \frac{1}{\pi}\int_{-\pi}^{\pi} I(V(x))\cos(x)\,dx \\ V(x) &= V_{DC} + V_{AC}\cos(x) \end{aligned}$$

This suggests the substitution $u = \cos(x)$ to evaluate the integral. However because $du = -\sin(x)\,dx$ and $\sin(x) = \pm\sqrt{1-u^2}$, care must be taken to chose the proper branch cut. For $0 \leq x < \pi$, $\sin(x) > 0$ and the positive branch is taken. For $\pi \leq x < 2\pi$, $\sin < 0$ and the negative branch is taken. Carrying this out in the substitution produces

$$I_1 = -\frac{1}{\pi}\int_1^{-1} \frac{I(V(u))\,u}{\sqrt{1-u^2}}du + \frac{1}{\pi}\int_{-1}^{1} \frac{I(V(u))\,u}{\sqrt{1-u^2}}du = \frac{2}{\pi}\int_{-1}^{1} \frac{I(V(u))\,u}{\sqrt{1-u^2}}du$$

Integration by parts followed by the substitution $V' = V_{AC}u$ yields

$$I_1 = \frac{2}{\pi}\int_{-V_{AC}}^{V_{AC}} \sqrt{1-(V'/V_{AC})^2}\frac{dI_t}{dV}\left(V_{DC}+V'\right)dV'$$

This can be rewritten into the final form for the voltage/energy broadening introduced by the finite bias modulation amplitude of the lock-in amplifier

$$I_1 = \frac{2}{\pi}\int_{-V_{AC}}^{V_{AC}} \sqrt{1-(V'/V_{AC})^2}\frac{dI_t}{dV}\left(V_{DC}-V'\right)dV' \tag{B.1}$$

Which is in the form of a convolution for

$$\begin{aligned} I_1(V_{DC}) &= \int_{-\infty}^{\infty} h(V')\frac{dI_t}{dV}\left(V_{DC}-V'\right)dV' \\ h(V) &= \begin{cases} 0 & V < -V_{AC} \\ \frac{2}{\pi}\sqrt{1-(V/V_{AC})^2} & -V_{AC} \leq V \leq V_{AC} \\ 0 & V > V_{AC} \end{cases} \end{aligned}$$

The singularities in the derivatives of $h(V)$ mandates that deconvolution be approached with more sophisticated non-linear inverse theory.

APPENDIX C

CALIBRATING THE STM POSITION SENSOR

This Appendix closely follows Appendix B of Ray Simmond's Ph.D. dissertation [146] with the explicit geometry of the STM position sensor capacitance.

The coarse approach mechanism (the walker, see Refs. [26, 28]) of the Davis group's STM heads have a metallic cylinder attached to the scanner. A second, fixed metallic cylinder with a slightly larger diameter sits concentric to the scanner cylinder, forming a parallel plate capacitor. Because $d \ll r_1, r_2$ the parallel plate capacitor formula can be invoked so that

$$C_{STM} = \frac{\epsilon_0 2\pi r_1 L}{d}$$

As the scanner moves forward during coarse approach, the overlap of the two cylinders changes, which changes the capacitance. This geometry is shown in Fig. C.1. By putting this capacitor into the Wheatstone bridge circuit of Fig. C.2 we can measure the differential capacitance

$$\delta C_{STM} = \frac{\epsilon_0 2\pi r_1}{d}\delta L = C_{STM}\left(\frac{\delta L}{L}\right) \tag{C.1}$$

to yield the motion δL of the scanner in real distance units.

A Wheatstone bridge is created using two inductors and two capacitors. A ratio transformer provides ground isolation for the experiment as well as the two inductors whose values are set by an adjustable ratio α so that $L_1 = (\alpha - 1)\, L$ and $L_2 = \alpha L$. One capacitor C_{ref} is a fixed reference. The other capacitor is C_{STM}. An excitation voltage V_{in} is applied to the input of the ratio transformer, and a response voltage V_{out} is measured at the output. We use a lock-in

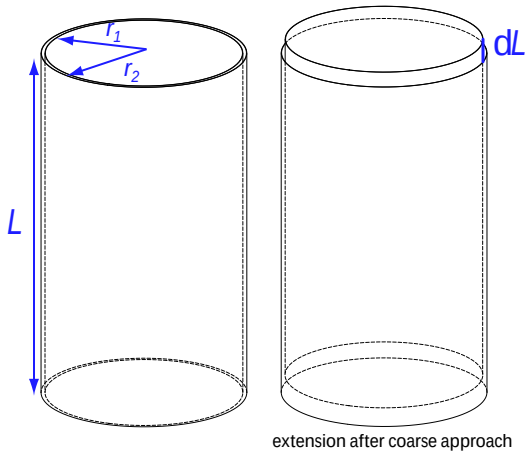

Figure C.1: Position sensor capacitance geometry

amplifier to measure V_{out} as well as provide V_{in} with its sine reference. This arrangement allows for the measurement of the very small voltage responses by using large time constants on the lock-in output filter.

Before starting coarse approach α on the ratio transformer is adjusted until V_{out} is zero. This is defines the balance point of the bridge. Here, the clever grounding in Fig. C.2 cancels the stray capacitance C_S since both ends of C_S are at the same potential. At this point

$$\frac{C^0_{STM}}{C_{ref}} = \frac{L_1}{L_2} = \frac{\alpha_0 - 1}{\alpha_0} \tag{C.2}$$

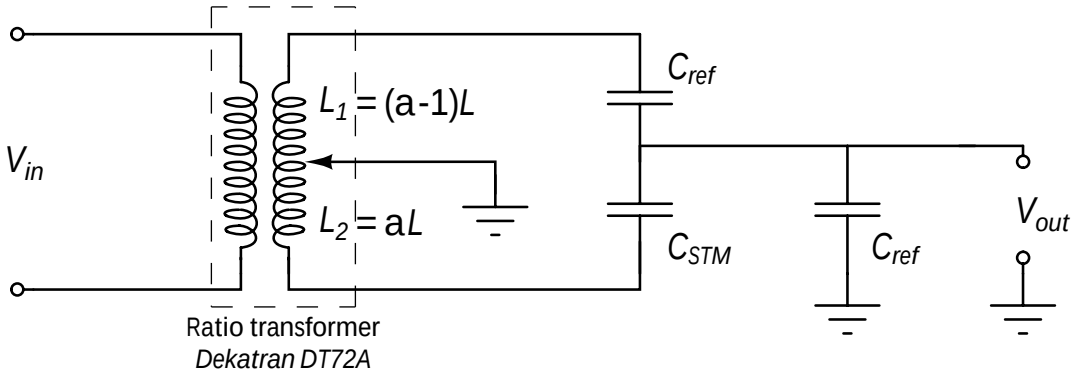

Figure C.2: Wheatstone bridge circuit of the position sensor

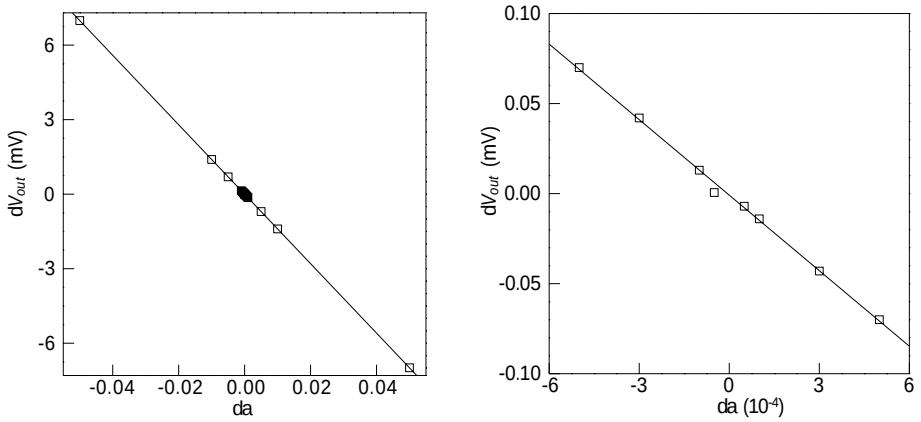

(a) Full scale response (b) Near origin

Figure C.3: Determination of the linear response coefficient λ

or

$$C^0_{STM} = \left(\frac{1}{\alpha_0} - 1\right) C_{ref} - C_S \tag{C.3}$$

Above, the values of α and C_{STM} at the balance point are identified as α_0 and C^0_{STM}.

If the value of one of the components in the bridge changes slightly, the bridge ratio changes $\alpha = \alpha_0 + \delta\alpha$ and a non-zero V_{out} is generated. For $\delta\alpha \ll \alpha_0$ linear response can be invoked so that $V_{out} = \lambda\delta\alpha$. The constant λ is determined by using the ratio transformer to move off-balance with several known values of $\delta\alpha$ and measuring the response V_{out}. Fig. C.3 shows one set of V_{out}, $\delta\alpha$ and the straight line fit used to determine λ.

During coarse approach, the capacitance C^0_{STM} will change by δC_{STM}. Differentiating Eq. C.3 gives

$$\delta C_{STM} = -\frac{C_{ref}}{\alpha_0^2}\delta\alpha \tag{C.4}$$

Using Eqs. C.1, C.2, C.3, and C.4 gives

$$V_{out} = -\lambda\alpha_0^2 \left(\frac{C^0_{STM}}{C_{ref}}\right)\left(\frac{\delta L}{L}\right) = \left\{-\lambda\frac{(1-\alpha_0)\,\alpha_0}{L}\right\}\delta L$$

The quantity in braces is the calibration constant that converts between displacements δL and the measured voltage V_{out} on the lock-in.

The data in Fig. C.3 can be used as a specific example of position sensor calibration. This was a calibration performed on Davis Group STM2 November 23, 2005 after building a new scanner with a larger capacitor plate than previously. The linear fit in Fig. C.3 to $\delta V_{out} = \lambda \delta\alpha + b$ coughs up $\lambda = -139.772$mV, $b = -0.00086$mV. The balance point was $\alpha_0 = 0.40268$, and the length of the capacitor cylinder is $L = 0.450'$. Plugging in,

$$-\lambda \frac{(1-\alpha_0)\,\alpha_0}{L} = 3.0\mu\text{V}/^{-}\text{m}$$

or $0.34\mu\text{m}/\mu\text{V}$. The amplitude of the lock-in reference sine wave applied to V_{in} was 5V.

BIBLIOGRAPHY

[1] Steven Weinberg, To the postdocs, *Physics Today* March 2007, 58

[2] Ivar Giaever, Energy Gap in Superconductors Measured by Electron Tunneling, *Phys. Rev. Lett.* **5**, 147 (1960)

[3] Ivar Giaever, Electron Tunneling Between Two Superconductors, *Phys. Rev. Lett.* **5**, 464 (1960)

[4] Ivar Giaever and Karl Megerle, Study of Superconductors by Electron Tunneling, *Phys. Rev.* **122**, 1101 (1961)

[5] J. Bardeen, L.N. Cooper, and J.R. Schrieffer, Theory of Superconductivity, *Phys. Rev.* **108**, 1175 (1957)

[6] W. L. McMillan and J. M. Rowell, Lead Phonon Spectrum Calculated from Superconducting Density of States, *Phys. Rev. Lett.* **14**, 108 (1965)

[7] G.M. Eliashberg, *Soviet Phys. -JETP* **11**, 696 (1960)

[8] J. M. Rowell, W. L. McMillan, and W. L. Feldmann, Phonon Spectra in Pb and Pb40Tl60 Determined by Tunneling and Neutron Scattering, *Phys. Rev.* **178**, 897 (1969)

[9] J. M. Rowell, W. L. McMillan, and W. L. Feldmann, Phonon Emission and Self-Energy Effects in Normal-Metal Tunneling, *Phys. Rev.* **180**, 658 (1969)

[10] David J. Griffiths, *Introduction to Quantum Mechanics*, Prentice Hall - New Jersey (1995)

[11] Kurt Gottfried and Tung-Mow Yan, *Quantum Mechanics: Fundamentals, 2nd Ed.*, Springer - New York (2003)

[12] J. Bardeen, Tunneling from a many-particle point of view, *Phy. Rev. Lett.* **6**, 57 (1961)

[13] Henrik Bruus and Karsten Flensberg, *Many-Body Theory in Condensed Matter Physics*, Oxford University Press - New York (2004)

[14] Philip Phillips, *Advanced Solid State Physics*, Westview Press - Boulder, CO (2003)

[15] Charles T. Black and Jeffrey J. Welser, Electric-Field Penetration Into Metals: Consequences for High-Dielectric-Constant Capacitors, *IEEE T. Electron Dev.* **46**, 776 (1999)

[16] N.D. Lang and W. Kohn, Theory of Metal Surfaces: Induced Surface Charge and Image Potentials, *Phy. Rev. B.* **7**, 3541 (1973)

[17] R.M. Feenstra and Joseph Stroscio, Tunneling spectroscopy of the GaAs(110) surface, *J. Vac. Sci. Technol. B* **5**, 923 (1987)

[18] M. Chiao, Low-energy quasiparticles in cuprate superconductors: A quantitative analysis, *Phys. Rev. B.* **62**, 3554 (2000)

[19] Walter A. Harrison, Tunneling from an Independent-Particle Point of View, *Phys. Rev.* **123**, 85 (1961)

[20] John G. Simmons, Electric Tunnel Effect between Dissimilar Electrodes Separated by a Thin Insulating Film, *J. Appl. Phys.* **34**, 2581 (1963)

[21] J. Tersoff and D. R. Hamann, Theory and Application for the Scanning Tunneling Microscope, *Phys. Rev. Lett.* **50**, 1998 (1983)

[22] J. Tersoff and D. R. Hamann, Theory of the scanning tunneling microscope, *Phys. Rev. B* **31**, 805 (1985)

[23] S. H. Pan, J. P. O'Neal, R. L. Badzey, C. Chamon, H. Ding, J. R. Engelbrecht, Z. Wang, H. Eisaki, S. Uchida, A. K. Guptak, K.-W. Ngk, E. W. Hudson, K. M. Lang and J. C. Davis, Microscopic electronic inhomogeneity in the high-T_C superconductor $Bi_2Sr_2CaCu_2O_{8+x}$, *Nature* **413**, 282 (2001)

[24] K. M. Lang, V. Madhavan, J. E. Hoffman, E. W. Hudson, H. Eisaki, S. Uchida and J. C. Davis, Imaging the granular structure of high-Tc superconductivity in underdoped $Bi_2Sr_2CaCu_2O_{8+x}$, *Nature* **415**, 412 (2002)

[25] Roland Wiesendanger, *Scanning Probe Microscopy and Spectroscopy*, Cambridge University Press - New York (1994)

[26] Eric W. Hudson, Ph.D. dissertation, University of California, Berkeley (1999)

[27] Jennifer E. Hofmann, Ph.D. dissertation, University of California, Berkeley (2003)

[28] Curry B. Taylor, Ph.D. dissertation, Cornell University (2008)

[29] G. Binning, H. Rohrer, Ch. Gerber, and E. Weibel, Tunneling through a controllable vacuum gap, *Appl. Phys. Lett.* **40**, 178 (1982)

[30] J. Friedel, Metallic Alloys, *Nuovo Cimento Suppl.* **7**, 287 (1958)

[31] M. F. Crommie, C. P. Lutz, and D. M. Eigler, Imaging standing waves in a two-dimensional electron gas, *Nature* **363**, 524 (1993)

[32] Y. Hasegawa and Ph. Avouris, Direct Observation of Standing Wave Formation at Surface Steps Using Scanning Tunneling Spectroscopy, *Phys. Rev. Lett.* **71**, 1071 (1993)

[33] L. Petersen, Ph. Hofmann, E. W. Plummer, F. Besenbacher, Fourier Transform-STM: determining the surface Fermi contour, *J. Electron Spectrosc. Relat. Phenom.* **109**, 97 (2000)

[34] Andrew P. Mackenzie, Professor of Physics, St. Andrews University, private communication

[35] Milan Allan *et. al.*, in preparation

[36] R. A. Borzi, S. A. Grigera, J. Farrell, R. S. Perry, S. J. S. Lister, S. L. Lee, D. A. Tennant, Y. Maeno, and A. P. Mackenzie, Formation of a Nematic Fluid at High Fields in $Sr_3Ru_2O_7$, *Science* **315**, 214 (2007)

[37] D. J. Van Harlingen, Phase-sensitive tests of the symmetry of the pairing state in the high-temperature superconductors—Evidence for $d_{x^2-y^2}$ symmetry, *Rev. Mod. Phys.* **67**, 515 (1995)

[38] C. C. Tsuei and J. R. Kirtley, Pairing symmetry in cuprate superconductors, *Rev. Mod. Phys.* **72**, 969 (2000)

[39] Andrea Damascelli, Zahid Hussain, and Zhi-Xun Shen, Angle-resolved photoemission studies of the cuprate superconductors, *Rev. Mod. Phys.* **75**, 473 (2003)

[40] J. C. Campuzano, M. R. Norman, and M. Randeria, Photoemission in the High Tc Superconductors, **The Physics of Superconductors, Vol. II**, p167-273 ed. K. H Bennemann and J. B. Ketterson, Springer - New York (2004)

[41] Qiang-Hua Wang and Dung-Hai Lee, Quasiparticle scattering interference in high-temperature superconductors, *Phys. Rev. B.* **67**, 20511 (2003)

[42] Kyle P. McElroy, Ph.D. dissertation, University of California, Berkeley (2005)

[43] J. E. Hoffman, K. McElroy, D.-H. Lee, K. M Lang, H. Eisaki, S. Uchida, and J. C. Davis, Imaging Quasiparticle Interference in $Bi_2Sr_2CaCu_2O_{8+\delta}$, *Science* **297**, 1148 (2002)

[44] K. McElroy, R. W. Simmonds, J. E. Hoffman, D.-H. Lee, J. Orenstein, H. Eisaki, S. Uchida and J. C. Davis, Relating atomic-scale electronic phenomena to wave-like quasiparticle states in superconducting $Bi_2Sr_2CaCu_2O_{8+\delta}$, *Nature* **422**, 592 (2003)

[45] T. Pereg-Barnea and M. Franz, Magnetic-field dependence of quasiparticle interference peaks in a d-wave superconductor with weak disorder, *Phys. Rev. B.* **78**, 020509 (2008)

[46] T. Hanaguri, Y. Kohsaka, J. C. Davis, C. Lupien, I. Yamada, M. Azuma, M. Takano, K. Ohishi, M. Ono, and H. Takagi, Quasiparticle interference and superconducting gap in $Ca_{2-x}Na_xCuO_2Cl_2$, *Nat. Phys.* **3**, 865 (2007)

[47] T. Hanaguri, Y. Kohsaka, M. Ono, M. Maltseva, P. Coleman, I. Yamada, M. Azuma, M. Takano, K. Ohishi and H. Takagi, Coherence Factors in a High-T_C Cuprate Probed by Quasi-Particle Scattering Off Vortices, *Science* **323**, 923 (2009)

[48] R. S. Markiewicz, Bridging k and q space in the cuprates: Comparing angle-resolved photoemission and STM results, *Phys. Rev. B.* **69**, 214517 (2004)

[49] K. McElroy, G.-H. Gweon, S. Y. Zhou, J. Graf, S. Uchida, H. Eisaki, H. Takagi, T. Sasagawa, D.-H. Lee, and A. Lanzara, Elastic Scattering Susceptibility of the High Temperature Superconductor $Bi_2Sr_2CaCu_2O_{8+\delta}$: A Comparison between Real and Momentum Space Photoemission Spectroscopies, *Phys. Rev. Lett.* **96**, 067005 (2006)

[50] U. Chatterjee, M. Shi, A. Kaminski, A. Kanigel, H. M. Fretwell, K. Terashima, T. Takahashi, S. Rosenkranz, Z. Z. Li, H. Raffy, A. Santander-Syro, K. Kadowaki, M. R. Norman, M. Randeria, and J. C. Campuzano, Nondispersive Fermi Arcs and the Absence of Charge Ordering in the Pseudogap Phase of $Bi_2Sr_2CaCu_2O_{8+\delta}$, *Phys. Rev. Lett.* **96**, 107006 (2006)

[51] U. Chatterjee, M. Shi, A. Kaminski, A. Kanigel, H. M. Fretwell, K. Terashima, T. Takahashi, S. Rosenkranz, Z. Z. Li, H. Raffy, A. Santander-Syro, K. Kadowaki, M. Randeria, M. R. Norman, and J. C. Campuzano, Anomalous dispersion in the autocorrelation of angle-resolved photoemission spectra of high-temperature $Bi_2Sr_2CaCu_2O_{8+\delta}$ superconductors, *Phys. Rev. B.* **76**, 012504 (2007)

[52] I. Martin, A. V. Balatsky, and J. Zaanen, Impurity States and Interlayer Tunneling in High Temperature Superconductors, *Phys. Rev. Lett.* **88**, 097003 (2002)

[53] Congjun Wu, Tao Xiang, and Zhao-Bin Su, Absence of the zero bias peak in vortex tunneling spectra of high-temperature superconductors, *Phys. Rev. B.* **62**, 14427 (2000)

[54] K. McElroy, Jinho Lee, J. A. Slezak, D.-H. Lee, H. Eisaki, S. Uchida, and J. C. Davis, Atomic-Scale Sources and Mechanism of Nanoscale Electronic Disorder in $Bi_2Sr_2CaCu_2O_{8+\delta}$, *Science* **309**, 1048 (2005)

[55] Y. Kohsaka, C. Taylor, K. Fujita, A. Schmidt, C. Lupien, T. Hanaguri, M. Azuma, M. Takano, H. Eisaki, H. Takagi, S. Uchida, J. C. Davis, An Intrinsic Bond-Centered Electronic Glass with Unidirectional Domains in Underdoped Cuprates, *Science* **315**, 1380 (2007)

[56] T. Hanaguri, C. Lupien, Y. Kohsaka, D.-H. Lee, M. Azuma, M. Takano, H. Takagi, and J. C. Davis, A 'checkerboard' electronic crystal state in lightly hole-doped $Ca_{2-x}Na_xCuO_2Cl_2$, *Nature* **430**, 1001 (2004)

[57] K. Fujita, Ilya Grigorenko, J. Lee, M. Wang, JianXinZhu, J.C. Davis, H. Eisaki, S. Uchida, and Alexander V. Balatsky, Bogoliubov angle and visualization of particle-hole mixture in superconductors, *Phys. Rev. B.* **78**, 054510 (2008)

[58] Tom Timusk and Bryan Statt, The pseudogap in high-temperature superconductors: an experimental survey, *Rep. Prog. Phys.* **62**, 61 (1998)

[59] M. R. Norman, H. Ding, M. Randeria, J. C. Campuzano, T. Yokoya, T. Takeuchik, T. Takahashi, T. Mochiku, K. Kadowaki, P. Guptasarma and D. G. Hinks, Destruction of the Fermi surface in underdoped high-T_C superconductors, *Nature* **392**, 157 (1998)

[60] Ch. Renner, B. Revaz, J.-Y. Genoud,1 K. Kadowaki, and Ø. Fischer, Pseu-

dogap Precursor of the Superconducting Gap in Under- and Overdoped $Bi_2Sr_2CaCu_2O_{8+\delta}$, *Phys. Rev. Lett.* **80**, 149 (1998)

[61] Ben Stein, "The Smoot-Hawley Act Is More Than a Laugh Line", *The New York Times* May 9, 2009

[62] S. H. Pan, E. W. Hudson, and J. C. Davis, ^{3}He refrigerator based very low temperature scanning tunneling microscope. *Rev. Sci. Instrum.* **70**, 1459 (1998)

[63] William H. Press, Saul A. Teukolosky, William T. Vetterling, and Brian P. Flannery, *Numerical Recipes in C*, Second Edition, Cambridge University Press - New York (1992)

[64] L. Capriotti, D. J. Scalapino, and R. D. Sedgewick, Wave-vector power spectrum of the local tunneling density of states: Ripples in a *d*-wave sea, *Phys. Rev. B* **68**, 014508 (2003)

[65] Alan V. Oppenheim and Ronald W. Schafer, *Discrete-Time Signal Processing*, Prentice Hall - New Jersey (1989)

[66] T. Pereg-Barnea and M. Franz, Theory of quasiparticle interference patterns in the pseudogap phase of the cuprate superconductors, *Phys. Rev. B* **68**, 180506 (2003)

[67] J. D. Scargle, Studies in Astronomical Time Series Analysis II. Statistical Aspects of Spectral Analysis of Unevenly Sampled Data, *Astrophysical Journal* **263**, 835 (1982)

[68] D. V. Hinkley, On the ratio of two correlated normal random variables, *Biometrika* **56**, 635 (1969)

[69] Lingyin Zhu, W. A. Atkinson, and P. J. Hirschfeld, Power spectrum of many impurities in a *d*-wave superconductor, *Phys. Rev. B* **69**, 060503 (2004)

[70] L. Dell'Anna, J. Lorenzana, M. Capone, C. Castellani, and M. Grilli, Effect of mesoscopic inhomogeneities on local tunneling density of states in cuprates, *Phys. Rev. B* **71**, 064518 (2005)

[71] O. Kodra and W. A. Atkinson, Many-impurity effects in Fourier transform scanning tunneling spectroscopy, *Phys. Rev. B* **73**, 045404 (2006)

[72] Tamara S. Nunner, Wei Chen, Brian M. Andersen, Ashot Melikyan, and P. J. Hirschfeld, Fourier transform spectroscopy of *d*-wave quasiparticles in the presence of atomic scale pairing disorder, *Phys. Rev. B* **73**, 104511 (2006)

[73] N. David Mermin, What's bad about this habit, *Physics Today* May 2009, 8

[74] J. Mesot, M. R. Norman, H. Ding, M. Randeria, J. C. Campuzano, A. Paramekanti, H. M. Fretwell, A. Kaminski, T. Takeuchi, T. Yokoya, T. Sato, T. Takahashi, T. Mochiku, and K. Kadowaki, Superconducting Gap Anisotropy and Quasiparticle Interactions: A Doping Dependent Photoemission Study, *Phys. Rev. Lett.* **83**, 840 (1999)

[75] M. Le Tacon, A. Sacuto, A. Georges, G. Kotliar, Y. Gallais, D. Colson and A. Forget, Two energy scales and two distinct quasiparticle dynamics in the superconducting state of underdoped cuprates, *Nat. Phys.* **2**, 537 (2006)

[76] J. M. Luttinger, Fermi Surface and Some Simple Equilibrium Properties of a System of Interacting Fermions, *Phys. Rev.* **119**, 1153 (1960)

[77] I. Dzyaloshinskii, Some consequences of the Luttinger theorem: The Luttinger surfaces in non-Fermi liquids and Mott insulators. *Phys. Rev.* **B** 68, 085113 (2003)

[78] W. J. Padilla, Y. S. Lee, M. Dumm, G. Blumberg, S. Ono, Kouji Segawa, Seiki Komiya, Yoichi Ando, and D. N. Basov, Constant effective mass across the phase diagram of high-T_C cuprates, *Phys. Rev. B* **72**, 060511 (2005)

[79] D. N. Basov and T. Timusk, Electrodynamics of high-T_C superconductors, *Rev. Mod. Phys.* **77**, 721 (2005)

[80] K. -Y. Yang, T. M. Rice, and F. -C. Zhang, Phenomenological theory of the pseudogap state. *Phys. Rev. B* **73**, 174501 (2006).

[81] Neil W. Ashcroft and N. David Mermin, **Solid State Physics**, Brooks Cole - New York (1976)

[82] Kiyohisa Tanaka, W. S. Lee, D. H. Lu, A. Fujimori, T. Fujii, Risdiana, I. Terasaki, D. J. Scalapino, T. P. Devereaux, Z. Hussain, and Z.-X. Shen, Distinct Fermi-Momentum-Dependent Energy Gaps in Deeply Underdoped Bi2212, *Science* **314**, 1910 (2006)

[83] W. S. Lee, I. M. Vishik, K. Tanaka, D. H. Lu, T. Sasagawa, N. Nagaosa, T. P. Devereaux, Z. Hussain and Z.-X. Shen, Abrupt onset of a second energy gap at the superconducting transition of underdoped Bi2212, *Nature* **450**, 81 (2007)

[84] K. McElroy, D.-H. Lee, J. E. Homan, K. M Lang, E. W. Hudson, S. Uchida, J. Lee and J.C. Davis, Homogeneous nodal superconductivity coexisting with inhomogeneous charge order in strongly underdoped $Bi_2Sr_2CaCu_2O_{8+\delta}$, arXiv:cond-mat/0404005 (unpublished)

[85] K. McElroy, D.-H. Lee, J. E. Hoffman, K. M. Lang, J. Lee, E.W. Hudson, H. Eisaki, S. Uchida, and J. C. Davis, Coincidence of Checkerboard Charge Order and Antinodal State Decoherence in Strongly Underdoped Superconducting $Bi_2Sr_2CaCu_2O_{8+\delta}$, *Phys. Rev. Lett.* **94**, 197005 (2005)

[86] J. W. Alldredge, Jinho Lee, K. McElroy, M. Wang, K. Fujita, Y. Kohsaka, C. Taylor, H. Eisaki, S. Uchida, P. J. Hirschfeld, and J. C. Davis, Evolution of the electronic excitation spectrum with strongly diminishing hole density in superconducting $Bi_2Sr_2CaCu_2O_{8+\delta}$, *Nature Physics* **4**, 319 (2008)

[87] Y. Kohsaka, C. Taylor, P. Wahl, A. Schmidt, Jhinhwan Lee, K. Fujita, J. W. Alldredge, K. McElroy, Jinho Lee1, H. Eisaki, S. Uchida, D.-H. Lee and J. C. Davis, How Cooper pairs vanish approaching the Mott insulator in $Bi_2Sr_2CaCu_2O_{8+\delta}$, *Nature* **454**, 1072 (2008)

[88] C. Howald, P. Fournier, and A. Kapitulnik, Inherent inhomogeneities in tunneling spectra of $Bi_2Sr_2CaCu_2O_{8-x}$ crystals in the superconducting state, *Phys Rev B* **64**, 100504 (2001)

[89] Kenjiro K. Gomes, Abhay N. Pasupathy, Aakash Pushp, Shimpei Ono, Yoichi Ando & Ali Yazdani, Visualizing pair formation on the atomic scale in the high-T_c superconductor $Bi_2Sr_2CaCu_2O_{8+\delta}$, *Nature* **447**, 569 (2007)

[90] W. D. Wise, M. C. Boyer, Kamalesh Chatterjee, Takeshi Kondo, T. Takeuchi, H. Ikuta, Yayu Wang, and E. W. Hudson, Charge-density-wave origin of cuprate checkerboard visualized by scanning tunnelling microscopy, *Nature Physics* **4**, 696 (2008)

[91] A. Kanigel, U. Chatterjee, M. Randeria, M. R. Norman, S. Souma, M. Shi, Z. Z. Li, H. Raffy, and J. C. Campuzano, Protected Nodes and the Collapse of Fermi Arcs in High-T_C Cuprate Superconductors, *Phys. Rev. Lett.* **99**, 157001 (2007)

[92] R. P. Feynman, Superfluidity and Superconductivity, *Rev. Mod. Phys.* **29**, 205 (1957)

[93] Y. J. Uemura, G. M. Luke, B. J. Sternlieb, J. H. Brewer, J. F. Carolan, W. N. Hardy, R. Kadono, J. R. Kempton, R. F. Kiefl, S. R. Kreitzman, P. Mulhern, T. M. Riseman, D. Ll. Williams, B. X. Yang, S. Uchida, H. Takagi, J. Gopalakrishnan, A. W. Sleight, M. A. Subramanian, C. L. Chien, M. Z. Cieplak, Gang Xiao, V. Y. Lee, B. W. Statt, C. E. Stronach, W. J. Kossler, and X. H. Yu, Universal Correlations between T_c and $n_s/m*$ in High-T_c Cuprate Superconductors, *Phys. Rev. Lett.* **62**, 2317 (1989)

[94] V. J. Emery and S. A. Kivelson, Importance of phase fluctuations in superconductors with small superfluid density, *Nature* **374**, 434 (1995)

[95] V. J. Emery and S. A. Kivelson, Superconductivity in Bad Metals, *Phys. Rev. Lett.* **74**, 3253 (1995)

[96] J. Corson, R. Mallozzi, J. Orenstein, J. N. Eckstein, and I. Bozovic, Vanishing of phase coherence in underdoped $Bi_2Sr_2CaCu_2O_{8+\delta}$, *Nature* **398**, 221 (1999)

[97] Z. A. Xu, Y. Wang, T. Kakeshita, S. Uchida, and N. P. Ong, Vortex-like excitations and the onset of superconducting phase fluctuations underdoped $La_{2-x}Sr_xCuO_4$, *Nature* **406**, 486 (2000)

[98] Yayu Wang, Lu Li, M. J. Naughton, G. D. Gu, S. Uchida, and N. P. Ong, Field-Enhanced Diamagnetism in the Pseudogap State of the Cuprate Superconductor $Bi_2Sr_2CaCu_2O_{8+\delta}$ in an Intense Magnetic Field, *Phys. Rev. Lett.* **95**, 247002 (2005)

[99] Michael Tinkham, *Introduction to Superconductivity Second Edition*, Dover Publications Inc., Mineola, New York (1996)

[100] N. Bergeal, J. Lesueur, M. Aprili, G. Faini, J. P. Contour and B. Leridon, Pairing fluctuations in the pseudogap state of copper-oxide superconductors probed by the Josephson effect, *Nature Physics* **4**, 608 (2008)

[101] S. Kamal, D. A. Bonn, Nigel Goldenfeld, P. J. Hirschfeld, Ruixing Liang, and W. N. Hardy, Penetration Depth Measurements of 3D XY Critical Behavior in $YBa_2Cu_3O_{6.95}$ Crystals, *Phys. Rev. Lett.* **73**, 1845 (1994)

[102] Sudip Chakravarty, R. B. Laughlin, Dirk K. Morr, and Chetan Nayak, Hidden order in the cuprates, *Phys. Rev. B.* **63**, 094503 (2001)

[103] Cristina Bena, Sudip Chakravarty, Jiangping Hu, and Chetan Nayak, Quasiparticle scattering and local density of states in the *d*-density-wave phase, *Phys. Rev. B* **69**, 134517 (2004)

[104] Erez Berg and Ehud Altman, Evolution of the Fermi Surface of *d*-Wave Superconductors in the Presence of Thermal Phase Fluctuations, *Phys. Rev. Lett.* **99**, 247001 (2007)

[105] Philip A. Casey, J. D. Koralek, N. C. Plumb, D. S. Dessau, and Philip W. Anderson, Accurate theoretical fits to laser-excited photoemission spectra in the normal phase of high-temperature superconductors, *Nature Physics* **4**, 210 (2008).

[106] Michael Vershinin, Shashank Misra, S. Ono, Y. Abe, Yoichi Ando, Ali Yazdani, Local Ordering in the Pseudogap State of the High-Tc Superconductor $Bi_2Sr_2CaCu_2O_{8+\delta}$, *Science* **303**, 1995 (2004)

[107] S. H. Pan, E.W. Hudson, A. K. Gupta, K.-W. Ng, H. Eisaki, S. Uchida, and J. C. Davis, STM Studies of the Electronic Structure of Vortex Cores in $Bi_2Sr_2CaCu_2O_{8+\delta}$, *Phys. Rev. Lett.* **85**, 1536 (2000)

[108] J. E. Hoffman, E. W. Hudson, K. M. Lang, V. Madhavan, H. Eisaki, S. Uchida, and J. C. Davis, A Four Unit Cell Periodic Pattern of Quasi-Particle States Surrounding Vortex Cores in $Bi_2Sr_2CaCu_2O_{8+\delta}$, *Science* **295**, 466 (2002)

[109] Robert Laughlin, Nobel Lecture: Fractional quantization, *Rev. Mod. Phys* **71**, 863 (1999)

[110] L. P. Gor'kov and Gregory B. Teitel'baum, Interplay of Externally Doped and Thermally Activated Holes in $La_{2-x}Sr_xCuO_4$ and Their Impact on the Pseudogap Crossover, *Phys. Rev. Lett.* **97**, 247003 (2006)

[111] Y. S. Lee, Kouji Segawa, Z. Q. Li, W. J. Padilla, M. Dumm, S. V. Dordevic, C. C. Homes, Yoichi Ando, and D. N. Basov, Electrodynamics of the nodal metal state in weakly doped high-T_C cuprates, *Phys. Rev. B* **72**, 054529 (2005)

[112] J.W. Loram, J. Luo, J.R. Cooper, W.Y. Liang, J.L. Tallon, Evidence on the

pseudogap and condensate from the electronic specific heat, *Journal of Physics and Chemistry of Solids* **62**, 59 (2001)

[113] Abhay N. Pasupathy, Aakash Pushp, Kenjiro K. Gomes, Colin V. Parker, Jinsheng Wen, Zhijun Xu, Genda Gu, Shimpei Ono, Yoichi Ando, and Ali Yazdani, Electronic Origin of the Inhomogeneous Pairing Interaction in the High-T_C Superconductor $Bi_2Sr_2CaCu_2O_{8+\delta}$, *Science* **320**, 196 (2008)

[114] Aakash Pushp, Colin V. Parker, Abhay N. Pasupathy, Kenjiro K. Gomes, Shimpei Ono, Jinsheng Wen, Zhijun Xu, Genda Gu, and Ali Yazdani, Extending Universal Nodal Excitations Optimizes Superconductivity in $Bi_2Sr_2CaCu_2O_{8+\delta}$, *Science* **326**, 1689 (2009)

[115] Kyle M. Shen, F. Ronning, D. H. Lu, F. Baumberger, N. J. C. Ingle, W. S. Lee, W. Meevasana, Y. Kohsaka, M. Azuma, M. Takano, H. Takagi, and Z.-X. Shen, Nodal Quasiparticles and Antinodal Charge Ordering in $Ca_{2-x}Na_xCuO_2Cl_2$, *Science* **307**, 901 (2005)

[116] A. Kanigel, M. R. Norman, M. Randeria, U. Chatterjee, S. Souma, A. Kaminski, H. M. Fretwell, S. Rosenkranz, M. Shi, T. Sato, T. Takahashi, Z. Z. Li, H. Raffy, K. Kadowaki, D. Hinks, L. Ozyuzer and J. C. Campuzano, Evolution of the pseudogap from Fermi arcs to the nodal liquid, *Nature Physics* **2**, 447 (2006)

[117] Cyril Proust, Etienne Boaknin, R.W. Hill, Louis Taillefer, and A. P. Mackenzie, Heat Transport in a Strongly Overdoped Cuprate: Fermi Liquid and a Pure *d*-Wave BCS Superconductor, *Phys. Rev. Lett.* **89**, 147003 (2002)

[118] N. E. Hussey, M. Abdel-Jawad, A. Carrington, A. P. Mackenzie and L. Balicas, A coherent three-dimensional Fermi surface in a high-transition temperature superconductor, *Nature* **425**, 814 (2003)

[119] B. Vignolle, A. Carrington, R. A. Cooper, M. M. J. French, A. P. Mackenzie, C. Jaudet, D. Vignolles, Cyril Proust and N. E. Hussey, Quantum oscillations in an overdoped high-T_C superconductor, *Nature* **455**, 952 (2008)

[120] A. Kaminski, S. Rosenkranz, H. M. Fretwell, M. R. Norman, M. Randeria, J. C. Campuzano, J-M. Park, Z. Z. Li, and H. Raffy, Change of Fermi-surface topology in $Bi_2Sr_2CaCu_2O_{8+\delta}$ with doping, *Phys. Rev. B* **73**, 174511 (2006)

[121] Takeshi Kondo, Rustem Khasanov, Tsunehiro Takeuchi, Jorg Schmalian and Adam Kaminski, Competition between the pseudogap and superconductivity in the high-T_C copper oxides, *Nature* **457**, 296 (2009)

[122] H.-B. Yang, J. D. Rameau, P. D. Johnson, T. Valla, A. Tsvelik and G. D. Gu, Emergence of preformed Cooper pairs from the doped Mott insulating state in $Bi_2Sr_2CaCu_2O_{8+\delta}$, *Nature* **456**, 77 (2008)

[123] A. Kanigel, U. Chatterjee, M. Randeria, M. R. Norman, G. Koren, K. Kadowaki, and J. C. Campuzano, Evidence for Pairing above the Transition Temperature of Cuprate Superconductors from the Electronic Dispersion in the Pseudogap Phase, *Phys. Rev. Lett.* **101**, 137002 (2008)

[124] P. W. Anderson, The Resonating Valence Bond State in La_2CuO_4 and Superconductivity, *Science* **235**, 1196 (1987)

[125] Gabriel Kotliar and Jianlin Liu, Superexchange mechanism and *d*-wave superconductivity, *Phys. Rev. B* **38**, 5142 (1988)

[126] Patrick A. Lee, Naoto Nagaosa, and Xiao-Gang Wen, Doping a Mott insulator: Physics of high-temperature superconductivity, *Rev. Mod. Phys.* **78**, 17 (2006)

[127] Arun Paramekanti, Mohit Randeria, and Nandini Trivedi, Projected Wave Functions and High Temperature Superconductivity, *Phys. Rev. Lett.* **87**, 217002 (2001)

[128] Arun Paramekanti, Mohit Randeria, and Nandini Trivedi, High- T_C superconductors: A variational theory of the superconducting state, *Phys. Rev. B* **70**, 054504 (2004)

[129] Tudor D. Stanescu and Gabriel Kotliar, Fermi arcs and hidden zeroes of the Green function in the pseudogap state, *Phys. Rev. B* **74**, 125110 (2006)

[130] Kristjan Haule and Gabriel Kotliar, Strongly correlated superconductivity: A plaquette dynamical mean-field theory study, *Phys. Rev. B* **76**, 104509 (2007)

[131] J. M. Tranquada, S. M. Heald, and A. R. Moodenbaugh, X-ray-absorption near-edge-structure study of $La_{2-x}(Ba,Sr)_xCuO_{4-y}$ superconductors, *Phys. Rev. B* **36**, 5263 (1987)

[132] C. T. Chen, F. Sette, Y. Ma, M. S. Hybertsen, E. B. Stechel, W. M. C. Foulkes, M. Schulter, S-W. Cheong, A. S. Cooper, L. W. Rupp, Jr., B. Batlogg, Y. L. Soo, Z. H. Ming, A. Krol, and Y. H. Kao, Electronic states in $La_{2-x}Sr_xCuO_{4+\delta}$ probed by soft-x-ray absorption, *Phys. Rev. Lett.* **66**, 104 (1991)

[133] J. Zaanen, G. A. Sawatzky, and J. W. Allen, Band gaps and electronic structure of transition-metal compounds, *Phys. Rev. Lett.* **55**, 418 (1985)

[134] V. J. Emery, Theory of High-T_C Superconductivity in Oxides, *Phys. Rev. Lett.* **58**, 2794 (1987)

[135] S. A. Kivelson, E. Fradkin and V. J. Emery, Electronic liquid-crystal phases of a doped Mott insulator, *Nature* **393**, 550 (1998)

[136] Jan Zaneen and Olle Gunnarsson, Charged magnetic domain lines and the magnetism of high-T_C oxides, *Phys. Rev. B* **40**, 7391 (1989)

[137] J. M. Tranquada, H. Woo, T. G. Perring, H. Goka, G. D. Gu, G. Xu, M. Fujita and K. Yamada, Quantum magnetic excitations from stripes in copper oxide superconductors, *Nature* **429**, 534 (2004)

[138] N. Read and Subir Sachdev, Valence-Bond and Spin-Peierls Ground States of Low-Dimensional Quantum Antiferromagnets, *Phys. Rev. Lett.* **62**, 1694 (1989)

[139] Subir Sachdev, Quantum magnetism and criticality, *Nature Physics* **4**, 173 (2008)

[140] Nobuo Furukawa, T. M. Rice, and Manfred Salmhofer, Truncation of a Two-Dimensional Fermi Surface due to Quasiparticle Gap Formation at the Saddle Points, *Phys. Rev. Lett.* **81**, 3195 (1998)

[141] C. Honerkamp, M. Salmhofer, N. Furukawa, and T. M. Rice, Breakdown of the Landau-Fermi liquid in two dimensions due to Umklapp scattering. *Phys. Rev. B* **63**, 035109 (2001).

[142] M. Ossadnik, C. Honerkamp, T. M. Rice, and M. Sigrist, Breakdown of Landau Theory in Overdoped Cuprates near the Onset of Superconductivity, *Phys. Rev. Lett.* **101**, 256405 (2008)

[143] M. Abdel-Jawad, J. G. Analytis, L. Balicas, A. Carrington, J. P. H. Charmant, M. M. J. French, and N. E. Hussey, Correlation between the Superconducting Transition Temperature and Anisotropic Quasiparticle Scattering in $Tl_2Ba_2CuO_{6+\delta}$, *Phys. Rev. Lett.* **99**, 107002 (2007)

[144] Z. Schlesinger, R. T. Collins, F. Holtzberg, C. Feild, S. H. Blanton, U. Welp, G. W. Crabtree, Y. Fang, and J. Z. Liu, Superconducting Energy Gap and Normal-State Conductivity of a Single-Domain $YBa_2Cu_3O_7$ Crystal, *Phys. Rev. Lett*. **65**, 801 (1990)

[145] Kai-Yu Yang, H. -B. Yang, P. D. Johnson, T. M. Rice, and Fu-Chun Zhang, Quasiparticles in the pseudogap phase of underdoped cuprate, *Euro. Phys. Lett.* **86**, 37002 (2009)

[146] Raymond Wiley Simmonds, Ph.D. dissertation, University of California, Berkeley (2002)